COMPUTATIONAL STUDIES ON THE SELF-SENSING INVERSE PROBLEM ENHANCED WITH SENSOR DATA FUSION

by

Andrew Le Nguyen

A Thesis

Submitted to the Faculty of Purdue University

In Partial Fulfillment of the Requirements for the degree of

Master of Science in Aeronautics and Astronautics

School of Aeronautics and Astronautics

West Lafayette, Indiana

August 2025

THE PURDUE UNIVERSITY GRADUATE SCHOOL
STATEMENT OF COMMITTEE APPROVAL

Dr. Tyler N. Tallman, Chair

School of Aeronautics and Astronautics

Dr. Vikas Tomar

School of Aeronautics and Astronautics

Dr. Luz D. Sotelo

School of Mechanical Engineering

Approved by:

Dr. Dengfeng Sun

To my family and friends

ACKNOWLEDGMENTS

To say the journey was difficult is an understatement. My decision to pursue a master's degree was driven by the desire to further grow the knowledge I gained during my undergrad years and to hone my skills in order to become a more confident engineer. At the end of this journey, however, I realized I have accomplished more than anticipated.

I first would like to thank my advisor Dr. Tallman. I am truly grateful for the opportunity to work in his lab and for his strong mentorship and guidance in my research, as well as in academics and grad school survival skills. Through Dr. Tallman, I have become a better student, researcher, and thinker.

I next want to thank my parents. Their lifelong love and support and has shaped me into the person I am today. Their support and encouragement throughout these few years has helped achieve all that I have set out to do in grad school.

I also want to thank my fellow lab mates for always being around to share experiences, ideas, and advice. We make a great team, and I am happy to have become great friends with you all.

Finally, I would like to thank my best friends from undergrad for also being there for me. I am thankful for all the fun memories from the times I was able to take a break from the cornfields of Indiana to come visit.

TABLE OF CONTENTS

LIST OF TABLES

LIST OF FIGURES

ABBREVIATIONS

BVID	barely visible impact damage
CFRP	carbon fiber reinforced polymer
CNF	carbon nanofiber
DIC	digital image correlation
DS	displacement sensors
EIT	electrical impedance tomography
FFF	fused filament fabrication
iFEM	inverse finite element method
LEC	linear equality constraint
MSA	material state awareness
MWCNT	multi-walled carbon nanotubes
NDE	non-destructive evaluation
PC	polycarbonate
SDF	sensor data fusion
SNR	signal-to-noise ratio
SS	strain sensors
SSIP	self-sensing inverse problem
TPU	thermoplastic polyurethane

ABSTRACT

Many equipment operators and inspectors today make use of time-based maintenance strategies to ensure proper working order of engineering systems and structures. This approach can be costly and inefficient because inspections and maintenance are not targeted, and equipment downtime can be lengthy during this process. Condition-based maintenance, on the other hand, involves monitoring the condition of critical components or structures so that targeted maintenance is performed only when the parts being monitored exhibit signs indicating the end of its operational life. Shifting toward more efficient condition-based maintenance strategies for mechanical systems requires material state awareness (MSA) of the critical components and structures the system is comprised of. MSA of a structure involves attaining a thorough understanding of the structure's material properties, current mechanical state, and damage modes in order to estimate its remaining lifetime. Currently, many non-destructive evaluation (NDE) sensors and techniques are currently being developed and fielded for embedded sensing and condition monitoring applications, including in civil and aerospace structures. Among them, the self-sensing inverse problem (SSIP) is an emerging method that possesses great potential for providing MSA for piezoresistive materials.

Piezoresistive materials exhibit a change in electrical conductivity when subject to strain, making them a prime candidate for manufacturing structures that have the innate ability to transduce its mechanical state. The SSIP is a mathematical method that recovers the continuous displacement and strain field of the deformed piezoresistive material from measured resistivity (or conductivity) changes. Being able to obtain the full-field displacements and strains of a component or structure is a key insight into its mechanical state, enabling accurate stress and failure analyses that can prove invaluable for condition-based maintenance. Computational and experimental demonstrations of the SSIP to date have yielded good results on simple shapes and experimental test specimen. However, the accuracy of the SSIP recovered displacement field is not guaranteed because the SSIP is an ill-posed and undetermined inverse problem. Furthermore, present work on the SSIP has focused on simple shapes and loads, and the applicability of the SSIP on more complex geometries has not yet been explored.

In this work, sensor data fusion (SDF) of the electrical data the SSIP utilizes for displacement field recovery with discrete displacement and strain data is explored as a way to increase the accuracy of the reconstructed displacement field and to improve the reliability of the SSIP when the resistivity data contains noise and outliers. Through a series of computational experiments, it was found that by supplementing resistivity data with sensors providing displacement data, the SSIP was able to recover the displacement field of a complex shape resembling real world structural components with good accuracy. Recovery of the displacement field was not possible without the use of additional sensor data. Furthermore, the displacement sensors made the SSIP more robust to increases in resistivity data noise. When resistivity data were supplemented with sensors providing strain data, while not as accurate as reconstructions enhanced with displacement data, there was still a significant improvement in the displacement reconstruction accuracy, even with a moderate increase in resistivity data noise.

1. INTRODUCTION

All mechanical components, mechanisms, and structures possess a finite service life, and it is the duty of engineers to design and maintain those mechanical systems to ensure their safety and functionality throughout operation. To this end, engineers work to identify key failure modes and estimate operational lifetime during a system's design and analysis phase. However, once the system is deployed, the multitude of stresses induced by human and environmental factors, some of which unforeseen, makes it challenging to precisely predict the remaining useful life of its components. Therefore, routine inspections are necessary to certify the system for continued use or to perform maintenance. This time-based maintenance strategy can be costly and inefficient, often requiring a system's removal from service, meticulous comprehensive inspection, and even total disassembly. With the rise of advanced composite materials, especially in the aerospace and automotive industries, the inspection process becomes even more complex as composite materials exhibit material anisotropy and damage mechanisms distinct from traditional metallic structures, including matrix cracking, fiber breakage, and delamination. As a result, a number of equipment operators are shifting towards condition-based maintenance strategies, where information gathered from monitoring a system provides accurate failure prognosis so that targeted, proactive maintenance can be performed, reducing maintenance costs and downtime [1–3].

Effective employment of condition-based maintenance strategies hinges on real-time material state awareness (MSA). MSA of a system, structure, or component involves understanding its material properties, damage processes, and operational environment while continuously monitoring its current state to predict its future state and remaining lifetime [4]. Continuous monitoring can be achieved through the use of embedded nondestructive evaluation (NDE) sensors relaying relevant information including, but not limited to, strain and vibrational response [5–9]. However, some of the challenges of implementing NDE sensor networks include the complexity of incorporating sensors into the component or structure, the number of sensors required to achieve desired fidelity, and sensor reliability. One solution to overcome these challenges is to use self-sensing materials to manufacture parts in need of monitoring [10]. Broadly speaking, self-sensing materials are able to transduce a quantity

of interest through a measurable signal such that the component or structure itself becomes the sensor enabling MSA.

1.1 Self-Sensing Applications of Piezoresistive Materials

A piezoresistive material is a type of self-sensing material that exhibits a change in its electrical conductivity when subject to mechanical strain. Piezoresistive materials are often manufactured by dispersing a small amount of conductive nanofillers into an insulating material. When the volume fraction of nanofillers exceeds the percolation threshold, the nanofillers form a conductive network, imparting the originally insulating material with deformation dependent electrical conductivity. The conductivity is deformation dependent because it relies on the proximity of the nanofillers and well-connectedness of the nanofiller network. Strain on the material impacting the connectivity of the network manifests as a conductivity change. For instance, tensile strains increasing the distance among nanofillers generally decreases the material conductivity, whereas compressive strains decrease the distance between nanofillers, increasing conductivity. More extreme mechanical perturbations can sever the connection between nanofillers, which can be indicative of a certain level of damage to the material. Thus, piezoresistive materials have garnered interest for a variety of applications [11–15].

To summarize a few representative examples of these applications, with the eventual goal of creating self-sensing pediatric scoliosis braces, Verma et al. [12] manufactured a piezoresistive thermoplastic consisting of polypropylene random copolymer (PPR) modified with multi-walled carbon nanotubes (MWCNT) which was used as 3D-printing stock. The PPR/MWCNT was printed into dog-bone specimens via fused filament fabrication (FFF) with filaments oriented along and perpendicular to the length of the dog-bone, and quasi-static tension and cyclic loading tests were performed to characterize its piezoresistive properties. From the tensile test, Verma et al. identified the material's gauge factor for different nanofiller concentrations and print orientations, and, from the cyclic loading tests, demonstrated the stability of its piezoresistive response, all shown in Figure 1.1. The adequate

sensitivity to strain and consistent piezoresistive response after repeated loading proved PPR/MWCNT as a viable material for self-sensing applications.

As another example, Hohimer et al. [13] fabricated pneumatic actuators using thermoplastic polyurethane modified with multi-walled carbon nanotubes (TPU/MWCNT). Four actuators were manufactured via FFF containing either 1, 2, 3, or 4 wt.% MWCNT, and each was inflated to three different pressure levels. Measuring the resistance change through cycles of pressurization and depressurization, the actuators with 1 and 2 wt.% MWCNT demonstrated an increasing piezoresistive response with increasing actuation pressure, shown in Figure 1.2. The actuators with higher nanofiller weight fractions were piezoresistive but showed a saturated response because the denser nanofiller network made the conductivity less sensitive to deformation. Hohimer and al. state that the ability to correlate specific pressure values to resistance change is an important development for self-sensing soft robotics.

As a final example, Costa et al. [15] manufactured and characterized the piezoresistive properties of MWCNT modified polycarbonate (PC) to demonstrate the material's ability to sense deformations in aerospace structures. This was demonstrated in two ways: by coating the upper surface a 3D-printed wing section made out of commercial acrylonitrile butadiene styrene plastic with a thin layer PC/MWCNT, and 3D-printing the entire wing of the similar geometry using PC/MWCNT. The wings were then subject to cyclic displacement controlled compressive loading on the wing's top surface, with three electrodes placed at the location with the highest expected deformation. Resistance measurements taken at the electrodes during deformation demonstrated a consistent, repeatable piezoresistive response over many cycles, with similar results for both uses of PC/MWCNT as an embedded sensor and a self-sensing structural material. Figure 1.3 shows the wings and the piezoresistive response measured at one of the electrodes.

1.2 Leveraging Piezoresistive Materials for MSA

Because of their innate ability to provide insight into their mechanical state, piezoresistive materials can be leveraged as a tool for MSA. In fact, piezoresistive materials have been widely explored for embedded sensing and condition monitoring. Much research has

been focused on strain sensing and damage detection in polymeric [16, 17], fiber-reinforced composite [18–20], and cementitious materials [21, 22] because of the relative ease to modify them with conductive nanofillers.

By measuring the changes in electrical resistance before and after a damage event, it has been demonstrated that damage in a piezoresistive material can be detected. For instance, Viets et al. [19] were able to detect and localize barely visible impact damage (BVID) in a glass fiber reinforced polymer laminate modified with MWCNT by measuring the resistance change between silver-ink electrodes in the thickness and in-plane directions. The results are shown in Figure 1.4.

However, while resistance change methods are proven to be able to detect damage, the spatial localization and resolution of the damage are limited. A popularly used technique to overcome this limitation is electrical impedance tomography (EIT) [23]. EIT images a spatially continuous, internal conductivity distribution of a domain from a set of voltage measurements taken at electrodes placed on the domain's boundary. Originally developed for medical imaging applications [24], EIT has been used to successfully detect and localize several different damage types in composite components [25–34], damage in thin films [16, 35], and crack propagation and moisture flow in cement [36–41]. Other advantages of EIT are that it is non-invasive and can produce images in nearly real-time.

For instance, Thomas et al. [32] extended the application of EIT to detect damage on non-planar composite structures, as work done in the field of EIT-based damage detection on composite materials had been dominated by studies on flat plates. In part of their work, Thomas et. al successfully detected conductivity changes attributed to sub-surface delamination resulting from two, low-velocity impacts on a carbon black-modified glass fiber/epoxy tube. The two impacts delivered different 10 J and 14 J of energy, which manifested as different levels of conductivity change detectable by EIT. This indicated EIT has the potential to distinguish between impact severity.

As another example, Sannamani et al. [33], in part of their work, used EIT to detect two BVID on an airfoil shaped carbon fiber reinforced polymer (CFRP) component while also accounting for the anisotropic conductivity of CFRP and utilizing non-standard electrode placement. Typically, electrodes are placed on the edges of a specimen to be imaged by

EIT. However, this approach is generally impractical for real composite structures, so in this work the electrodes were placed on the surface of the airfoil shape. The airfoil was impacted at two locations with 12 J and 15 J of energy, and the in-plane and through-thickness conductivity changes were imaged before and between each impact. While the high energy impact was easily detected by in-plane conductivity changes, it was more difficult to discern the lower energy impact since it caused less damage. It was also observed that the through-thickness conductivity change due to the impacts were undetectable since impact damage mostly affects in-plane conductivity through fiber breakage. These results were compared to another common EIT method where a scalar multiple of the conductivity tensor is sought instead of components of the conductivity tensor.

While the conductivity data afforded by EIT serve well as a damage detection technique, conductivity data are not directly useful to structural engineers seeking insight into the mechanical state of the material. Moreover, the goal of MSA is to understand the material state and damage modes in order to accurately perform damage and failure prognosis, whereas the spatial conductivity imaging in the aforementioned examples is aimed at identifying existing damage. Therefore instead, engineers seek real-time knowledge of the stresses, strains, and displacements, which is more informative for MSA and condition-based maintenance than conductivity data. In light of this shortcoming, the self-sensing inverse problem (SSIP) is a method which bridges the gap by combining the conductivity imaging capabilities of EIT with mathematical models linking strain to conductivity changes [42]. In essence, the SSIP recovers the strain state that gives rise to an observed conductivity change. This is achieved by finding the strain state that minimizes the difference between the observed conductivity distribution and a model predicted conductivity distribution. Recovery of the stress, strain, and displacement field using the SSIP has been numerically and experimentally demonstrated [43–46].

Tallman and Wang [42] first formulated the SSIP and numerically demonstrated its ability to recover the displacement field, and hence the strains, that gave rise to an observed conductivity change distribution. Conductivity change data were simulated for a piezoresistive unit cube with one end fixed and the opposite face subject to three different load cases: uniform compression, combined uniform tension and shear, and uniform shear. Gaussian white noise

was added to the simulated conductivity change data to simulate real EIT data. The results in Figure 1.7 show accurate recovery of the displacements for the compression case at 50 dB signal-to-noise ratio (SNR). At 25 dB SNR, the recovered displacements matched less closely to the exact solution but were still largely captured. For the other two cases, at 50 dB SNR the displacements were recovered well albeit not as closely as the compression case, with notable under-prediction of the displacement magnitude. At 25 dB SNR, the reconstruction quality degraded significantly. It was also found that the SSIP struggled more to accurately capture smaller displacements when the magnitude of the load was decreased because noise artifacts begin to dominate.

Hassan and Tallman [44] modified the SSIP formulation by incorporating a genetic algorithm and experimentally validated this methodology. A through-hole specimen was manufactured with 1 wt.% carbon nanofiber (CNF)-modified epoxy and loaded in tension under displacement control to 31%, 62%, and 93% of the failure displacement. At each level of displacement, the conductivity change distribution was imaged via EIT. Next, the displacement field giving rise to the conductivity change distribution was predicted via the SSIP. Using the recovered displacement field, the first principal strains and stresses were computed and compared to values obtained using digital image correlation (DIC) and standard finite element simulation. Comparison of the genetic algorithm enabled SSIP reconstructions to DIC and simulation results demonstrated good agreement in the shape and magnitude of the stress and strain fields. The results related to the first principal strains are shown in Figure 1.8.

Although the numerical and experimental demonstrations of the SSIP displacement field recovery above show promising results, there is undeniably ample opportunity for improvement when one compares the SSIP results to finite element simulation and other experimental methods like DIC. The most immediately apparent shortcoming is that the recovered displacement field is very sensitive to noise in the conductivity data. This is seen in Figure 1.7 when decreasing the conductivity data SNR resulted in the degradation in quality of the displacement field reconstruction and increased prevalence of noise artifacts. Noise artifacts are again seen in Figure 1.8 most notably as aberrations along the top edge of the test specimen. This is an intrinsic issue for inverse problems—the class of mathematical

problems the SSIP falls under. This weakness is compounded by the fact that EIT is also prone to measurement noise. The SSIP is also an underdetermined problem, meaning that the displacement field solutions the SSIP reconstructs are not unique. As a consequence, the SSIP can converge to a solution that satisfies the SSIP mathematically, but does not match the true displacement field or have any physical meaning. For instance, one common failure mode of the SSIP is under-predicting the magnitude of the displacement field. This is seen in the middle column of figure 1.7, where the shape of the displacement field is reasonably captured, but the displacement magnitude falls short of the exact solution. Furthermore, computational and experimental research employing the SSIP has to date been limited to simple geometries and test specimens, such as the ones presented in the examples above. Research demonstrating the use of the SSIP on more complex, realistic shapes is necessary to advance its readiness for practical applications.

Nevertheless, the spatially continuous strain and displacement fields recovered by the SSIP empowers engineers to make more meaningful prognostic structural analysis, for instance, by incorporating constitutive relations and failure criterion to the recovered strains. The SSIP also generally elevates the functionality of piezoresistive materials beyond just a damage detection medium. Coupled with the experimentally proven imaging capabilities of EIT, the SSIP can potentially enable near real-time monitoring of the strains and displacements throughout an entire structural component.

1.3 Sensor Data Fusion in NDE

To fully characterize a component or structure for MSA requires the measurement and evaluation of multiple physical properties, a task no single NDE sensor type or technique can achieve. Therefore, depending on the application, engineers must employ a variety of sensor types in a NDE sensor network, necessitating a method for integrating the heterogeneous datasets. The concept of synergistically integrating data from multiple sensors with the purpose enhancing data reliability and reaching a more accurate understanding of a system is known as sensor data fusion (SDF). SDF is a broad research field historically developed for military applications [47, 48]. Military applications usually involve integrating sensor data in

order to make more informed inferences regarding situation and threat assessment [49–51]. For instance, surface-to-air defense systems fuse information from radar, infrared, passive electronic support measures, identification-friend-foe sensors, electro-optic image sensors, and visual sightings to accurately detect, track, and identify aircraft for threat assessment, whereas use of only one of these inputs may prove unreliable.

Beyond military applications, SDF has expanded into diverse array of research fields, including NDE [52–54]. In recent decades, SDF has gained momentum in NDE as new sensor technologies and data acquisition platforms continue to emerge and advance. While the concept of SDF is relatively simple, its execution is challenging. SDF practitioners must develop fusion techniques that can manage data of different physical quantities, handle potentially incomplete or noisy data, identify a common reference frame among datasets, and be properly suited for the specific task at hand. Application of SDF for NDE typically involves the use of image and signal processing, heuristic, or probabilistic methods to fuse NDE data to improve the fidelity of defect detection from large scale civil and aerospace structures to small scale industrial machine parts and electronic components [55–64].

For instance, Heideklang and Shokouhi [65] fused eddy current, magnetic flux leakage, and thermography data to increase the reliability of detecting near-surface cracks in steel. These NDE techniques were selected because while all react similarly to a material defect, they are based on unrelated physical properties, meaning each is susceptible to a different source of structural noise. Thus, the NDE techniques produce complementary data and their fusion could help negate noise artifacts while enhancing defect detection. Ten grooves of increasing width and depth were machined into a steel block to simulate near-surface cracks, and the surface of the block was imaged using each NDE method. Since each dataset was a different physical quantity, the shape and magnitude of the data were normalized to allow for direct comparison. Next, signal-level fusion was performed– the three datasets were combined to create a new dataset that was then analyzed for defect detection. Several combinations of data normalization and fusion methods were evaluated, the best of which is shown in Figure 1.9, depicting the detection results for the shallowest groves. Compared to thermography, which was determined to be the best individual sensor method, the best

SDF method reduced the incidence of damage detection false positives by a factor of nearly six.

As a final example featuring a real-world NDE application of SDF, Pashoutani et al. [66] fused vertical electrical impedance (VEI) testing and ground-penetrating radar (GPR) data to enhance defect detection in a reinforced concrete bridge deck. These NDE techniques were chosen because they can be efficiently performed over large areas, and the data they generate were expected to be complementary as both measure the electrical properties of concrete while utilizing different frequencies and having different spatial resolutions. To fuse the data, a neural-network analysis determined the relationship between the VEI and GPR data. Using this relationship, the GPR data were converted into VEI format, and the data were combined. The resulting electrical impedance magnitude map (low impedance indicates high probability of damage) demonstrates an improvement in spatial resolution and also reveals defect features not visible in the individual GPR and VEI maps. A high-definition imaging (HDI) scan identifying surface cracks was also performed, and the results were superimposed over the fused data map. The HDI identified cracks correlate well with the low impedance regions on the fusion map, validating the effectiveness of the SDF method. All the aforementioned results are presented in Figure 1.10.

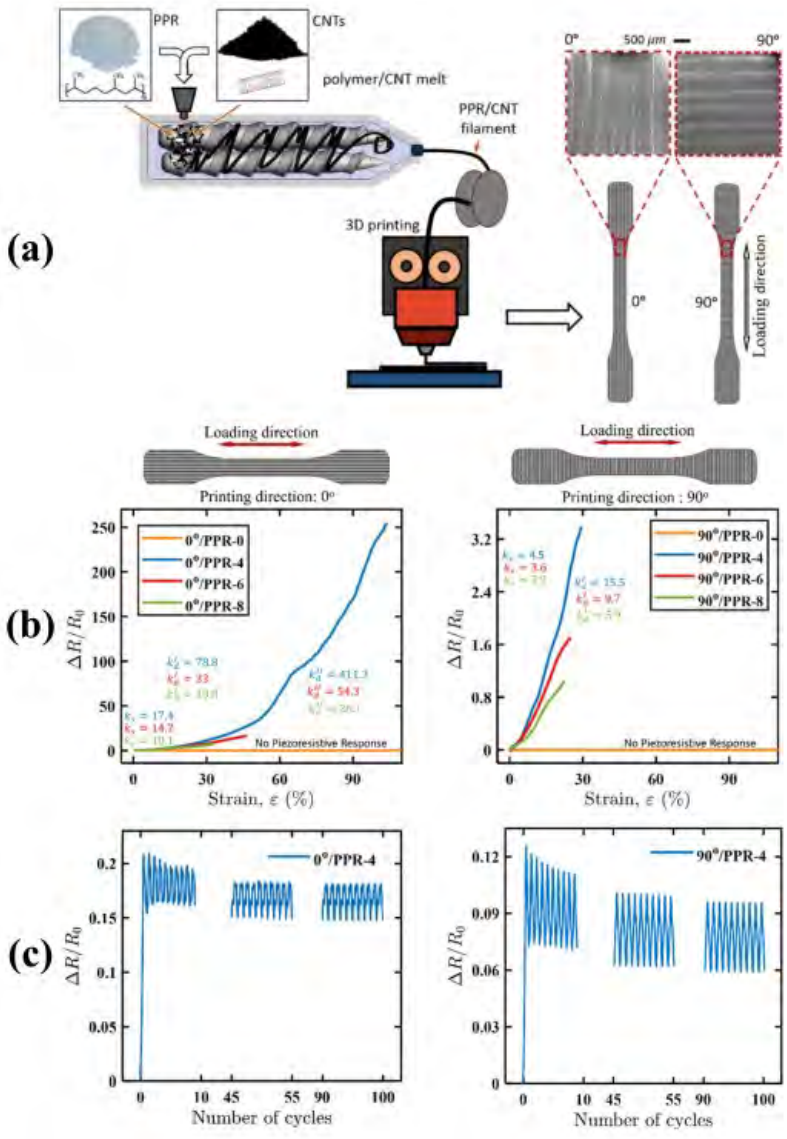

Figure 1.1. Manufacturing and characterization of piezoresistive properties of PPR/MWCNT in [12]: (a) manufacturing process, (b) tensile test results for PPR with 0, 4, 6, and 8 wt.% MWCNT, and (c) cyclic load test results for PPR with 4 wt.% MWCNT.

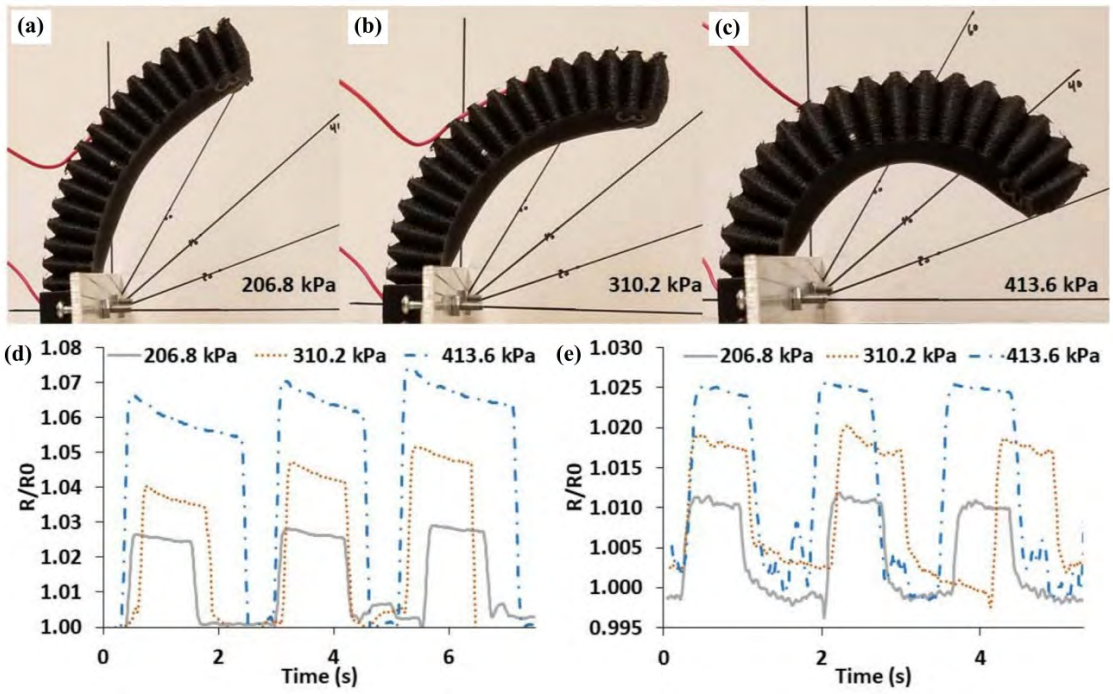

Figure 1.2. The piezoresistive response of pressurized self-sensing actuators from [13]: 1 wt.% TPU/MWCNT actuator at (a) 206.8 kPa, (b) 310.2 kPa, and (c) 413.6 kPa, (d) resistance change profiles of actuator made with (d) 1 wt.% TPU/MWCNT and (e) 2 wt.% TPU/MWCNT.

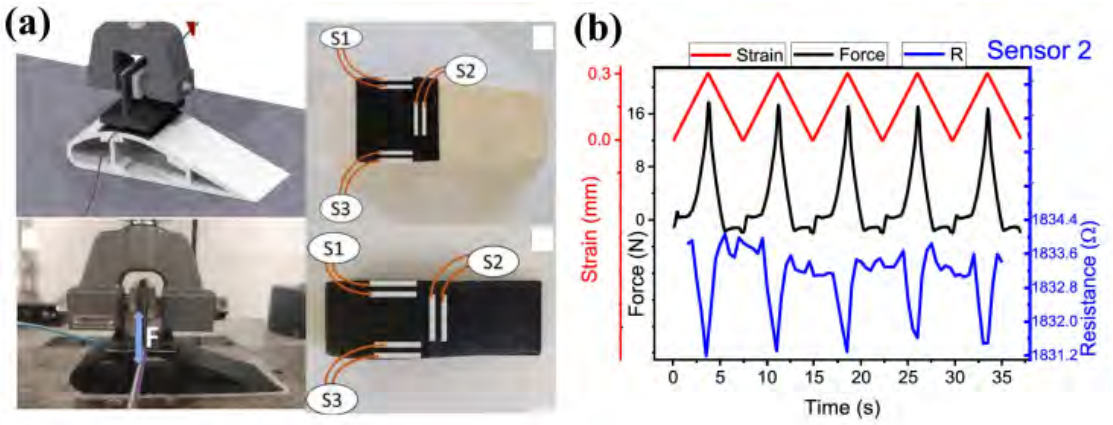

Figure 1.3. The (a) PC/MWCNT coated ABS wing section and wing section printed entirely out of PC/MWCNT instrumented with electrodes under compressive loading, and (b) the material's piezoresistive response during loading from [15].

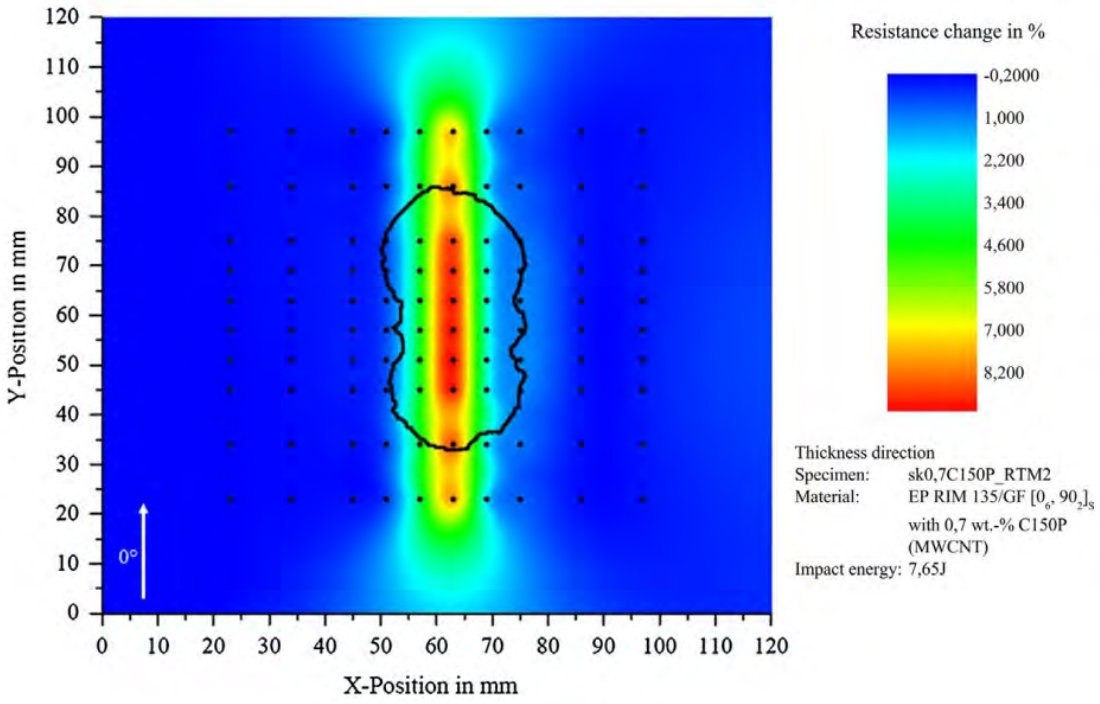

Figure 1.4. Damage map of MWCNT modified glass fiber reinforced polymer laminate obtained through electrical resistance measurements from [19]. The delamination contour obtained from an ultrasonic C-scan is superimposed onto the map. The black dots indicate electrode locations.

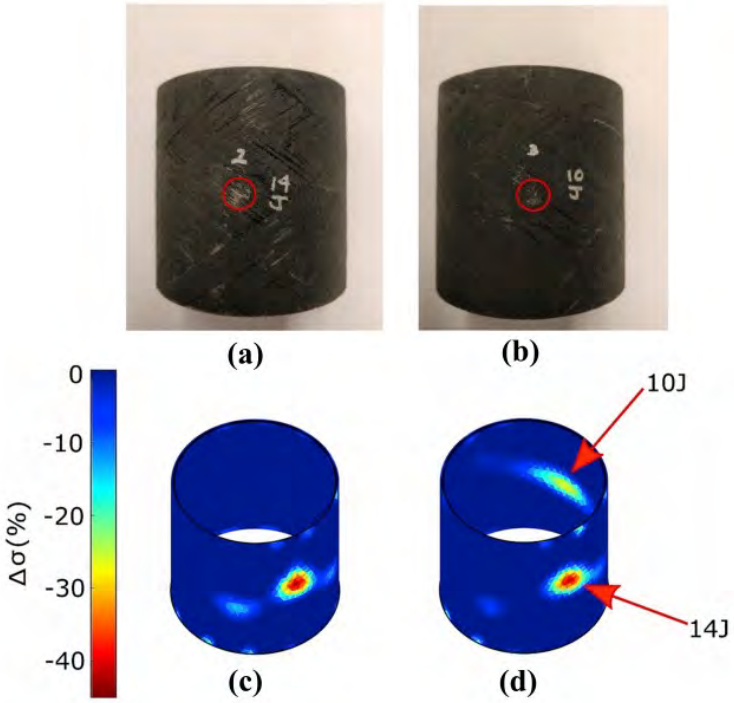

Figure 1.5. BVID damage detection on a glass fiber/epoxy tube using EIT in [32]: (a) 14 J impact damage, (b) 10 J impact damage, (c) EIT imaged conductivity change after 14 J impact, (d) EIT imaged conductivity change distribution after both impacts.

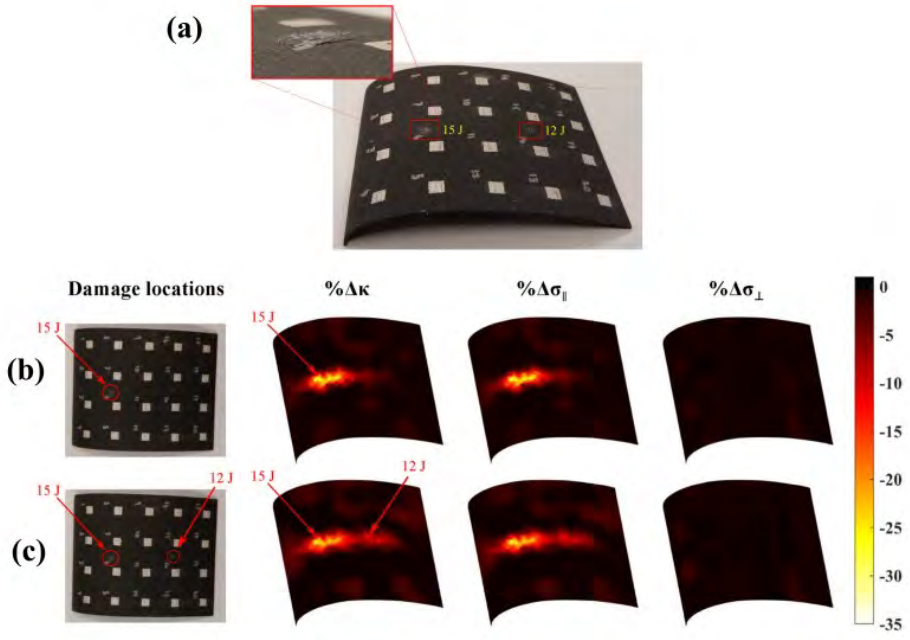

Figure 1.6. EIT BVID damage detection on a CFRP airfoil with surface mounted electrodes in [33]: (a) impact damages on surface of airfoil, and scalar multiple, in-plane conductivity, and through-thickness conductivity change imaged by EIT after (b) the 15 J impact and (c) both 12 J and 15 J impacts.

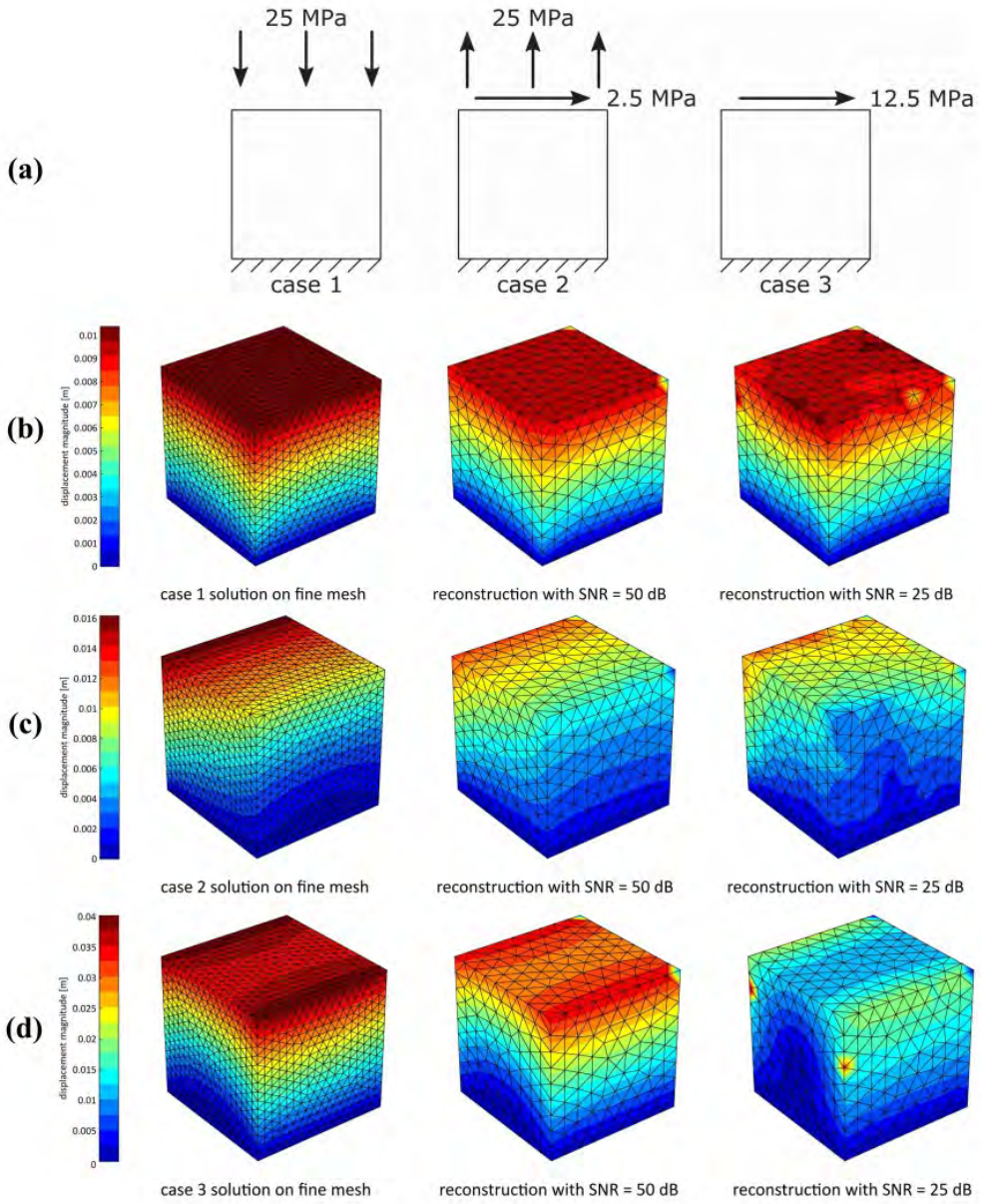

Figure 1.7. Numerical demonstration of SSIP on a unit cube from [42]. Row (a), from left to right, shows an illustration of load cases: uniform compression, uniform tension and shear, and uniform shear. The remaining rows show, from left to right, the exact displacement solution, and the SSIP displacement field reconstruction for conductivity data with 50 dB and 25 dB SNR for the (b) uniform compression case, (c) combined uniform tension and shear case, and (d) uniform shear case.

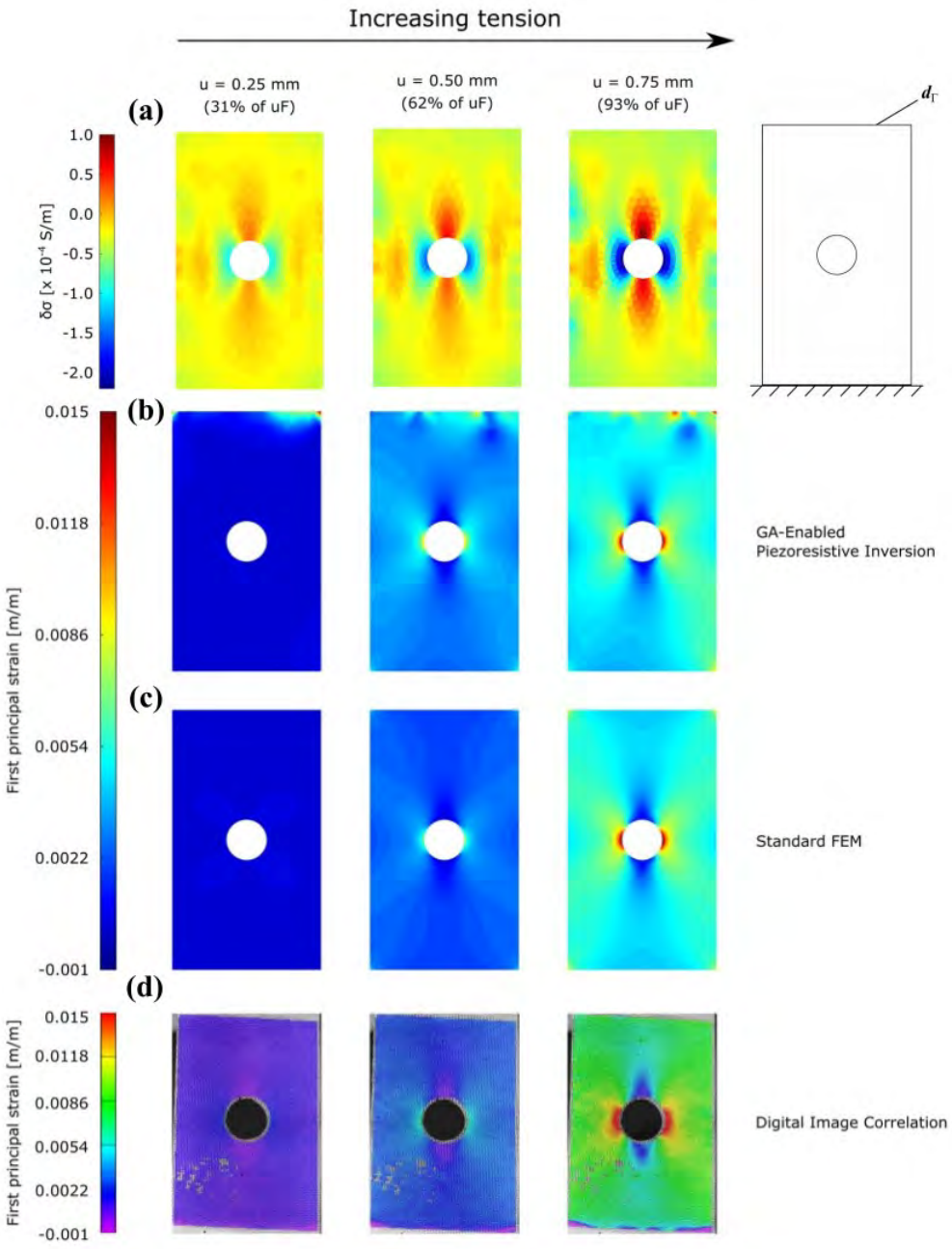

Figure 1.8. Experimental application of genetic algorithm enabled SSIP from [44] on a tension loaded open-hole test specimen. For each level of tension, (a) an illustration of loading and EIT imaged internal conductivity change distribution under increasing tension, and the first principal strains (b) recovered via genetic algorithm enabled SSIP (c) simulated using finite element analysis, and (d) derived from DIC measurements are shown.

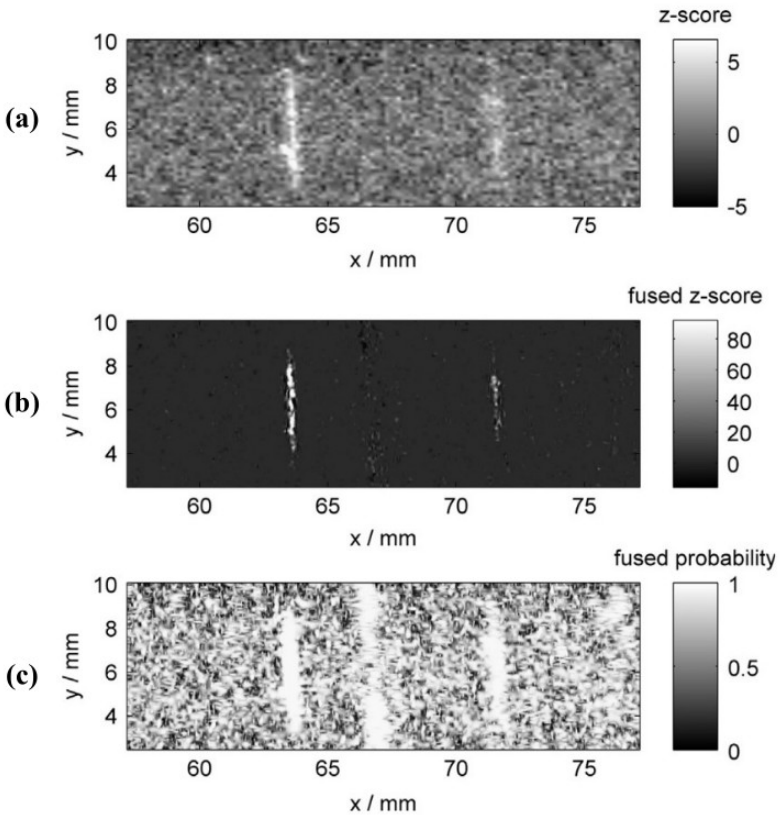

Figure 1.9. From [65], the detection of shallow grooves in steel simulating near surface cracks using (a) thermography data, (b) best performing SDF method of ECT, MFL, and thermography, (c) worst performing SDF method.

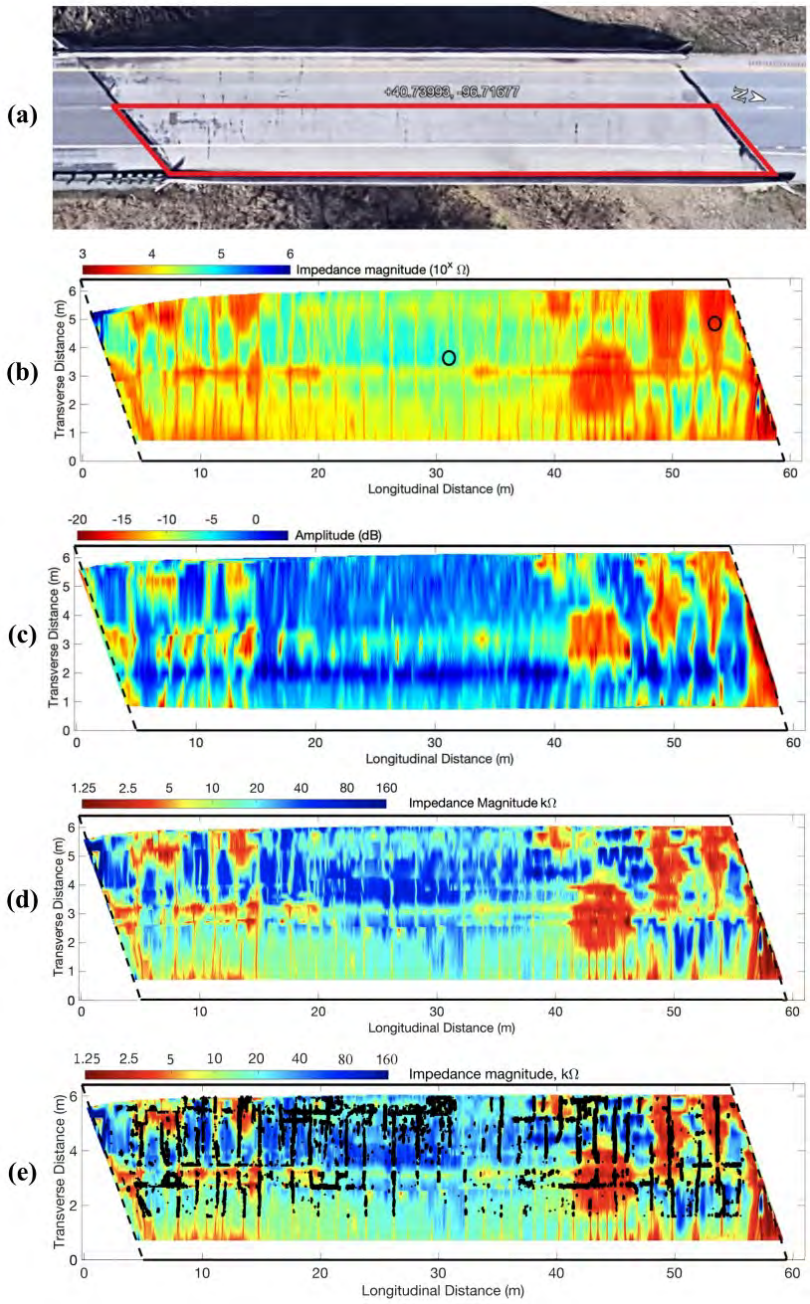

Figure 1.10. An example of SDF being applied to a bridge from [66] featuring (a) satellite image of bridge, (b) VEI map, (c) GPR map, (d) fused VEI and GPR map, and (e) the fused VEI and GPR map overlaid with cracks detected with HDI.

2. PROBLEM STATEMENT AND RESEARCH GOAL

From the discussion in the previous chapter, it is evident that piezoresistive materials are a promising tool to aid in the pursuit of MSA. Out of the many approaches being actively explored to leverage piezoresistive materials for condition monitoring of structural components and systems, the SSIP is of special interest. Recovery of the spatially continuous strains and displacements via the SSIP empowers engineers to perform more accurate failure prognosis and remaining lifetime estimation, which are the preeminent goals of MSA. However, it is clear from current work on the SSIP that there is a need for further research investigating methods to improve the accuracy and reliability of the recovered strain and displacement fields, especially when the electrical data the SSIP solely relies on for its predictions contains high levels of noise. Additionally, current applications of the SSIP are limited to simple geometries or small scale experimental specimens. Based on these opportunities to advance the state-of-the-art, the following Problem Statement and Research Goal are presented.

2.1 Problem Statement

The SSIP is a challenging mathematical problem to solve, and the accuracy of the displacement and strain field recovered from the conductivity changes in not guaranteed. As described in the previous chapter, the SSIP recovered displacement field is sensitive to noise and outliers in the conductivity data and prone to under-prediction of the displacement magnitude. In the field of NDE, it is well known that no single NDE sensor or technique possesses the ability to fully characterize the state of a material. Researchers studying NDE defect detection have demonstrated that SDF of datasets from NDE sensors measuring different physical quantities can improve the accuracy and reliability of defect detection. This line of thought can be extended to the SSIP: the fusion of conductivity data with some other complementary data can potentially improve the accuracy and reliability of the strain and displacement fields recovered via the SSIP. Furthermore, application of the SSIP to date has been limited to relatively simple geometries and load cases. Overall, enhancing the accuracy and reliability of the SSIP and demonstrating its efficacy on more realistic load cases are

necessary prior to more advanced experimental implementation and eventual deployment as a widely used tool for MSA.

2.2 Research Goals

The goal of this research is to develop the mathematical methods that allow the fusion of conductivity data with complementary sensor data within the SSIP framework and to computationally demonstrate the capacity of SDF to enhance the accuracy and reliability of the SSIP recovered strain and displacement fields. Specifically, the fusion of conductivity data with displacement and strain data, made available through displacement and strain gauges, respectively, is investigated. To clarify, SDF of displacement and strain data with conductivity data is explored separately. Additionally, this work expands the computational application of the SSIP to more practical geometries representing real structural components and their operational loads cases. The goals are summarized in the list below.

- Develop a method to fuse resistivity data with displacement data.
- Develop a method to fuse resistivity data with strain data.
- Demonstrate the efficacy of SDF in improving the accuracy and reliability of the SSIP displacement field recovery.
- Demonstrate the SSIP displacement field recovery on complex geometries and loads.

2.3 Thesis Organization

Having presented the problem statement and research goal, the remainder of the thesis is structured as follows. First, the mathematical formulation of the SSIP is explained in detail, which includes a discussion of the piezoresistivity model used in this work. Second, the method in which displacement and strain data are fused with conductivity data are presented. Third, the computational experimental procedure is presented. This is followed by a discussion of the computational experimental results. Lastly, this thesis closes with a summary, conclusions, and outlook for future work.

3. THE SELF-SENSING INVERSE PROBLEM

3.1 Introduction

The SSIP, as its name suggests, is an inverse problem. At a high level, an inverse problem concerns determining, from a set of measurements, the factors that caused them—seeking the cause from the measured effect. EIT is one example, where the internal conductivity distribution that caused the measured boundary voltages is being sought. In the context of structural engineering, this entails finding the unknown characteristics of a structural system from the outputs, or measurements, of that system [67]. Similarly, the goal of the SSIP is to reconstruct the deformation induced strain state that gave rise to an observed conductivity change in a piezoresistive material. Here, the conductivity changes are the measured outputs, and the strain state is the unknown characteristic being determined. Mathematically, the SSIP is a minimization problem. Reconstructing the underlying strain state involves minimizing the difference between the observed conductivity distribution and the conductivity distribution predicted by a model. The observed conductivity is available through the methods such as EIT. To obtain the model predicted conductivity, one must quantify the relationship between strains and conductivity for the specific piezoresistive material being used. The mathematical relationship linking conductivity to strains is called a piezoresistivity model.

3.2 Piezoresistivity Model

Much research has been conducted to model the piezoresistive effect, largely for conductive-nanofiller modified composite materials. The models that have been developed can be classified into three general categories: equivalent network based [68–71], computational micromechanics based [72–75], or analytical [76–79]. Equivalent resistor network based models simulate individual conductive nanofillers in the microscale domain. Computational micromechanics based models simulate both the nanofillers and the enveloping matrix material. Analytical models depart from simulating individual nanofillers and instead express

conductivity (or resistivity) as a function of parameters taken from manufacturing data, experimental characterization, and the material strain state.

Herein, the analytical piezoresistivity model developed by Koo and Tallman [80] is used, given in equation (3.1) below. This piezoresistivity model was selected for a few reasons. First, it is because analytical piezoresistivity models have much lower computational cost than equivalent network and computational micromechanics models since individual nanofillers are not being modeled. Second, this model predicts resistivity changes from general deformations. This means that it is applicable to complex load cases and strain states at macroscales, unlike the majority of piezoresistivity models which are limited to the microscale. Third, this model is compatible with EIT because the model assumes resistivity change is a scalar quantity. The conductivity (or resistivity) distributions imaged by EIT are traditionally reported as scalars. Lastly, this model has been experimentally validated in [80] for selected weight fractions of CNF-modified epoxy. It was demonstrated that the model predicted a resistivity change distribution for an open-hole tension test specimen that was comparable to the resistivity change distribution imaged by EIT.

$$\Delta\rho = \kappa(\varepsilon_{11}+\varepsilon_{22}+\varepsilon_{33}) + (\Pi_1+\Pi_2)(\varepsilon_{11}^2+\varepsilon_{22}^2+\varepsilon_{33}^2) + 2\Pi_1(\varepsilon_{11}\varepsilon_{22}+\varepsilon_{33}\varepsilon_{11}+\varepsilon_{22}\varepsilon_{33}) + 2\Pi_2(\varepsilon_{12}^2+\varepsilon_{31}^2+\varepsilon_{23}^2) \quad (3.1)$$

In the equation above, $\Delta\rho$ is the resistivity change in ohm-meters ($\Omega \cdot \mathrm{m}$), the terms denoted with ε are components of the infinitesimal strain tensor, and κ, Π_1, and Π_2 are piezoresistive constants determined from curve-fitting experimental resistivity change-strain data.

To elaborate on the determination of the piezoresistive constants, the following is brief summary of the work done in [80]. Equation (3.1) is a general mathematical model with undetermined coefficients. To find the coefficients, a process analogous to finding a line of best fit for scatter plot data is performed. Dog-bone and v-notched specimens were manufactured from a piezoresistive material. The dog-bone specimen was then loaded uniaxially, and the v-notched specimen was loaded in a state of pure shear. Uniaxial and pure shear were

chosen because the strain state induced by these loadings isolated different piezoresistivity constants. The resistivity of the specimens were determined at several levels of uniaxial and shear strain, from which axial and shear resistivity-strain plots were generated. Finally, the piezoresistive constants were selected using the MATLAB '*cftool*' command such that the model best fit the data in the plots.

Before proceeding with the mathematical formulation of the SSIP, important assumptions and caveats associated with the model are acknowledged. This model was developed assuming linear elastic material behavior and infinitesimal strains. Additionally, because the model is a curve fit of experimental data, it is only expected to be accurate within the range of strains the for which the model was defined.

3.3 Mathematical Formulation of the SSIP

Prior discussion about the SSIP had been in terms of electrical conductivity. However, since the piezoresistivity model chosen for this work is in terms of resistivity, the following mathematical formulation (and work in later sections) will proceed in terms of resistivity. Additionally, it is assumed in this work that the experimentally observed resistivity distribution is available through the use of EIT. However, EIT is not the focus of this research and, therefore, will not be treated in detail. Interested readers are directed to the relevant literature presented here and in section 1.2 [23, 81].

The SSIP is mathematically formulated as a minimization problem as shown in equation (3.2), where ρ is the experimentally observed resistivity distribution (as obtained via, for example, EIT), $f(\varepsilon_{ij})$ is the model predicted resistivity distribution, and ε^*_{ij} is the strain state that satisfies the minimization. In other words, ε^*_{ij} is the strain state that, when provided to the piezoresistivity model, gives rise to the observed resistivity distribution.

$$\varepsilon^*_{ij} = \arg\min_{\varepsilon_{ij}}(\|\rho - f(\varepsilon_{ij})\|^2) \tag{3.2}$$

Note that the ρ in equation (3.2) is an absolute resistivity, but the piezoresistivity model predicts a resistivity change for a given strain tensor. To convert the model predicted resistivity change into an absolute resistivity, a baseline resistivity, ρ_0 must be added to

the resistivity change, explicitly expressed in equation (3.3). This baseline resistivity would be obtained from the material in the undeformed state.

$$f(\varepsilon_{ij}) = \Delta\rho + \rho_0 \tag{3.3}$$

Proceeding with the minimization, $f(\varepsilon_{ij})$ is linearized via a Taylor series expansion about an initial estimate of the strain state, ε_{ij}^0, as shown in equation (3.4). Substituting equation (3.4) back into equation (3.2) produces equation (3.5). Consider the derivative term, $\partial f(\varepsilon_{ij}^0)/\partial\varepsilon_{ij}$. Because the piezoresistivity model used in this work is a continuous and differentiable function of the infinitesimal strain tensor, the derivative term is computed analytically, given explicitly in equation (3.6). The derivatives with respect to the shear strains are equivalent due to the symmetry of the infinitesimal strain tensor. In cases where a non-analytical or non-differentiable model is used, the derivative can be computed using any appropriate numerical method.

$$f(\varepsilon_{ij}) \cong f(\varepsilon_{ij}^0) + \frac{\partial f(\varepsilon_{ij}^0)}{\partial\varepsilon_{ij}}(\varepsilon_{ij} - \varepsilon_{ij}^0) \tag{3.4}$$

$$\varepsilon_{ij}^* = \arg\min_{\varepsilon_{ij}} \left(\left\| \rho - f(\varepsilon_{ij}^0) - \frac{\partial f(\varepsilon_{ij}^0)}{\partial\varepsilon_{ij}}(\varepsilon_{ij} - \varepsilon_{ij}^0) \right\|^2 \right) \tag{3.5}$$

$$\begin{aligned}
\frac{\partial f(\varepsilon_{ij})}{\partial\varepsilon_{11}} &= \kappa + 2(\Pi_1 + \Pi_2)\varepsilon_{11} + 2\Pi_1(\varepsilon_{22} + \varepsilon_{33}) \\
\frac{\partial f(\varepsilon_{ij})}{\partial\varepsilon_{22}} &= \kappa + 2(\Pi_1 + \Pi_2)\varepsilon_{22} + 2\Pi_1(\varepsilon_{11} + \varepsilon_{33}) \\
\frac{\partial f(\varepsilon_{ij})}{\partial\varepsilon_{33}} &= \kappa + 2(\Pi_1 + \Pi_2)\varepsilon_{33} + 2\Pi_1(\varepsilon_{11} + \varepsilon_{22}) \\
\frac{\partial f(\varepsilon_{ij})}{\partial\varepsilon_{12}} &= \frac{\partial f(\varepsilon_{ij})}{\partial\varepsilon_{21}} = 4\Pi_2\varepsilon_{12} \\
\frac{\partial f(\varepsilon_{ij})}{\partial\varepsilon_{13}} &= \frac{\partial f(\varepsilon_{ij})}{\partial\varepsilon_{31}} = 4\Pi_2\varepsilon_{13} \\
\frac{\partial f(\varepsilon_{ij})}{\partial\varepsilon_{23}} &= \frac{\partial f(\varepsilon_{ij})}{\partial\varepsilon_{32}} = 4\Pi_2\varepsilon_{23}
\end{aligned} \tag{3.6}$$

By defining the difference between the observed and model determined resistivity as $\delta\rho = \rho - f(\varepsilon_{ij})$ and the difference between the true strain and estimated strain as $\delta\varepsilon_{ij} = \varepsilon_{ij} - \varepsilon^0_{ij}$, equation (3.7) is obtained.

$$\varepsilon^*_{ij} = \arg\min_{\varepsilon_{ij}} \left(\left\| \delta\rho - \frac{\partial f(\varepsilon^0_{ij})}{\partial \varepsilon_{ij}} \delta\varepsilon_{ij} \right\|^2 \right) \tag{3.7}$$

At this point, equation (3.7) now states that if we can find the strain increment $\delta\varepsilon_{ij}$ that causes the difference between the observed and model determined resistivity, $\delta\rho$, we satisfy the minimization and can move toward determining the underlying strain state of the material.

3.4 Finite Element Discretization

Next, the minimization is adapted to be applicable to a finite element mesh. This is done because EIT customarily recovers the resistivity distribution of a domain discretized by a finite element mesh, so it is logical to perform the SSIP on the same mesh. Further, solving the SSIP on non-trivial shapes requires some discretization of the solution space, and the finite element method is easily integrated into this process. To clarify, the finite element method is not being used to solve differential equations. The minimization is simply written in terms of a discretized displacement field. Stated directly, we seek the strain state that minimizes the difference between the observed and predicted resistivity for each element in a finite element mesh.

Continuing with the finite element adaptation, in this work, trilinear hexahedral elements are used because they are commonly used in structural analysis simulations and generally produce more accurate results than linear tetrahedral elements. Next, recall the definition of the infinitesimal strain tensor in equation (3.8). Also recall the finite element forms of displacement, u_i, and the displacement gradient, $\partial u_i / \partial x_j$, given as equations (3.9) and (3.10), respectively.

$$\varepsilon_{ij} = \frac{1}{2} \left(\frac{\partial u_i}{\partial x_j} + \frac{\partial u_j}{\partial x_i} \right) \tag{3.8}$$

$$u_{\mathrm{ei}} = \sum_A N^A d^A_{\mathrm{ei}} \tag{3.9}$$

$$\frac{\partial u_{\mathrm{ei}}}{\partial x_{\mathrm{j}}} = \sum_A \frac{\partial N^A}{\partial \xi_k} \frac{\partial \xi_k}{\partial x_{\mathrm{j}}} d^A_{\mathrm{ei}} \tag{3.10}$$

In the above equations, u_{ei} is the displacement in the i-direction of the eth element, N^A is the trilinear finite element interpolation function for the Ath node of a hexahedral element, and d^A_{ei} is the displacement in the i-direction of the Ath node of the eth element. The summation $\sum_A(\cdot)$ runs from one to eight for hexahedral elements. The trilinear interpolation functions are given in equation (3.11).

$$\begin{aligned}
N^1 &= \frac{1}{8}(1-\xi_1)(1-\xi_2)(1-\xi_3) \\
N^2 &= \frac{1}{8}(1+\xi_1)(1-\xi_2)(1-\xi_3) \\
N^3 &= \frac{1}{8}(1+\xi_1)(1+\xi_2)(1-\xi_3) \\
N^4 &= \frac{1}{8}(1-\xi_1)(1+\xi_2)(1-\xi_3) \\
N^5 &= \frac{1}{8}(1-\xi_1)(1-\xi_2)(1+\xi_3) \\
N^6 &= \frac{1}{8}(1+\xi_1)(1-\xi_2)(1+\xi_3) \\
N^7 &= \frac{1}{8}(1+\xi_1)(1+\xi_2)(1+\xi_3) \\
N^8 &= \frac{1}{8}(1-\xi_1)(1+\xi_2)(1+\xi_3)
\end{aligned} \tag{3.11}$$

However, the use of trilinear hexahedral elements and their interpolation functions conflicts with the treatment of resistivity as a constant value for each element. Since each element of the finite element mesh will possess a single constant resistivity value, we expect the strains of the element to defined by a single infinitesimal strain tensor such that the contraction in the right term of the difference results in a constant value. Yet, $\partial u_{\mathrm{ei}}/\partial x_{\mathrm{j}}$ is not constant, resulting in non-constant components of $\varepsilon_{\mathrm{ij}}$. To overcome this problem, a

strain tensor with constant components is obtained by computing the volumetric average of $\partial u_{\mathrm{ei}}/\partial x_{\mathrm{j}}$, as shown in equation (3.12).

$$\frac{\partial \bar{u}_{\mathrm{ei}}}{\partial x_{\mathrm{j}}} = \frac{\int_{v_{\mathrm{e}}} \sum_A \frac{\partial N^A}{\partial \xi_k}\frac{\partial \xi_k}{\partial x_{\mathrm{j}}} d^A_{\mathrm{ei}}\, \mathrm{d}v_{\mathrm{e}}}{v_{\mathrm{e}}} = \sum_A \frac{\int_{v_{\mathrm{e}}} \frac{\partial N^A}{\partial \xi_k}\frac{\partial \xi_k}{\partial x_{\mathrm{j}}}\, \mathrm{d}v_{\mathrm{e}}}{v_{\mathrm{e}}} d^A_{\mathrm{ei}} = \sum_A \frac{\partial \bar{N}^A}{\partial x_{\mathrm{j}}} d^A_{\mathrm{ei}} \tag{3.12}$$

In the above, the bar accent signifies a volumetric average and v_{e} is the volume of the eth element. The third term of the equality exploits the fact that the integral of the sum of functions is equal to the sum of the integrals of the same function. The d^A_{ei} term is also moved outside of the integral because the nodal displacements are constant.

The final result of equation (3.12) is substituted into equation (3.8), arriving at equation (3.13), where the volume averaged infinitesimal strain tensor is now expressed in terms of interpolation functions and nodal displacements.

$$\varepsilon_{\mathrm{ij}} = \frac{1}{2}\left(\sum_A \frac{\partial \bar{N}^A}{\partial x_{\mathrm{j}}} d^A_{\mathrm{ei}} + \sum_A \frac{\partial \bar{N}^A}{\partial x_{\mathrm{i}}} d^A_{\mathrm{ej}}\right) \tag{3.13}$$

Inserting equation (3.13) into equation (3.7) yields equation (3.14). Note that the subscript e is now included in $\varepsilon^*_{\mathrm{e,ij}}$ and ρ_{e} to indicate that the minimization is defined for the eth element of the finite element mesh.

$$\varepsilon^*_{\mathrm{e,ij}} = \arg\min_{\varepsilon_{\mathrm{ij}}} \left(\left\| \delta\rho_{\mathrm{e}} - \frac{\partial f(\varepsilon^0_{\mathrm{ij}})}{\partial \varepsilon_{\mathrm{ij}}} \frac{1}{2}\left(\sum_A \frac{\partial \bar{N}^A}{\partial x_{\mathrm{j}}} \delta d^A_{\mathrm{ei}} + \sum_A \frac{\partial \bar{N}^A}{\partial x_{\mathrm{i}}} \delta d^A_{\mathrm{ej}}\right)\right\|^2\right) \tag{3.14}$$

Next, recognize that $\partial f(\varepsilon^0_{\mathrm{ij}})/\partial \varepsilon_{\mathrm{ij}}$ is the partial derivative of a scalar with respect to a symmetric tensor. This results in another symmetric tensor. Also, note that the two terms being summed are the displacement gradient and its transpose. Since the contraction of symmetric tensor with a second tensor is equal to the contraction of the same symmetric tensor with the transpose if the same second tensor, equation (3.14) can be condensed into equation (3.15).

$$\varepsilon^*_{\mathrm{e,ij}} = \arg\min_{\varepsilon_{\mathrm{ij}}} \left(\left\| \delta\rho_{\mathrm{e}} - \frac{\partial f(\varepsilon^0_{\mathrm{ij}})}{\partial \varepsilon_{\mathrm{ij}}} \sum_A \frac{\partial \bar{N}^A}{\partial x_{\mathrm{j}}} \delta d^A_{\mathrm{ei}}\right\|^2\right) \tag{3.15}$$

Equation (3.15) will now be re-expressed so that the minimization encompasses the entire finite element mesh. First, $\partial f(\varepsilon_{\mathrm{ij}}^0)/\partial\varepsilon_{\mathrm{ij}}$ is moved inside the summation. Next, the explicit summation is replaced with linear algebra as the multiplication of a row and column vector for the eth element. The contraction of $\partial f(\varepsilon_{\mathrm{ij}}^0)/\partial\varepsilon_{\mathrm{ij}}$ with $\partial\bar{N}^A/\partial x_{\mathrm{j}}$ is represented as a row vector, $\boldsymbol{g}_{\mathbf{e}}$, and the nodal displacement is represented as a column vector, $\delta\boldsymbol{d}_{\mathbf{e}}$. The conversion from explicit summation to linear algebra is shown in equation (3.16).

$$\frac{\partial f(\varepsilon_{\mathrm{ij}}^0)}{\partial\varepsilon_{\mathrm{ij}}}\sum_A\frac{\partial\bar{N}^A}{\partial x_{\mathrm{j}}}\delta d_{\mathrm{ei}}^A=\sum_A\frac{\partial f(\varepsilon_{\mathrm{ij}}^0)}{\partial\varepsilon_{\mathrm{ij}}}\frac{\partial\bar{N}^A}{\partial x_{\mathrm{j}}}\delta d_{\mathrm{ei}}^A=\begin{bmatrix}g_{\mathrm{e1}}^1 & g_{\mathrm{e2}}^1 & \dots & g_{\mathrm{e3}}^8\end{bmatrix}\begin{bmatrix}\delta d_{\mathrm{e1}}^1\\ \delta d_{\mathrm{e2}}^1\\ \vdots\\ \delta d_{\mathrm{e3}}^8\end{bmatrix} \tag{3.16}$$

The elemental $\boldsymbol{g}_{\mathbf{e}}$ and $\delta\boldsymbol{d}_{\mathbf{e}}$ vectors are reassembled into a global matrix, $\boldsymbol{G}$, and global nodal displacement increment vector, $\delta\boldsymbol{d}$, such that the element level contractions are preserved. The minimization is restated for the entire finite element mesh in equation (3.17). Now, instead of seeking a the strains, we seek the global displacement vector, $\boldsymbol{d}^*$, that satisfies the minimization. The transition from $\varepsilon_{\mathrm{ij}}^*$ to $\boldsymbol{d}^*$ is a consequence of the infinitesimal strain tensor being expressed in terms of nodal displacements as part of the finite element formulation. Note that the boldface $\delta\boldsymbol{\rho}$ is now a global vector of element resistivities.

$$\boldsymbol{d}^*=\arg\min_d(\|\delta\boldsymbol{\rho}-\boldsymbol{G}\delta\boldsymbol{d}\|^2) \tag{3.17}$$

Solving for $\boldsymbol{d}^*$ is an iterative process. The process begins by setting an initial estimate of the global displacement vector. Since we assume no prior knowledge of the state of the material, the initial nodal displacement estimate is set as the zero vector, $\boldsymbol{d}=\mathbf{0}$. The nodal displacement estimate is used to calculate the initial estimate of the strain tensor, $\varepsilon_{\mathrm{ij}}^0$, model predicted resistivity, $f(\varepsilon_{\mathrm{ij}}^0)$, and the piezoresistivity model derivative, $\partial f(\varepsilon_{\mathrm{ij}}^0)/\partial\varepsilon_{\mathrm{ij}}$, for each element. The global $\boldsymbol{G}$ matrix and $\delta\boldsymbol{\rho}$ vector are then assembled.

To proceed, we must solve for $\delta\boldsymbol{d}$. To do so, we must recognize that recovering the three independent components of displacement from a scalar resistivity is an underdetermined

problem. With this in mind, the method of least squares with regularization is employed, as shown in equation (3.18), where $\boldsymbol{R}$ is the regularization term, and α is the scalar regularization parameter that controls the degree of regularization.

$$\delta \boldsymbol{d} = (\boldsymbol{G}^T \boldsymbol{G} + \alpha^2 \boldsymbol{R}^T \boldsymbol{R})^{-1} \boldsymbol{G}^T \delta \boldsymbol{\rho} \tag{3.18}$$

Here, the application of displacement boundary conditions is addressed. The columns of $\boldsymbol{G}$ corresponding to nodal degrees of freedom subject to a displacement boundary condition are removed prior to the solving for $\delta \boldsymbol{d}$. Thus, the number of columns of $\boldsymbol{G}$ and rows of $\delta \boldsymbol{d}$ are reduced. Likewise, the rows and columns of $\boldsymbol{R}$ must be removed to retain dimensional compatibility. The reduced dimension $\boldsymbol{G}$, $\boldsymbol{R}$, and $\delta \boldsymbol{d}$ are denoted as $\hat{\boldsymbol{G}}$, $\hat{\boldsymbol{R}}$, $\delta \hat{\boldsymbol{d}}$, and equation (3.18) is rewritten as equation (3.19). After equation (3.19) is solved, the known displacement values for these degrees of freedom are manually reassembled back into $\delta \hat{\boldsymbol{d}}$, restoring the vector to $\delta \boldsymbol{d}$. This routine is similar to standard finite element simulation.

$$\delta \hat{\boldsymbol{d}} = (\hat{\boldsymbol{G}}^T \hat{\boldsymbol{G}} + \alpha^2 \hat{\boldsymbol{R}}^T \hat{\boldsymbol{R}})^{-1} \hat{\boldsymbol{G}}^T \delta \boldsymbol{\rho} \tag{3.19}$$

After $\delta \boldsymbol{d}$ is calculated, $\boldsymbol{d}$ is updated as $\boldsymbol{d}^{n+1} = \boldsymbol{d}^n + \delta \boldsymbol{d}$. The updated displacement vector is then used to calculate the next estimates of ε_{ij}^n, $f(\varepsilon_{ij}^n)$, and $\partial f(\varepsilon_{ij}^n)/\partial \varepsilon_{ij}$ so that the next iteration can proceed. With each iteration, the residual converges to zero, and iterations proceed until the relative residual term, given in equation (3.20), is deemed sufficiently minimized. In the equation below, $\bar{r}$ is the relative residual, r is the residual, and ϵ is the convergence criteria.

$$\begin{aligned} \bar{r}^n &= \left| \frac{r^n - r^{n-1}}{r^{n-1}} \right| \leq \epsilon \\ r^n &= \|\delta \boldsymbol{\rho}^n - \boldsymbol{G} \delta \boldsymbol{d}^n\|^2 \end{aligned} \tag{3.20}$$

3.5 Mathematical Limitations of the SSIP

By nature of being an inverse problem, the SSIP is inherently ill-posed. A well-posed problem fulfills the following three criteria: the problem has a solution, the solution is unique, and the solution's behavior changes continuously with the initial conditions. The SSIP violates the latter two criteria. The second criterion is violated because while a solution exists for the SSIP, it is not unique because the SSIP is also underdetermined. An underdetermined system has more degrees of freedom than equations to constrain them. In the case of the SSIP, there are more nodal displacement degrees of freedom than there are elemental resistivity data. The third criterion is violated because the SSIP is highly sensitive to noise and outliers in the resistivity data. In other words, small perturbations in the resistivity data will likely cause large differences in the recovered displacement field.

An essential method to combat the ill-posed and underdetermined nature of the SSIP is to employ regularization, as mentioned at the end of the previous section. Regularization aims to stabilize the inverse problem by imposing an assumed condition or prior knowledge of the solution space. In this work, the discrete Laplacian, denoted as $\boldsymbol{L}$ and defined in equation (3.21), is used for regularization; therefore, $\boldsymbol{R}$ in equation (3.18) is now equal to $\boldsymbol{L}$. Note that in equation (3.21) and for following mentions of $\boldsymbol{L}_{\mathrm{ij}}$, index notation is not being used.

$$\boldsymbol{L} = L_{\mathrm{ij}} = \begin{cases} \mathrm{degree}(\Omega_n) & \text{if } i = j. \\ -1 & \text{if } i = j \text{ and } \Omega_{\mathrm{i}} \text{ is adjacent to } \Omega_{\mathrm{j}}. \\ 0 & \text{otherwise} \end{cases} \tag{3.21}$$

Since the SSIP seeks the global displacement field vector, $\boldsymbol{L}$ is a square matrix with the number of rows and columns equal to the total number of displacement degrees of freedom. The total number of displacement degrees of freedom is equal to the product of the total number of finite element mesh nodes and the number of spatial dimensions of the geometry. Each diagonal entry counts the number of nodes adjacent to node Ω_n. For the off-diagonal terms, $L_{\mathrm{ij}} = L_{\mathrm{ji}} = -1$ whenever the ith and jth nodes are adjacent. Otherwise, $L_{\mathrm{ij}} = L_{\mathrm{ji}} = 0$.

$\boldsymbol{L}$ is chosen because it promotes a smoothly varying solution space, which is a reasonable assumption for a displacement field.

Despite regularization allowing for a solution to the SSIP to be found, the displacement field obtained is still not unique. In other words, it is still possible for the SSIP to produce a displacement field solution that mathematically satisfies the minimization in equation (3.17), but does not match the true displacement field. This fact motivates the research goal: we seek additional means to guide the SSIP toward the correct displacement field solution, and SDF is a promising avenue to achieve this goal given its efficacy in the aforementioned literature.

4. SENSOR DATA FUSION

4.1 Problem Identification

Since the SSIP aims to recover the displacement field and strain state from resistivity data, it is natural to consider fusing resistivity data with displacement or strain data provided by other sensors. Thus, the incorporation of SDF in effort to improve the SSIP displacement field recovery will hereon be called the SSIP SDF problem. In theory, additional strain or displacement data could help guide the SSIP toward the physically correct displacement field, and hence the correct strain state, that gives rise to an observed resistivity change distribution. This thesis explores the effect of fusing resistivity data with displacement data, as well as fusing resistivity data with strain data, on the SSIP displacement field recovery. Simultaneous fusion of all three data types is not investigated. Prior to describing the mathematical methods in which the data are fused, we first connect the SSIP SDF problem to the wider body of SDF research and discuss the fundamental considerations prior to employing SDF.

SDF is the process of combining data to refine state estimates and predictions [82]. This overarching objective remains constant across all applications SDF has been adopted for. However, depending on the particular application, the data fusion terminology, architecture, and common algorithms can vary. For instance, the original SDF framework and lexicon established in the context of military application are not aptly suited for all potential uses of SDF. Nevertheless, the design of any SDF system should attempt to address the following fundamental questions [4, 47]:

- What are the number and type of information sources?
- What architecture should be used?
- How should the individual sensor data be processed to extract the maximum amount of information?
- What algorithms or techniques are appropriate and optimal for a particular application?

- What accuracy can realistically be achieved by a data fusion process?
- How can the fusion process be optimized in a dynamic sense?
- How does the data collection environment affect the processing?
- Under what conditions does SDF improve system operation?

Since the work in this thesis is exploratory and purely computational, not all of these questions are necessarily relevant or require definitive answers at this stage. Namely, the final four questions pertain to the design and deployment of a SDF system, whereas the scope of the research presented in this thesis is limited to the development of SDF techniques specific to the SSIP. These questions may eventually become relevant points of discussion once the SSIP SDF problem progresses beyond computational studies.

We first identify the data and sensor types encountered in this work. Again, while all data were simulated, it is important to discuss how the data would be acquired experimentally to establish a realistic basis for future experimental work. The three types of data involved in the SSIP SDF problem are electrical resistivity, displacement, and strain. The resistivity data is spatially continuous and can be obtained through the use of EIT. Displacement data can be obtained using techniques such as DIC or hardware such as displacement gauges. DIC can capture a spatially displacement field of a surface. However, DIC, and other vision-based methods, is generally unsuited for long term, real-time condition monitoring of structures, so spatial displacement data is not considered in this work. Displacement gauges can provide accurate displacement data at discrete points. Types of displacement gauges include optical, eddy current, ultrasonic, or contact-based sensors. Although displacement gauges are more commonly used in industrial settings, they are also actively being used and researched for structural condition monitoring [83]. Therefore, in this work we make use of discrete displacement data. Strain data can be obtained using strain gauges. Strain gauges are extremely common and are used extensively as an NDE sensor. Certain configurations of strain gauges (i.e. strain rosette) can relay the local in-plane strains at the point on the surface which it is adhered to. Thus, in this work we make use of discrete strain data.

Next, we discuss the SDF architecture selection and the processing of sensor data. To reiterate, the goal of this research is to improve the accuracy and reliability of the SSIP strain and displacement field recovery by fusing resistivity data with some other complementary data in order to enhance MSA. This scenario resembles examples of SDF from NDE literature [52, 54, 55]. Furthermore, since the goals of MSA and NDE are closely related, it is reasonable to adopt the SDF architecture most commonly used for NDE to frame the SSIP SDF problem.

In NDE, a three level hierarchy is traditionally used to classify SDF: data-level, feature-level, and decision-level. Data-level fusion (also called signal/pixel level fusion) involves directly combining raw data before performing further analysis. To be combined, the data must have the same or similar physical meaning or be converted into a common reference value. For instance, signal data cannot be directly combined with visual image data. In feature-level fusion, statistical features are extracted from each data set and combined for further analysis. At the feature-level, data can measure different physical parameters. Finally, decision-level fusion involves combining the independent decision made by each sensor to inform a final assessment.

Fusion of resistivity data with displacement or strain category best fits under data-level fusion. Although resistivity, displacements, and strains are not measured using the same physical units, they are all still physical quantities that can be correlated to the nodes and elements of the same finite element mesh. Additionally, as displacements and strains are explicitly calculated during the SSIP iterative process, this provides opportunities for known displacements and strains to be fused with the resistivity data within the SSIP framework.

With the level of data fusion identified, data registration must be addressed. Data registration is the task of associating data to the correct physical points on specimen being examined. When working with multiple sensors, various types of data are available at different locations on the specimen. Additionally, for sensing techniques providing spatial data, the data resolution are likely to differ because of the different equipment being used. Therefore, all sensor data must be expressed in a common reference frame so that the physical location of data from each sensor is accurate relative to each other, and data of different resolutions must be transformed in order to be compatible for fusion.

For the computational work in this thesis, data registration is relatively straightforward. Computational experiments were performed on a three-dimensional finite element mesh. On this mesh, the SSIP reconstructs the nodal displacements and elemental strains using elemental resistivity data on the same mesh. Given that the same mesh is used throughout the SSIP reconstruction process, the simplest way to ensure proper data registration among sensors is to use the mesh itself as the common reference frame. Therefore, locations of sensors relaying displacement data are selected to coincide with existing mesh nodes. Likewise, locations of sensors relaying strain data are selected to coincide with mesh elements. In other words, specific nodes of the mesh are selected to be displacement sensors (DS), and specific elements of the mesh are selected to be strain sensors (SS).

In the following sections, the techniques behind the fusion of resistivity with displacement and strain data are detailed.

4.2 Fusion of Resistivity and Displacement Data

Fusing discrete displacement data from DS with resistivity data follows a similar approach to enforcing displacement boundary conditions as described in section 3.3. First, all the columns of $\boldsymbol{G}$ associated with DS nodes are replaced with zero column vectors. This is done for two reasons. The first reason is because a column of zeros in a matrix representing a system of linear equations indicates a free variable. In the context of the SSIP, degrees of freedom associated with DS nodes are made free variables. This means that the DS nodes no longer constrain the least squares solution and can be assigned any value. The second reason is to preserve the dimensions of $\boldsymbol{L}$. Recall that $\boldsymbol{L}$ is used for regularization because it enforces that the solution space is smoothly varying. When a column of $\boldsymbol{G}$ is removed, the corresponding rows and columns of $\boldsymbol{L}$ must also be removed to preserve dimensional compatibility. However, the removal of the rows and columns of $\boldsymbol{L}$ disconnects the corresponding nodes from the smooth solution space promoted by $\boldsymbol{L}$. This causes major aberrations in the displacement field reconstruction at and near the DS node.

Second, after $\delta\boldsymbol{d}$ is calculated and $\boldsymbol{d}^n$ is updated, the DS data are inserted into $\boldsymbol{d}^n$, replacing the unconstrained displacement values calculated for the free variables which correspond

to DS nodes. Additional consideration is needed regarding how displacement data are inserted into $\boldsymbol{d}^n$. If the displacement data values being inserted are much larger than majority of values in $\boldsymbol{d}^n$, the SSIP may diverge or arrive at a nonsensical displacement field solution. This is prone to happen since $\boldsymbol{d}^n$ is initialized as the zero vector, and the first few iterations of $\boldsymbol{d}^n$ tend to be small.

The divergence occurs because, for an element containing a DS node, a sharp disparity between the inserted displacement data of DS nodes and SSIP predicted displacements of non-DS nodes results in the calculation of a large elemental strain and, consequently, an outlier model predicted resistivity. This outlier resistivity will cause the SSIP to predict erroneous displacements in the following iteration, an error which compounds and propagates with each iteration. To surmount this problem, displacement data are incorporated using the function defined by equation (4.1).

$$\boldsymbol{d}_{DS}^n = \Phi(n)\boldsymbol{d}_{known} \tag{4.1}$$

In the above, $\boldsymbol{d}_{DS}^n$ is the subset of $\boldsymbol{d}^n$ belonging to DS nodes at the nth iteration, $\boldsymbol{d}_{known}$ is the known displacement data, and $\Phi(n)$ is a ramping function that is a function of n. $\Phi(n)$ is selected such that it is a positive, decimal value that approaches one. The idea is that if the DS data being inserted is incorporated gradually, the discrepancy in displacement values among DS and non-DS nodes can be mitigated enough to prevent the calculation of outlier model predicted resistivity values, thus maintaining the stability of the SSIP. In this work, a piecewise linear ramping function shown in equation (4.2) was selected for simplicity. In words, 10% of the DS data is added with each iteration such that by the tenth iteration, the full displacement data has been incorporated. Here, the slope of the linear ramping function is not necessarily optimal, but it was found that in general, a gentler slope reduced the risk of SSIP divergence. However, this becomes a tradeoff between stability of the SSIP and the total number of iterations required to converge to a solution.

$$\Phi(n) = \begin{cases} \frac{n}{10}, & n < 10 \\ 1, & n \geq 10 \end{cases} \tag{4.2}$$

One can recognize that this SDF method does not resemble the more prevalent data-level SDF methods in NDE such as those involving signal normalization and probabilistic techniques. This is because the goal of the SSIP SDF problem is inherently different from many NDE SDF applications. NDE SDF applications often involve directly combining different sets of raw data to produce a new data set. This new data set is analyzed to achieve more information about a specimen or better discriminate features of interest. In contrast, the SSIP SDF problem does not directly combine resistivity and displacement data to produce a third data set. Rather, the data are fused within the SSIP framework through modifications of the original SSIP formulation to enable a more accurate prediction of the state of a material. While the SSIP SDF problem and the proposed fusion method does not perfectly fit into the definitions established by the NDE SDF architecture, the core principle of SDF is still being exercised.

4.3 Fusion of Resistivity and Strain Data

Fusion of resistivity and strain data is a more challenging problem than fusion of displacement data because this formulation of the SSIP does not directly solve for the strains. The strains are computed from the global displacement vector predicted by the SSIP; therefore, a method similar to the displacement fusion technique presented in the previous section is not possible.

The general approach used for strain data fusion in this thesis is to enforce additional constraints on the displacements. These constraints came in the form of strain-displacement relations. Strain-displacement relations map the displacements of a deformed body to its strain state. For the general, three-dimensional case, assuming small deformations, the strain-displacement relations can be defined by the infinitesimal strain tensor, given earlier in equation (3.8). Here, the six independent strain components derived by expanding equation (3.8) are given below as equation (4.3). To clarify, the incorporation of the infinitesimal strain tensor in the SSIP finite element discretization did not apply strain-displacement relations as a constraint in the way that will be discussed in this section. It did, however, ensure that every displacement field solution found by the SSIP satisfied strain compatibility.

$$
\begin{aligned}
\varepsilon_{11} &= \frac{\partial u_1}{\partial x_1} \\
\varepsilon_{22} &= \frac{\partial u_2}{\partial x_2} \\
\varepsilon_{33} &= \frac{\partial u_3}{\partial x_3} \\
\varepsilon_{12} &= \frac{1}{2}\left(\frac{\partial u_1}{\partial x_2} + \frac{\partial u_2}{\partial x_1}\right) \\
\varepsilon_{13} &= \frac{1}{2}\left(\frac{\partial u_1}{\partial x_3} + \frac{\partial u_3}{\partial x_1}\right) \\
\varepsilon_{23} &= \frac{1}{2}\left(\frac{\partial u_2}{\partial x_3} + \frac{\partial u_3}{\partial x_2}\right)
\end{aligned}
\tag{4.3}
$$

Several methods of incorporating strain-displacement relations were explored resulting in various degrees of success. The first method involved augmenting the SSIP $\boldsymbol{G}$ matrix by concatenating additional rows that represent strain-displacement relations. To accomplish this, first, a global strain-displacement matrix, $\boldsymbol{B}$, was calculated. Since strain gauges provide strain data at a point, $\boldsymbol{B}$ was formulated to map the global nodal displacements to the global nodal strains. While a detailed mathematical formulation of this method is omitted from this section because this strain SDF method was ultimately not selected for use in this thesis, the following is a brief, high-level summary of the formulation and results.

Typically, in finite element discretization, $\boldsymbol{B}$ maps the global nodal displacements to global elemental strains because strains are defined for each mesh element. Therefore, it was necessary for $\boldsymbol{B}$ to be modified so that it instead related nodal displacements to nodal strains. To do so, the L_2 projection was incorporated into $\boldsymbol{B}$. The L_2 projection is a method that can project any arbitrary function defined at the Gauss integration points of the mesh to the mesh nodes [84]. Modification of $\boldsymbol{B}$ with the L_2 projection required the creation of six unique $\boldsymbol{B}$ matrices, denoted as $\boldsymbol{B}^{\varepsilon_{ij}}$, with each mapping the global nodal displacement vector to an independent strain component.

With the six $\boldsymbol{B}^{\varepsilon_{ij}}$ matrices calculated, the rows of $\boldsymbol{B}^{\varepsilon_{ij}}$ corresponding to nodes designated as SS are taken from the appropriate $\boldsymbol{B}^{\varepsilon_{ij}}$ matrix and concatenated to $\boldsymbol{G}$. For instance, if 'Node 1' of the finite element mesh is a SS at which ε_{11} is known, the first row of the $\boldsymbol{B}^{\varepsilon_{11}}$

matrix (the matrix which maps the global nodal displacements to the global nodal ε_{11}) is concatenated to $\boldsymbol{G}$. The known nodal strain data at the SS node is then concatenated to the $\delta\boldsymbol{\rho}$ vector. The SSIP minimization is now defined as equation (4.4), where $\delta\boldsymbol{\beta}$ is the difference between the known nodal strains and the SSIP predicted nodal strains, and $\boldsymbol{B}'$ are the rows concatenated onto $\boldsymbol{G}$. The prime symbol in $\boldsymbol{B}'$ indicates that $\boldsymbol{B}'$ can be a composite of rows from different $\boldsymbol{B}^{\varepsilon_{ij}}$ matrices if multiple strain components are known for at each SS. The number of rows $\boldsymbol{B}'$ has is equal to the number of strain components known at each SS node. For instance, if there are two SS at which three strain components are known, $\boldsymbol{B}'$ would have six rows.

$$\boldsymbol{d}^* = \arg\min_{d} \left\| \begin{bmatrix} \delta\boldsymbol{\rho} \\ \delta\boldsymbol{\beta} \end{bmatrix} - \begin{bmatrix} \boldsymbol{G} \\ \boldsymbol{B}' \end{bmatrix} \delta\boldsymbol{d} \right\|^2 \tag{4.4}$$

While this method was successful in enforcing that the strains at SS nodes equal the known strain data, the reconstructed displacement field tended to greatly under-predict the true displacement field.

The second method involved explicitly treating the SSIP as a constrained least-squares problem. In this method, the original SSIP minimization remains unchanged, but the strain-displacement relations are now treated as linear equality constraints. The rows that were concatenated to $\boldsymbol{G}$ in the previous method are now defined as linear equality constraints. The constrained least squares solution was calculated using the MATLAB function '*lsqlin*'. This method also successfully enforced strains at SS nodes to be equal to the known strain data; however, the displacement magnitude tended to be over-predicted. For a more detailed treatment of the mathematical formulation and results of these two methods, the reader is referred to the appendix.

The third and most successful method used to fuse strain and resistivity data involved adapting and incorporating a technique known as the inverse finite element method (iFEM) into the SSIP. Developed by Tessler et al. [85–87], iFEM is a computational method which aims to reconstruct the displacement field of a finite element discretized structure from a set of discrete strain measurements on the structure. iFEM is an inverse problem and is solved by minimizing a least squares functional. Since iFEM was originally developed for plate and

shell elements based on Mindlin plate theory, the least squares functional takes the form given in equation (4.5).

$$\boldsymbol{\Phi}(u) = \boldsymbol{W}_{\mathrm{e}}\|\mathbf{e}(\boldsymbol{u}) - \mathbf{e}^{\varepsilon}\|^2 + \boldsymbol{W}_{k}\|\boldsymbol{k}(\boldsymbol{u}) - \boldsymbol{k}^{\varepsilon}\|^2 + \boldsymbol{W}_{g}\|\boldsymbol{g}(\boldsymbol{u}) - \boldsymbol{g}^{\varepsilon}\|^2 \tag{4.5}$$

In the equation above, $\mathbf{e}$, $\boldsymbol{k}$, and $\boldsymbol{g}$ represent the in-plane membrane strains, bending curvatures, and transverse shear strains, respectively. Note that in iFEM, the strains are treated as elemental properties, meaning a strain state was defined for each element in the finite element mesh. Furthermore, u are the nodal degrees of freedom, $\boldsymbol{W}$ are scalar weight coefficients, and terms with superscript ε indicate the set of experimentally measured strains. Each squared norm term contains the difference between the strains calculated via Mindlin plate theory strain-displacement relations as a function of $\boldsymbol{u}$ and the experimentally measured strains. Minimization of this functional with respect to $\boldsymbol{u}$ theoretically recovers the displacement field that produced the measured strains. In other words, if the difference between the model predicted strains and the experimentally measured strains is minimized, the displacement field can be reconstructed. This functional is then defined for each element in a finite element mesh and subsequently assembled into a global functional in typical finite element method fashion.

One key limitation of this method is the availability of measured strain data. Obviously, strain data will not be available at every point within a structure, and, at points with sensors, not all strain components can be measured. For instance, strain sensor networks are often sparse, and transverse shears cannot be measured using an in-plane strain gauge. Therefore, in the original formulation, mesh elements that did not possess experimental strain data had their experimentally measured strain vectors, e^{ε}, k^{ε}, or g^{ε}, set equal to zero. This hindered the overall accuracy of the recovered displacement field because this effectively enforced that certain strains equal zero when in actuality they were non-zero. To minimize this effect, weight coefficients, $\boldsymbol{W}$, were introduced such that mesh elements with measured strain data were given a significantly larger weight, usually by a factor between 1×10^3 to 1×10^6, than elements without experimental data. This amplifies the contribution of elements with strain data to the solution relative to elements without strain data.

Later refinement of iFEM introduced methods to pre-extrapolate the strains for mesh elements without strain data. In other words, the strains for elements without strain data can be estimated using statistical [88] or physics-based [89] methods, which can provide improved accuracy of the recovered displacement field.

From the brief explanation of iFEM above, it can be recognized that the objective and mathematical formulation of iFEM and the SSIP are similar, thus motivating their synergistic combination. The SSIP SDF problem seeks a method to fuse strain data with resistivity data in order to more accurately recover the displacement field. iFEM is a method which recovers a displacement field directly from discrete strain data, but ideally requires a method to pre-extrapolate strains for elements without strain data. Since SSIP predicts a strain tensor for each mesh element during its iterative process, the SSIP can be used pre-extrapolate strains. Moreover, the iFEM mathematical formulation can be readily incorporated into the SSIP to allow for SDF of strain data. The following details the adaptation and incorporation of iFEM into the SSIP for the SDF of resistivity and strain data.

In this thesis, the finite element meshes used consist of hexahedral elements that are subject to general deformations. Thus, the least squares functional in equation (4.5) is re-expressed as equation (4.6) for the eth hexahedral element. For general deformations, the bending curvature and transverse shear terms from equation (4.5) are dropped, and u, which included nodal displacements and rotations, is changed to d to express nodal displacements only. In the equation below, $d^A_{\mathrm{e,i}}$ are the nodal displacements, $\varepsilon_{\mathrm{e}}(d^A_{\mathrm{e,i}})$ are the strains calculated from strain-displacement relations, $\bar{\varepsilon}_{\mathrm{e}}$ are the known strain data, and W_{e} is a diagonal matrix containing the weight coefficients of each strain component for the eth element. Equation (4.7) is the vector of strains ε represents.

$$\Phi_{\mathrm{e}}(d^A_{\mathrm{e,i}}) = W_{\mathrm{e}}\|\varepsilon_{\mathrm{e}}(d^A_{\mathrm{e,i}}) - \bar{\varepsilon}_{\mathrm{e}}\|^2 = W_{\mathrm{e}}\int_V [\varepsilon_{\mathrm{e}}(d^A_{\mathrm{e,i}}) - \bar{\varepsilon}_{\mathrm{e}}]^2 dV \tag{4.6}$$

$$\varepsilon = \begin{bmatrix} \varepsilon_{11} & \varepsilon_{22} & \varepsilon_{33} & \varepsilon_{12} & \varepsilon_{13} & \varepsilon_{23} \end{bmatrix}^T \tag{4.7}$$

Next, we express $\varepsilon_{\mathrm{e}}(d^A_{\mathrm{e,i}})$ in terms of linear algebra as the product of the element nodal displacements and the elemental B_{e} matrix as shown in equation (4.8). The elemental B_{e}

matrix, which maps the element nodal displacements to the six independent element strain components as defined in equation (4.7), is shown in equation (4.9). To clarify, the B_e strain-displacement matrix in this context mapped nodal displacements to elemental strains, unlike the strain-displacement matrix discussed earlier in the prior strain SDF methods explored.

$$\varepsilon_e(d^A_{e,i}) = B_e d^A_{e,i} \tag{4.8}$$

$$B_e = \begin{bmatrix} \frac{\partial N^1}{\partial x_1} & 0 & 0 & \frac{\partial N^2}{\partial x_1} & 0 & 0 & \cdots & \frac{\partial N^8}{\partial x_1} & 0 & 0 \\ 0 & \frac{\partial N^1}{\partial x_2} & 0 & 0 & \frac{\partial N^2}{\partial x_2} & 0 & \cdots & 0 & \frac{\partial N^8}{\partial x_1} & 0 \\ 0 & 0 & \frac{\partial N^1}{\partial x_3} & 0 & 0 & \frac{\partial N^2}{\partial x_3} & \cdots & 0 & 0 & \frac{\partial N^8}{\partial x_3} \\ \frac{1}{2}\frac{\partial N^1}{\partial x_2} & \frac{1}{2}\frac{\partial N^1}{\partial x_1} & 0 & \frac{1}{2}\frac{\partial N^2}{\partial x_2} & \frac{1}{2}\frac{\partial N^2}{\partial x_1} & 0 & \cdots & \frac{1}{2}\frac{\partial N^8}{\partial x_2} & \frac{1}{2}\frac{\partial N^8}{\partial x_1} & 0 \\ \frac{1}{2}\frac{\partial N^1}{\partial x_3} & 0 & \frac{1}{2}\frac{\partial N^1}{\partial x_1} & \frac{1}{2}\frac{\partial N^2}{\partial x_3} & 0 & \frac{1}{2}\frac{\partial N^2}{\partial x_1} & \cdots & \frac{1}{2}\frac{\partial N^8}{\partial x_3} & 0 & \frac{1}{2}\frac{\partial N^8}{\partial x_1} \\ 0 & \frac{1}{2}\frac{\partial N^1}{\partial x_3} & \frac{1}{2}\frac{\partial N^1}{\partial x_2} & 0 & \frac{1}{2}\frac{\partial N^2}{\partial x_3} & \frac{1}{2}\frac{\partial N^2}{\partial x_2} & \cdots & 0 & \frac{1}{2}\frac{\partial N^8}{\partial x_3} & \frac{1}{2}\frac{\partial N^8}{\partial x_2} \end{bmatrix} \tag{4.9}$$

Plugging equation (4.8) into equation (4.6), we arrive at the first term of equation (4.10). Here, the superscript A and subscript i are omitted for notational clarity. By expanding the integrand and consolidating terms, we obtain the final term of equation (4.10). Below, K_e is the elemental iFEM stiffness matrix, and f_e is the elemental iFEM forcing vector.

$$\begin{aligned} \Phi_e(d^A_{e,i}) &= W_e \int_V [B_e d_e - \bar{\varepsilon}_e]^2 dV \\ &= \int_V (d_e^T B_e^T W_e B_e d_e - 2 d_e^T B_e^T W_e \bar{\varepsilon}_e + \bar{\varepsilon}_e^T W_e \bar{\varepsilon}_e) dV \\ &= d_e^T \left[\int_V B_e^T W_e B_e dV \right] d_e - 2 d_e^T \left[\int_V B_e^T W_e \bar{\varepsilon}_e dV \right] + \int_V \bar{\varepsilon}_e^T W_e \bar{\varepsilon}_e dV \\ &= d_e^T K_e d_e - 2 d_e^T f_e + c \end{aligned} \tag{4.10}$$

To minimize equation (4.10), the variation of Φ_e is taken with respect to $d^A_{e,i}$ and set equal to zero, as shown in equation (4.11).

$$\delta \Phi_e = K_e d^A_{e,i} - f_e = 0 \tag{4.11}$$

The K_e matrix and f_e vectors of each element are then assembled into a global $\boldsymbol{K}$ matrix and $\boldsymbol{F}$ vector encompassing the entire finite element mesh, resulting in equation (4.12). $\boldsymbol{K}$ is a square, symmetric matrix with the number of rows and columns equal to the total number of displacement degrees of freedom, and $\boldsymbol{F}$ is a vector of matching length.

$$\boldsymbol{K}\boldsymbol{d} - \boldsymbol{F} = 0 \tag{4.12}$$

At this point, iFEM proceeds by applying displacement boundary conditions just as in a normal finite element routine, and then the displacement field is reconstructed by computing $\boldsymbol{d} = \boldsymbol{K}^{-1}\boldsymbol{F}$. However, the goal is to incorporate equation (4.12) into the SSIP. We therefore proceed by replacing $\boldsymbol{d}$ in equation (4.12) with $\delta\boldsymbol{d}$, where $\delta\boldsymbol{d}$ is the difference between the true displacement field and the model predicted displacement field, to match the $\delta\boldsymbol{d}$ being solved for by the SSIP in equation (3.18). Additionally, $\bar{\varepsilon}_e$ in f_e is converted to $\delta\bar{\varepsilon}_e$, defined as the difference between the measured strain data at SS and the model predicted strains. This conversion yields equation (4.13), which is then concatenated directly to the SSIP minimization in equation (3.17), resulting in equation (4.14).

It is important to note that regularization is no longer required to solve for $\delta\boldsymbol{d}$ in equation (4.14), so equation 3.18 is not used here. Instead, the MATLAB function *lsqlin* is used to solve equation (4.14) for $\delta\boldsymbol{d}$ in the least squares sense. Otherwise, the modified SSIP proceeds normally—$\delta\boldsymbol{d}$ is calculated, $\boldsymbol{d}^n$ is updated via $\boldsymbol{d}^{n+1} = \boldsymbol{d}^n + \delta\boldsymbol{d}$, and the new $\boldsymbol{d}^n$ is used to calculate the next estimates of ε_{ij}^n, $\partial f(\varepsilon_{ij}^n)$, and $\partial f(\varepsilon_{ij}^n)/\partial\varepsilon_{ij}^n$ so that the next iteration can proceed.

$$\boldsymbol{K}\delta\boldsymbol{d} - \delta\boldsymbol{F} = 0 \tag{4.13}$$

$$\boldsymbol{d}^* = \arg\min_d \left\| \begin{bmatrix} \delta\boldsymbol{\rho} \\ \delta\boldsymbol{F} \end{bmatrix} - \begin{bmatrix} \boldsymbol{G} \\ \boldsymbol{K} \end{bmatrix} \delta\boldsymbol{d} \right\|^2 \tag{4.14}$$

Now, strain pre-extrapolation is addressed. Prior to each iteration of the modified SSIP, a $\delta\boldsymbol{d}$ is calculated using the unmodified SSIP, hereon denoted as $\delta\boldsymbol{d}^X$. $\delta\boldsymbol{d}^X$ then is used to calculate a global strain increment $\delta\boldsymbol{\varepsilon}_{ij}^X$, which is a move direction in terms of elemental

strain tensors that satisfies the SSIP minimization. For mesh elements without strain data, $\delta\bar{\varepsilon}_{\mathrm{e}} = \delta\varepsilon^{X}_{\mathrm{e,ij}}$. For mesh elements with strain data, $\delta\bar{\varepsilon}_{\mathrm{e}} = \bar{\varepsilon}_{\mathrm{e}} - \varepsilon^{n}_{\mathrm{e,ij}}$. Note that $\delta\bar{\varepsilon}_{\mathrm{e}}$ is a $[6 \times 1]$ vector while $\delta\varepsilon^{X}_{\mathrm{e,ij}}$ and $\delta\varepsilon^{n}_{\mathrm{e,ij}}$ are second order tensors. By equating the vector to the tensor, the intent is to convey that the strain components of the vector are set equal to the corresponding strain components in the tensor.

This strain SDF method has a few advantages over the prior two methods discussed. The first is that the strain-displacement relations for the entire finite element mesh are incorporated instead of just a few rows associated with SS. Including the global strain-displacement relations enforces a mesh-wide nodal connectivity based on mechanics, which may help guide the SSIP displacement field recovery closer to the true displacement field. Second, this method is less computationally expensive because there is no need to project element strains to the nodes or formulate the modified $\boldsymbol{B}$.

5. COMPUTATIONAL EXPERIMENTS

This chapter details the objectives, design, and procedures of the computational experiments performed to achieve the research goals.

5.1 Computational Study Objectives

As discussed in previous chapters, the displacement field solution predicted by the SSIP is highly sensitive to noise and outliers in the resistivity data, which limits the accuracy and reliability of the recovered displacement field. By incorporating additional data via SDF, we endeavor to improve upon these shortcomings. To this end, the computational experiments performed should address the following three objectives:

1. Determine the number of sensors required to improve the accuracy of the SSIP recovered displacement field to a sufficient degree.

2. Demonstrate how SDF affects the reliability of the SSIP when resistivity data noise is increased.

3. Demonstrate how SDF affects the reliability of the SSIP when there are outlier resistivity data.

A separate computational experiment was performed for each objective. Furthermore, each experiment was performed twice, once for the fusion of displacement and resistivity data, and second for the fusion of strain and resistivity data. The details regarding the experiments are explained in section 5.3.

5.2 Geometries and Load Cases

Since computational and experimental work employing the SSIP has thus far been limited to simple shapes, the geometries selected for this work represent practical structural components. It is important to preface the following discussion by emphasizing that the geometries and load cases presented are representations and are not intended to be rigorous models of real components or their operational load cases. For instance, any dimensions

or load magnitudes are not based on or derived from actual part drawings or engineering analysis. The sole intent is to demonstrate that the SSIP can be applied to more complex shapes and loads.

Three geometries were selected for this work and are depicted in figure 5.1. The shapes are simplified representations of a T-shaped mounting bracket, a section of an aircraft wing spar, and the skin of an aircraft wing. For clarity, they will be hereon referred to as the mounting bracket, wing spar, and airfoil. The dimensions displayed are only relevant in establishing the proportions of each component. These shapes were selected because they are all parts of an aircraft that carry critical loads and would be of key interest for condition-monitoring and MSA.

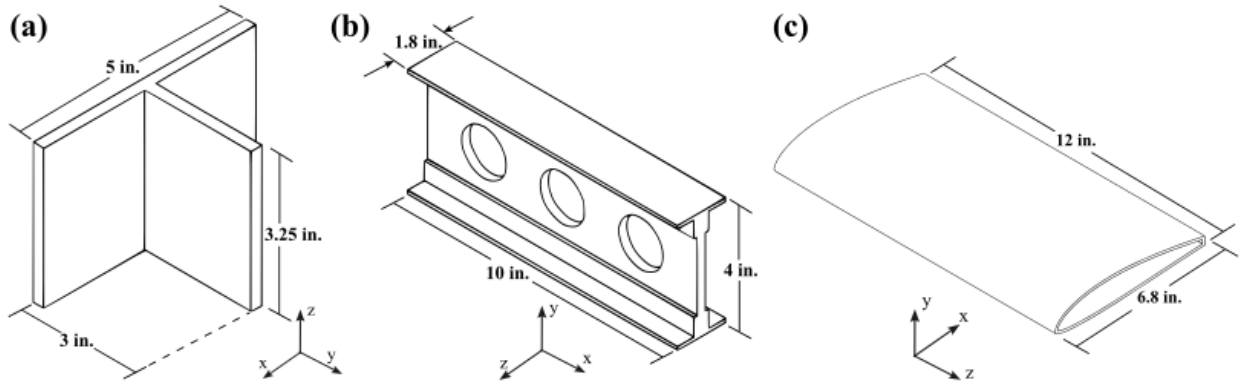

Figure 5.1. Isometric views of the geometries modeled for the computational experiments: (a) mounting bracket, (b) wing spar, (c) airfoil.

The load case and resulting deformation for each geometry are illustrated in figure 5.2. The load cases roughly simulate an operational load each component could experience. The magnitude of the loads were selected such that no axial strains exceeded $\pm 6.0 \times 10^{-3}$ and no shear strains exceeded $\pm 1.5 \times 10^{-2}$. These bounds were established because the piezoresistivity model used is only guaranteed to be accurate within those ranges of strains [80]. What follows is a detailed description of each load case and the real world operational load each represents.

The mounting bracket is essentially a fixed-free cantilever, with the rear face of the flange clamped and the web free. In practical application, the rear face would be bolted to a rigid

surface, and the web serves as a mounting plate for a load bearing member to attach to. Force along this member would be transferred from the member to the rigid surface through the mounting bracket via shear. Now, consider a member attached to the mounting bracket web at an angle and subject to tension. To simulate this load on the mounting bracket, a 155 kPa uniform shear stress is applied to both sides of the web directed at 45° counter-clockwise from the $+y$-axis.

The wing spar is also virtually a fixed-free cantilever. The fixed end would be the root of the wing spar connected to the aircraft fuselage, and the free end would be the wing tip. During maneuvering flight, the aerodynamic loads on an aircraft wing can induce twist—a rotation of the wing about its longitudinal axis. To simulate this for the wing spar, the surfaces of the spar caps are subject to a 10 kPa uniform shear stress in opposite directions along the z-axis.

The airfoil represents the skin of a straight wing with an SD7062 airfoil. The shape was modeled to be open and hollow with a finite shell thickness of 0.1 in. The trailing edge of the shape was truncated at the 80% chord position. Both of these geometric parameters were chosen to avoid the potential meshing complications an extremely thin shell and sharp trailing edge would pose for hexahedral elements. The load on the airfoil roughly simulates the net pressure distribution a wing would experience at 5° angle of attack and 45 m/s airspeed at sea-level. The airfoil was given fixed-fixed end boundary conditions. To arrive at the pressure distribution used in this work, the software *XFOIL* [90] was first used to calculate the pressure coefficient plot for the SD7062 airfoil at 5° angle of attack, assuming viscous flow. The pressure coefficients were then converted into a static pressure value using equation (5.1), where p is the static pressure at a point on the wing surface, C_p is the pressure coefficient at the same point, ρ is the density of air (in this context only), V_∞ is the freestream velocity, and p_∞ is the freestream pressure. Next, it was assumed that the pressure inside the airfoil shape is equal to p_∞; therefore, p_∞ is subtracted from p to arrive at the net pressure distribution. Finally, this two-dimensional net pressure distribution was extended along the entire span of the airfoil shape. It is acknowledged that the final, three-dimensional net pressure distribution is a simplification and neglects the effects of a finite wing.

$$p = \frac{1}{2}\rho V_\infty^2 C_p + p_\infty \tag{5.1}$$

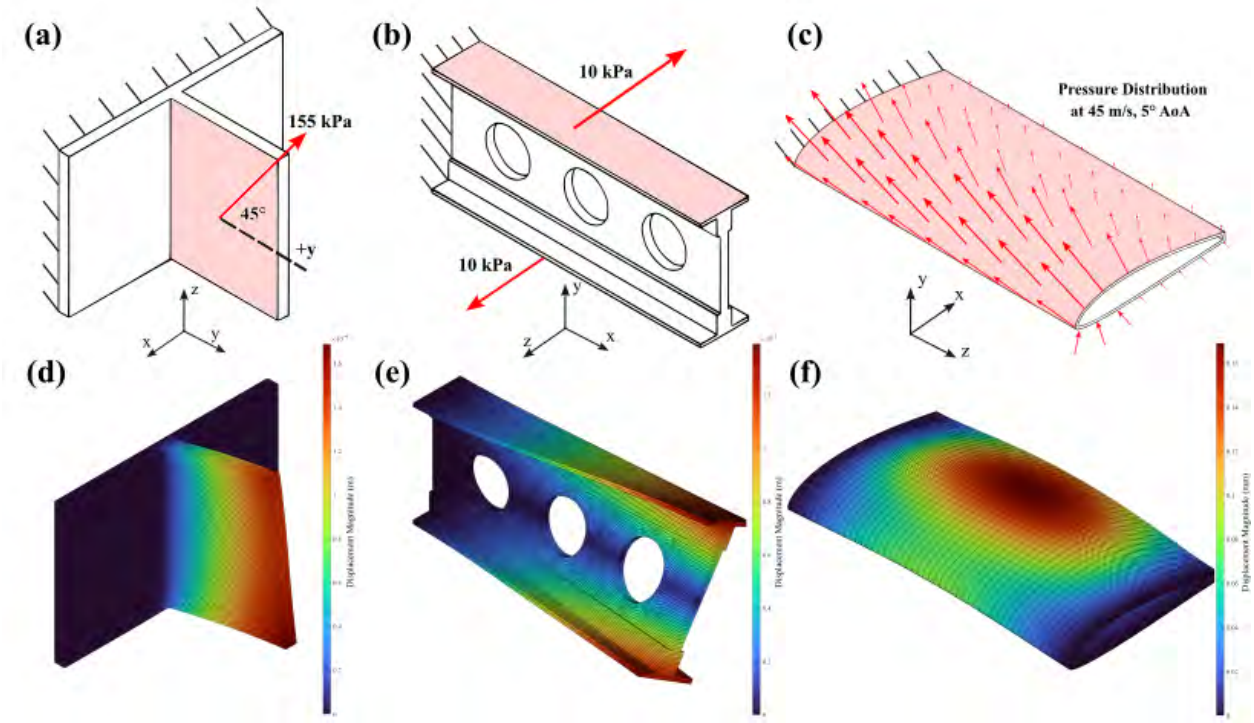

Figure 5.2. Top row: illustration of the load case for the (a) mounting bracket, (b) wing spar, and (c) airfoil. Bottom row: scaled deformation resulting from the load calculated from finite element analysis.

To prepare the geometries for the computational experiments, each was discretized into two finite element meshes, one coarse mesh and one fine mesh, using the meshing software *Trelis*. The fine mesh was derived from the coarse mesh via a simple refinement process where each hex element of the coarse mesh was split into eight smaller hex elements. The meshes are displayed in figure 5.3, and the mesh parameters are given in table 5.1.

Next, nodes and elements on the surface of each coarse mesh were selected to be DS and SS, respectively. The DS and SS were selected to be at the same locations to allow for comparison between DS and SS results. Furthermore, the sensor locations were selected to be as uniformly spaced as possible. While sensor location is an extremely important consideration in NDE when instrumenting a component in order to maximize efficiency

and usefulness of the data obtained, optimizing sensor location is outside the scope of this research. Additionally, since we are attempting to recover the global displacement field, it is logical to place sensors uniformly throughout the shape.

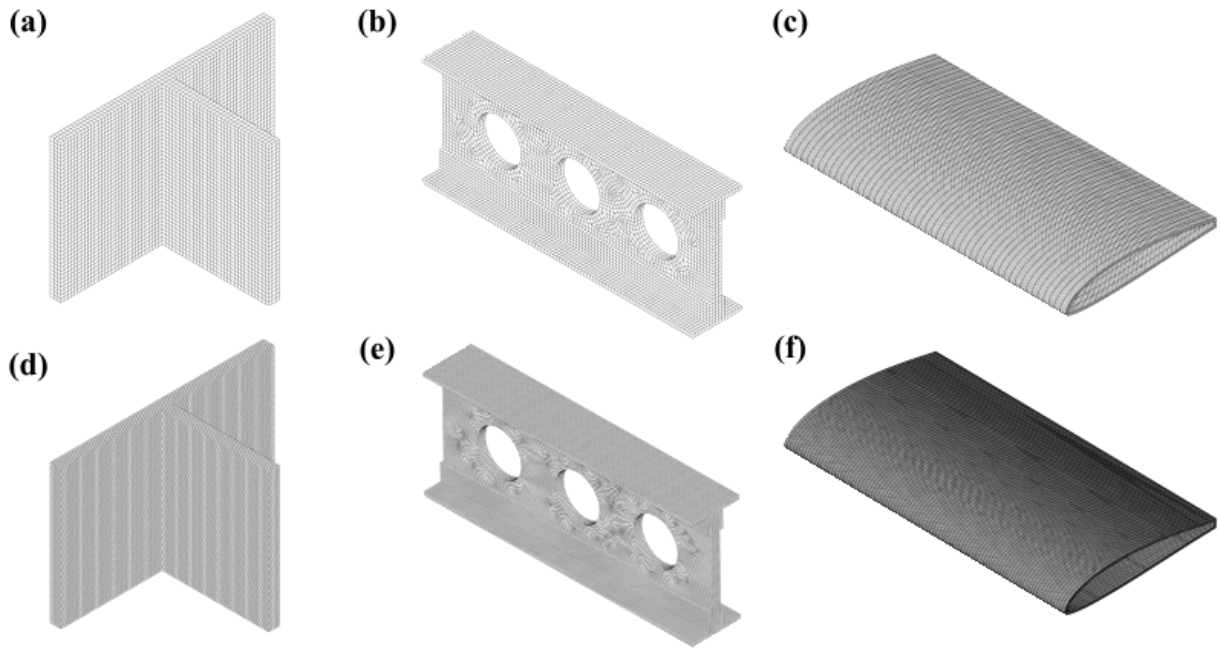

Figure 5.3. Coarse meshes (a)-(c) and fine meshes (d)-(f) generated for the mounting bracket, wing spar, and airfoil.

A total of 50, 78, and 85 potential sensor locations were selected for the mounting bracket, wing spar, and airfoil, respectively, shown in figure 5.4. For the mounting bracket and wing spar, the sensor locations were selected in pairs with half of the sensors seen in figure 5.4, and the others mirrored about the shapes' planes of symmetry. For the airfoil, sensors were placed on the top and bottom of the shape at each 10% chord station at the root, 25%, 50%, 75%, and 100% span position. To clarify, not all the sensor locations shown in figure 5.4 were necessarily used in the computational experiments. Instead, they represent the maximum number of sensors to be considered for each shape. The justification for an upper limit on the number of sensors is that while it is simple in a computational experiment to include as many sensors as necessary to ensure the SSIP recovers the correct displacement field, it becomes impractical to use an excessive number of sensors in experimental application due to cost and complexity constraints.

Table 5.1. Total number of nodes and elements for each mesh.

	Coarse Mesh		Fine Mesh	
Geometry	Nodes	Elements	Nodes	Elements
Mounting Bracket	15,960	11,562	109,809	92,496
Wing Spar	18,680	12,662	124,942	101,296
Airfoil	40,698	26,650	268,862	213,200

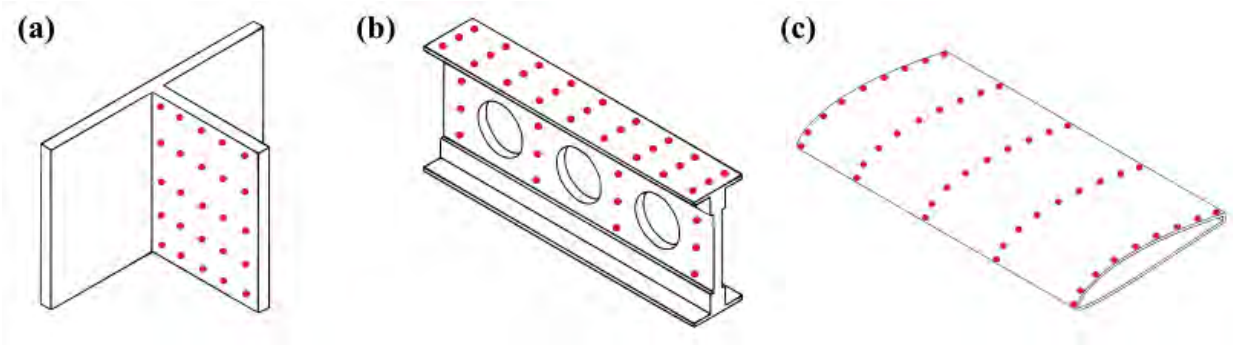

Figure 5.4. All potential sensor locations, indicated by red circles, for the (a) mounting bracket, (b) wing spar, and (c) airfoil.

5.3 Computational Experiment Procedure

The computational experiment procedure is succinctly illustrated by figure 5.5. First, the exact displacement field solution was calculated using standard finite element analysis on the fine mesh and was used to calculate a strain tensor for each element. The exact displacement field solution for each shape is shown in figure 5.6. Second, simulated resistivity data were generated for the fine mesh by plugging each elemental strain tensor into equation (3.1). Next, the fine mesh simulated resistivity data were averaged onto the coarse mesh. Next, to better represent experimental data, Gaussian white noise was added to the coarse mesh data. Figure 5.7 shows the averaged resistivity data at 75 dB SNR. Finally, the SSIP was performed using the coarse mesh resistivity data to attempt to recover the displacement field on the coarse mesh. A reconstruction is considered successful if the recovered displacement field on the coarse mesh closely matches the exact displacement field on the fine mesh.

The reason two different meshes were used was to prevent 'inverse crime' [81]. To explain in the context of the SSIP, if the SSIP reconstructs the displacement field using the same

mesh that the resistivity distribution is simulated on, it is *possible* (even if unlikely) that the recovered displacement field perfectly or very closely matches the exact displacement field. While one might be tempted to accept this result as a success, this however constitutes inverse crime. Some ways to avoid inverse crime as identified in [81] are to perform a reconstruction on a different mesh than the one used to simulate data and to add noise to the simulated data.

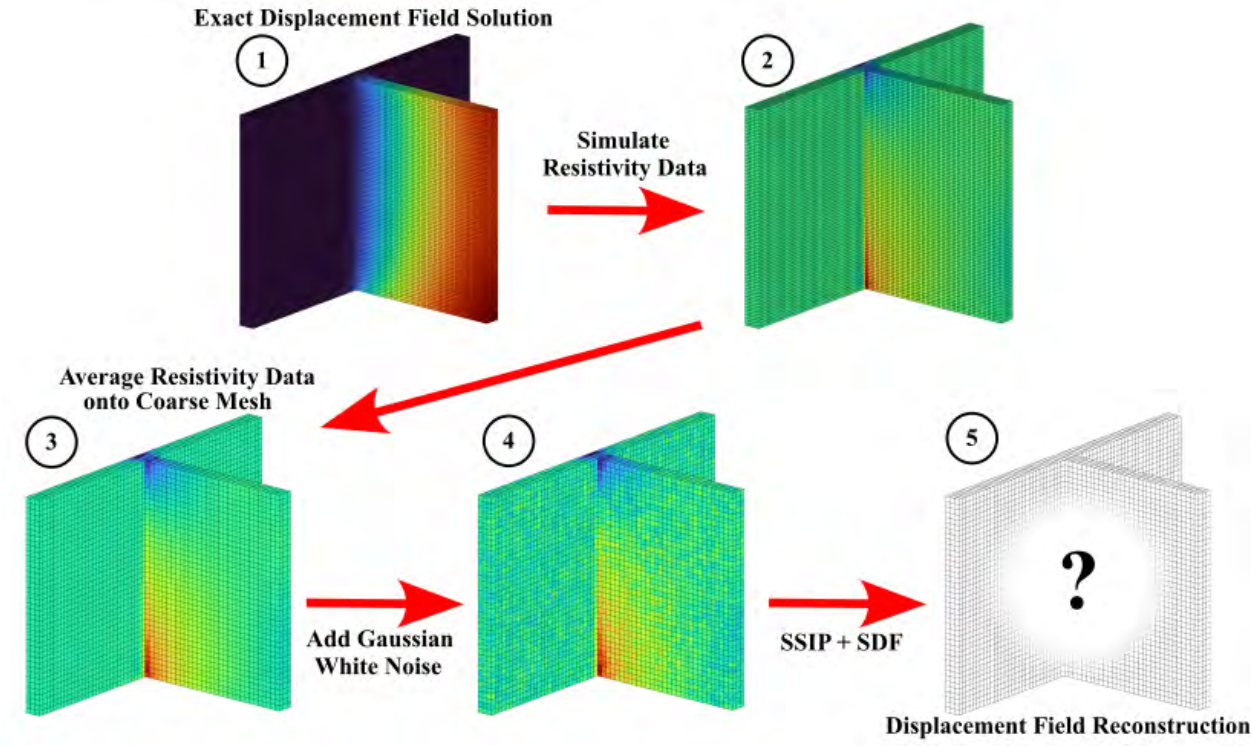

Figure 5.5. Flow chart illustrating the computational experiment workflow.

To simulate the mechanical deformation and resistivity data, all of the shapes were assumed to possess the mechanical and piezoresistive properties of 1 wt.% CNF/epoxy. While CNF/epoxy is obviously not the ideal material to manufacture any of the components, it was selected because an experimentally validated piezoresistivity model for the material already exists [80]. For simplicity, it was also assumed that the undeformed material would have a uniform resistivity distribution of 75,000 $\Omega \cdot$ m, a value derived from experimental character-

ization of the material [91]. The elastic properties and piezoresistivity model constants used are summarized in table 5.2.

Table 5.2. Elastic properties and piezoresistivity model constants used to define 1 wt.% CNF/epoxy.

Mechanical Properties	
E	2.711 GPa
ν	0.351
Piezoresistivity Constants	
κ	4.10 $\times 10^6$
Π_1	-1.50 $\times 10^8$
Π_2	5.15 $\times 10^5$
ρ_0	75,000 $\Omega \cdot$ m

In addition to the relative residual in equation (3.20), two metrics were plotted for each iteration of the SSIP to evaluate the SSIP convergence behavior: the resistivity error and the normalized displacement error, defined by equations (5.2) and (5.3), respectively. In the equations below, ϵ_ρ^n is the resistivity error, $[\boldsymbol{f}(\varepsilon_{ij})]^n$ is the model predicted resistivity distribution, ϵ_d^n is the resistivity error, $\boldsymbol{d}_{exact}$ is the exact displacement field solution, and superscript n is the iteration number. The resistivity error measures how closely the model predicted resistivity distribution matches the simulated resistivity data, and the displacement error measures how closely the displacement field estimate matches the exact displacement solution. Both error metrics are expected to converge to zero if the minimization in equation (3.17) is being satisfied and the SSIP predicted displacement field approaches the true displacement field.

It is important to note that in experimental application, the displacement error is a metric that cannot be tracked because the true displacement field is unknown. The only information a user would have available is the experimentally observed resistivity distribution and thus the resistivity error. Nevertheless, the displacement error is presented here as a useful tool to show if SDF improves convergence to the correct displacement field.

$$\epsilon_\rho^n = \|\boldsymbol{\rho} - [\boldsymbol{f}(\varepsilon_{ij})]^n\|^2 \tag{5.2}$$

$$\epsilon_d^n = \left\| \frac{\boldsymbol{d}_{exact}}{\|\boldsymbol{d}_{exact}\|^2} - \frac{\boldsymbol{d}^n}{\|\boldsymbol{d}_{exact}\|^2} \right\|^2 \tag{5.3}$$

Three computational experiments, hereon called Experiment 1, Experiment 2, and Experiment 3, were performed to individually address each of the three objectives identified in section 5.1. Again, each experiment was performed separately for the fusion of displacement data from DS and the fusion of strain data from SS.

Experiment 1 explored the first objective. Using 75 dB SNR resistivity data, two sensors on exact opposite sides of each shape were activated at a time until the reconstructed displacement field was deemed accurate to the exact solution. The sensors were added in a pattern that maintained uniform sensor spacing as closely as possible. Generally, it is difficult to objectively evaluate the accuracy of a recovered displacement field without prior knowledge of the exact solution. However, although in this case the exact solution was available and ϵ_d quantified the accuracy of the recovered displacement field compared to the exact solution, assigning a specific value for ϵ_d that deems the recovered displacement field as 'sufficiently accurate' is markedly arbitrary. Therefore, the number of sensors required to sufficiently improve the SSIP was determined qualitatively using a plot of ϵ_d against number of sensors and visual inspection of the recovered displacement fields.

Experiment 2 addressed the second objective. The SSIP was performed on resistivity data with 75, 50, 40, and 30 dB SNR while being supplemented with additional sensor data. The sensor configuration determined in Experiment 1 that brought the the SSIP recovered displacement field sufficiently close to the exact solution was used.

Experiment 3 investigated the third objective. For each shape, eight clusters of elements were randomly selected from the coarse mesh to contain outlier resistivity data. A cluster of elements consists of a selected element and all elements adjacent to it. Half of the clusters were assigned a resistivity value of 105,000 $\Omega \cdot$ m, and the remaining outlier elements were assigned 45,000 $\Omega \cdot$ m. Figure 5.8 shows the resistivity data with the outlier clusters. These outlier values were selected to be $\pm$30,000 $\Omega \cdot$ m of ρ_0, which is outside the range where the piezoresistivity model is accurate. These outlier data were applied to the resistivity data with 75 dB SNR. The displacement field was recovered using two sensor configurations, the

first being the same sensor configuration used in Experiment 2, and the second being a configuration with an increased number of sensors over the previous.

Both the displacement and strain sensor data came from the elasticity solution on the fine mesh. Because the DS was not based on a real NDE sensor, it was decided that, in this work, all three displacement components were to be known at each DS simply as a proof of concept demonstrating how SDF could enhance the SSIP. However, since strain gauges are a commonly used NDE sensor, a more realistic approach was taken for SS. Each SS relayed the in-plane principal and shear strains relative to the surface which the SS was placed.

The choice of the scalar regularization parameter, α, was driven by multiple factors. The primary purpose of α is to balance the tradeoff between fitting the data and the strength of regularization. However, to avoid having to tune α for every sensor configuration for each shape, a single α was selected for each shape. This also allows for better comparison of results among different sensor configurations—any difference in reconstruction quality can be entirely attributed to SDF and not a change in α. The selection process entailed sweeping through a range of potential α values between 1 and $1{\times}10^{10}$ and performing a reconstruction at each power of ten. During this process, it was found that the displacement reconstruction itself was relatively insensitive to α for a band of values generally between $1{\times}10^{3}$ and $1{\times}10^{8}$, the range varying depending on the geometry and the magnitude of the load. Within this range, the smallest α which stabilized any oscillatory behavior in the residual and relative residual convergence was selected. Thus, α was selected to be 1×10^{6} for the mounting bracket and airfoil and 1×10^{8} for the wing spar.

Finally, in this work, the convergence criteria was $\epsilon = 10^{-6}$ and the maximum iteration limit was set to 20.

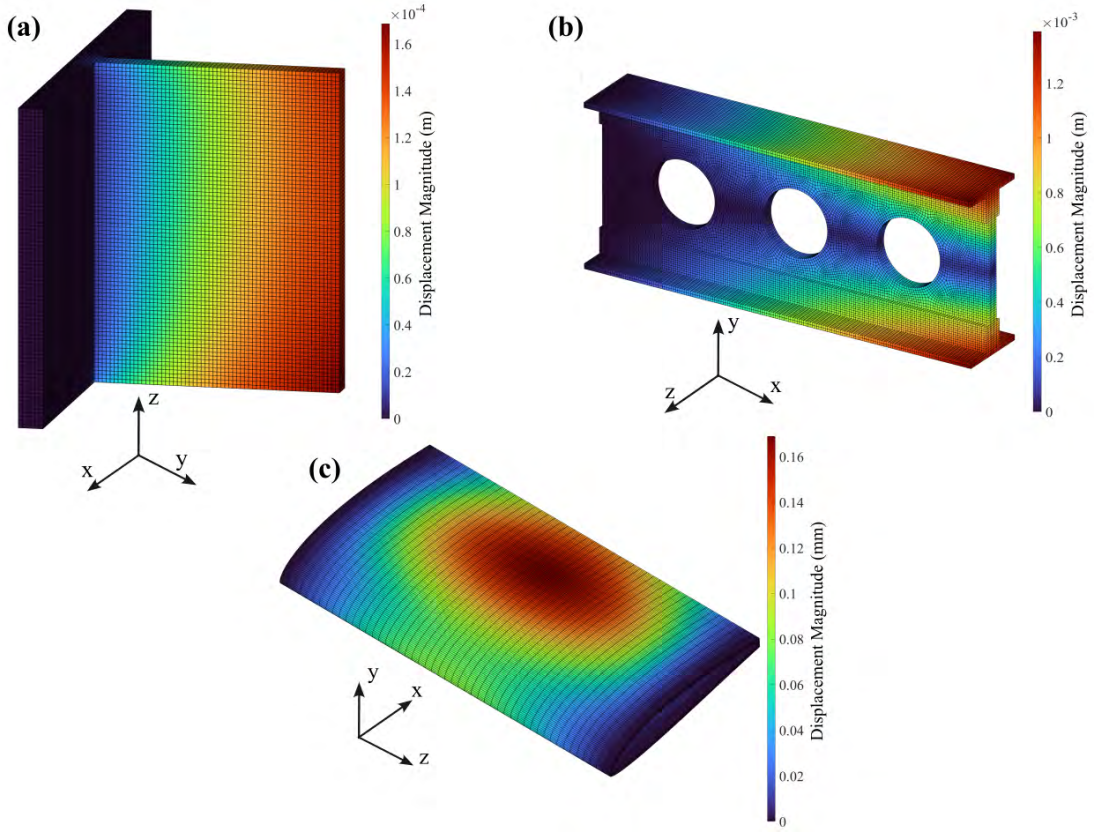

Figure 5.6. Exact displacement field solution for (a) mounting bracket, (b) wing spar, and (c) airfoil simulated using finite element analysis.

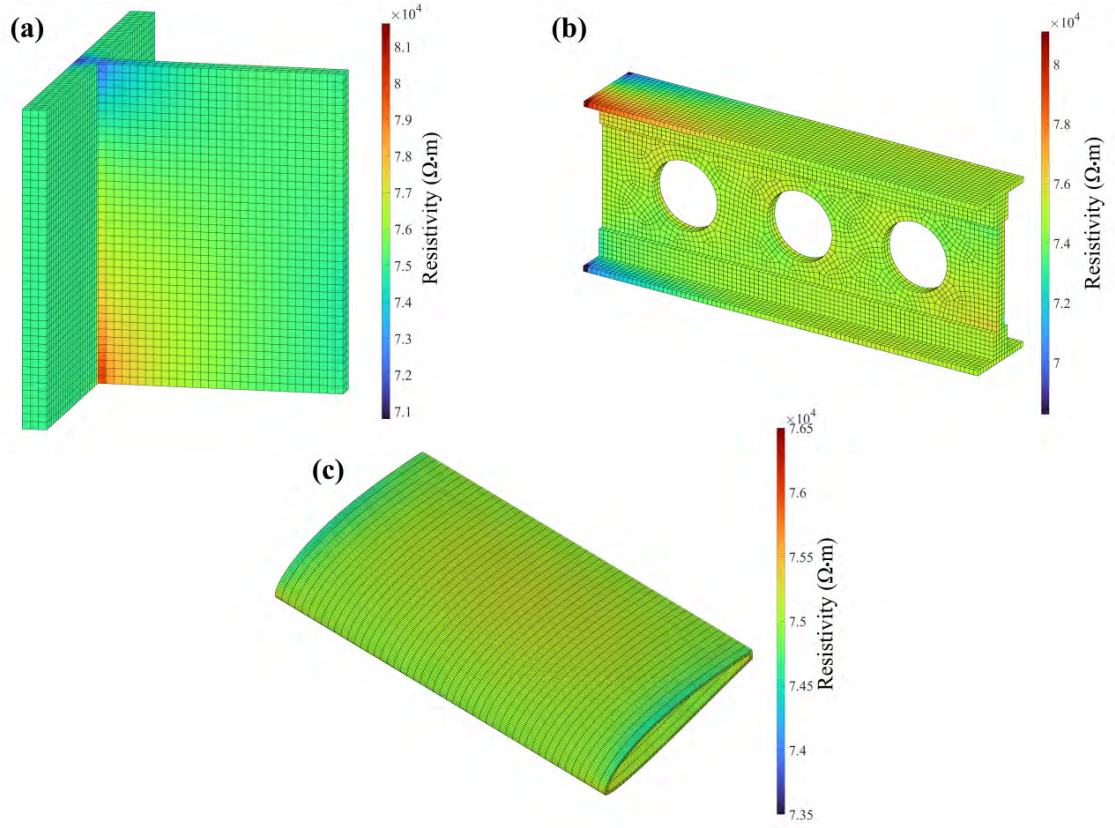

Figure 5.7. Resistivity data averaged on coarse mesh with 75 dB SNR for the (a) mounting bracket, (b) wing spar, and (c) airfoil.

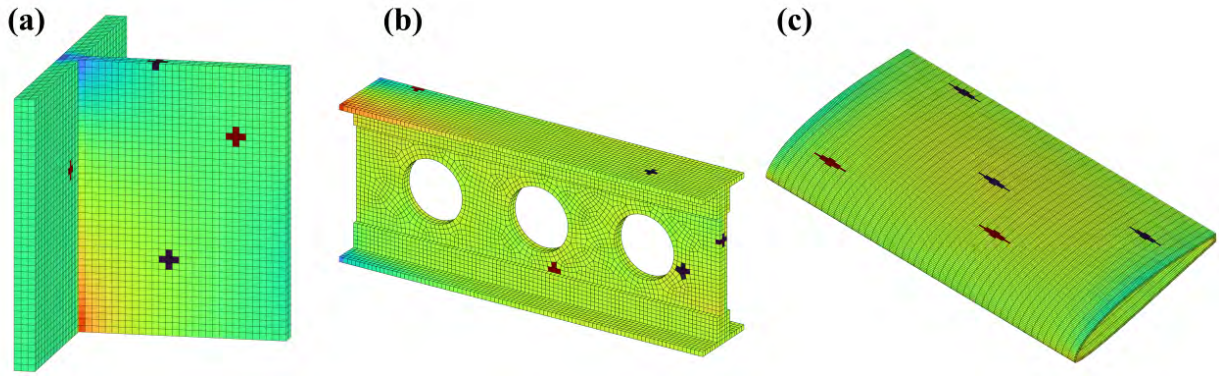

Figure 5.8. Resistivity data at 75 dB SNR with outliers for the (a) mounting bracket, (b) wing spar, and (c) airfoil.

6. COMPUTATIONAL EXPERIMENT RESULTS

6.1 Results of Displacement Data Fusion

6.1.1 Experiment 1

Figure 6.1 shows the sensor configurations used for this experiment. Recall that sensors are added two at a time on opposite sides of the shape—the numbers next to the sensor locations in figure 6.1 indicate the order in which a pair of DS were added.

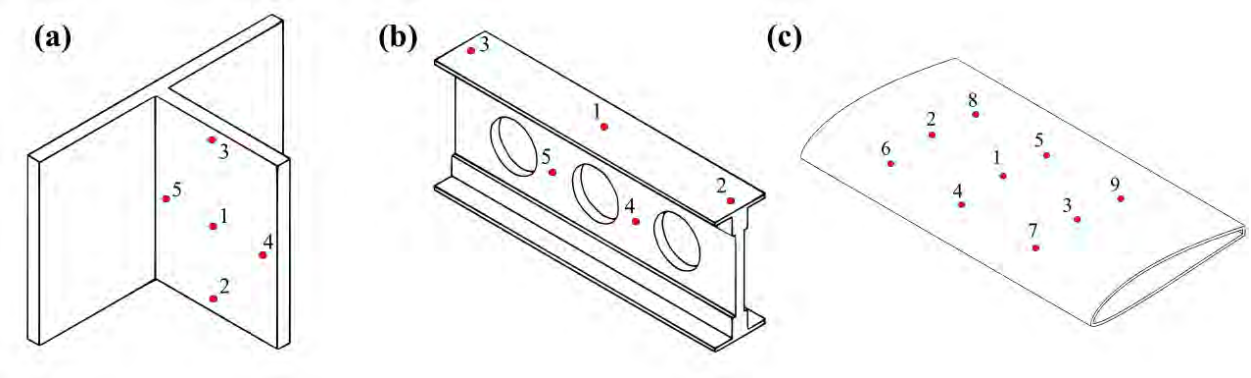

Figure 6.1. DS configurations used for Experiment 1 for the (a) mounting bracket, (b) wing spar, and (c) airfoil. The numbers indicate the order in which the sensors are added.

It is immediately apparent from figures 6.2, 6.3, and 6.4 that without DS, the SSIP reconstructions severely under-predicted the displacement magnitude and failed to capture the overall shape of the displacement field for every geometry. This is reflected in the displacement error plots, which show a minimal decrease in ϵ_d for cases without DS. Adding DS dramatically improved the accuracy of the recovered displacement fields. Up to 10 DS were activated for the mounting bracket and wing spar, and 18 DS for the airfoil. With this many DS, the displacement reconstructions are visually close to the exact solution. The displacement error plots reinforce this quantitatively, with the final ϵ_d of the maximum DS cases converging nearer to zero than all other cases.

Yet, the resistivity error plots in figure 6.6 show that ϵ_ρ for every single case, with and without DS, ϵ_ρ converged to near zero. A final ϵ_ρ value near zero indicates that the SSIP predicted resistivity distribution closely matches the simulated experimental resistivity dis-

tribution, which is a desired result. However, ϵ_ρ converged for all cases despite some predicted displacement fields being drastically different from each other and the exact solution. This result clearly demonstrates the underdetermined nature of the SSIP—the solution to the SSIP minimization is not unique. In other words, many displacement fields can map to the same resistivity distribution. Consequently, this makes it difficult to determine whether a displacement reconstruction is accurate from observing ϵ_ρ convergence alone. While this poses a challenge for the real world application of the SSIP where ϵ_d is not known, it is the goal of these computational experiments to demonstrate that SDF can provide more credence to the SSIP reconstructed displacement field such that future practitioners of SDF enhanced SSIP can be more confident with their results.

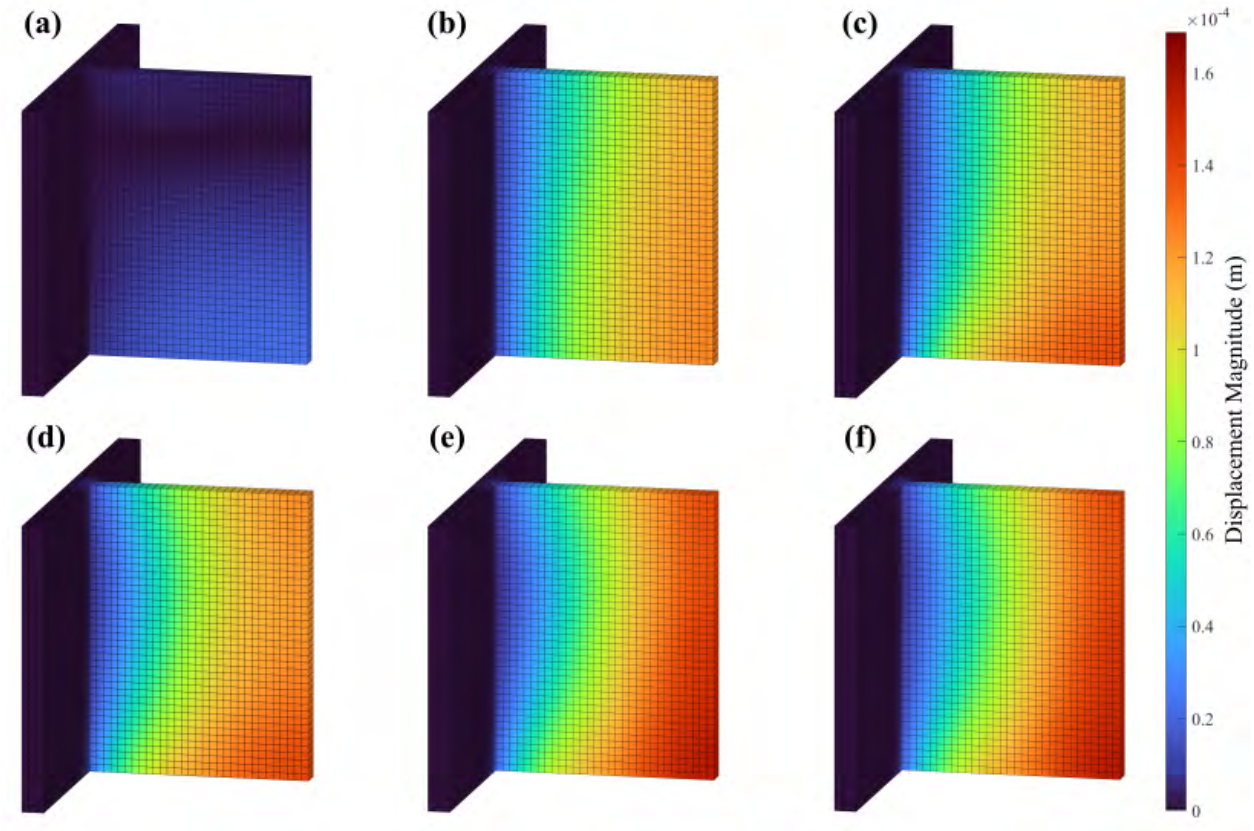

Figure 6.2. Displacement field reconstruction for the mounting bracket supplemented with displacement data from (a) 0, (b) 2, (c) 4, (d) 6, (e) 8, and (f) 10 DS.

One important behavior that can be observed visually is that increasing the number of DS improves the accuracy of the recovered displacement field, but the improvements diminish in magnitude as the recovered displacement field approaches the true displacement field. For instance, for the mounting bracket, only 2 DS were required to attain a displacement field close to the true displacement field magnitude, but it becomes difficult to visually discern improvements in accuracy beyond 6 DS. Plots of ϵ_d against the number of DS in figure 6.5 depict the diminishing improvements more clearly. For the mounting bracket and wing spar, after an early precipitous drop in ϵ_d, improvements stagnate quickly. For the airfoil, there were two distinct drops at 2 DS and 10 DS. This likely occurred because DS tend to improve the accuracy of the recovered displacement field locally. The fifth sensor pair was the first pair in the aft section of the airfoil, thus extending the region of accuracy toward that section of the geometry. While optimizing sensor location is not the focus of this research, this highlights that sensor location can have a significant impact on the quality the SSIP displacement field recovery.

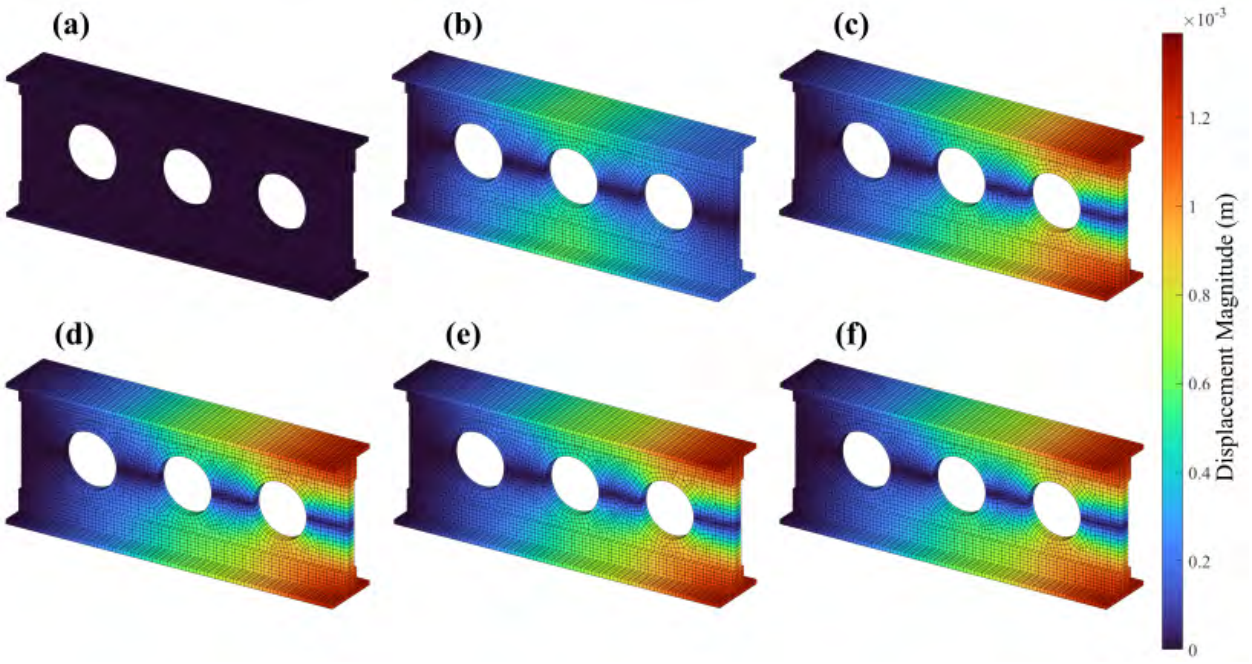

Figure 6.3. Displacement field reconstruction for the wing spar supplemented with displacement data from (a) 0, (b) 2, (c) 4, (d) 6, (e) 8, and (f) 10 DS.

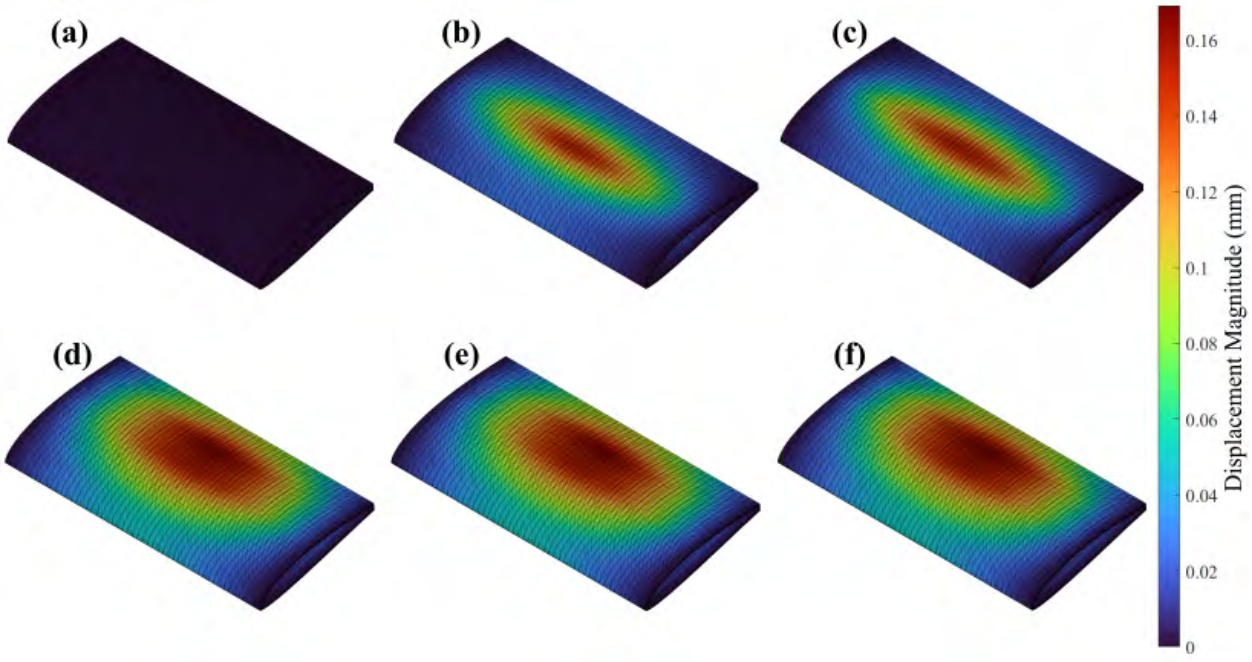

Figure 6.4. Displacement field reconstruction for the airfoil supplemented with displacement data from (a) 0, (b) 2, (c) 6, (d) 10, (e) 14, and (f) 18 DS.

Another important behavior to note is that the resistivity error for cases with DS behaves more unstably compared cases without DS. For the mounting bracket, ϵ_ρ plateaued before converging toward zero after the tenth iteration, and, for the wing spar and airfoil, ϵ_ρ actually increased during the first ten iterations. This is attributed to the displacement data ramping method described in section 4.2. Since the DS nodes do not constrain the minimization, the SSIP finds a displacement field that satisfies the minimization without contribution from DS nodes. When the displacement data are manually inserted into $\boldsymbol{d}^n$, the new $\boldsymbol{d}^n$ is no longer the vector predicted by the SSIP that satisfied the minimization. Therefore, ϵ_ρ for reconstructions with SDF tends to be larger and less stable than the ϵ_ρ in cases without SDF during the data ramping phase. Despite this, in all cases, resistivity error converges to nearly zero after the data ramping was complete.

To determine the number of DS required to reconstruct a sufficiently accurate displacement field, the ϵ_d versus the number of sensors plots were used. These plots displayed a clear point where adding additional DS did not appreciably improve the accuracy of the displacement reconstruction. The number of DS at this inflection point was selected. The rationale

behind this decision metric is similar to one of the considerations engineers must make when instrumenting structures for NDE: to determine the most efficient sensor configuration in order to minimize cost and complexity.

Thus, it was concluded that a minimum of 4 DS for the mounting bracket and wing spar, and 10 DS for the airfoil were required in order to obtain a reasonably accurate displacement field reconstruction. And in general, SDF of displacement and resistivity data significantly improves the SSIP displacement field recovery. Additionally, these sensor configurations were then used in Experiments 2 and 3.

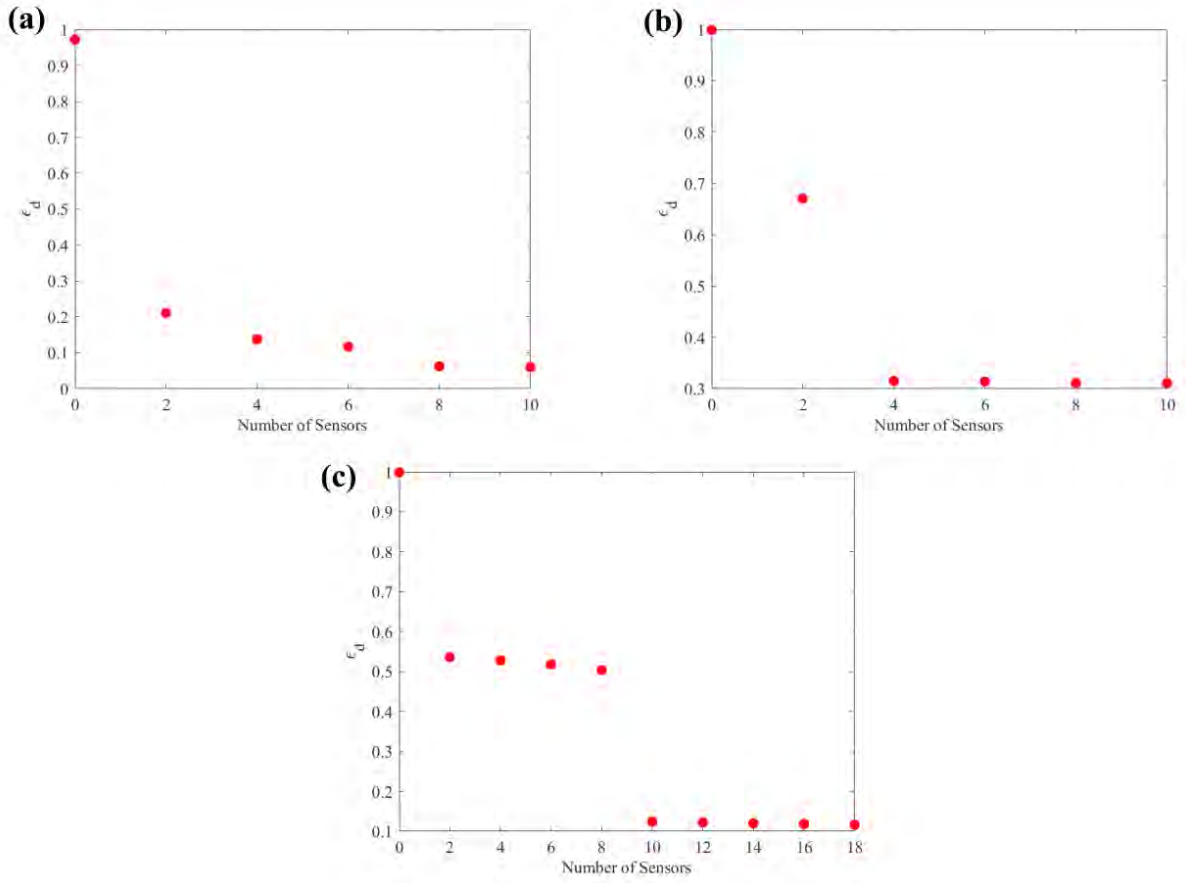

Figure 6.5. Displacement data fusion Experiment 1 ϵ_d versus number of sensors plot for the (a) mounting bracket, (b) wing spar, and (c) airfoil.

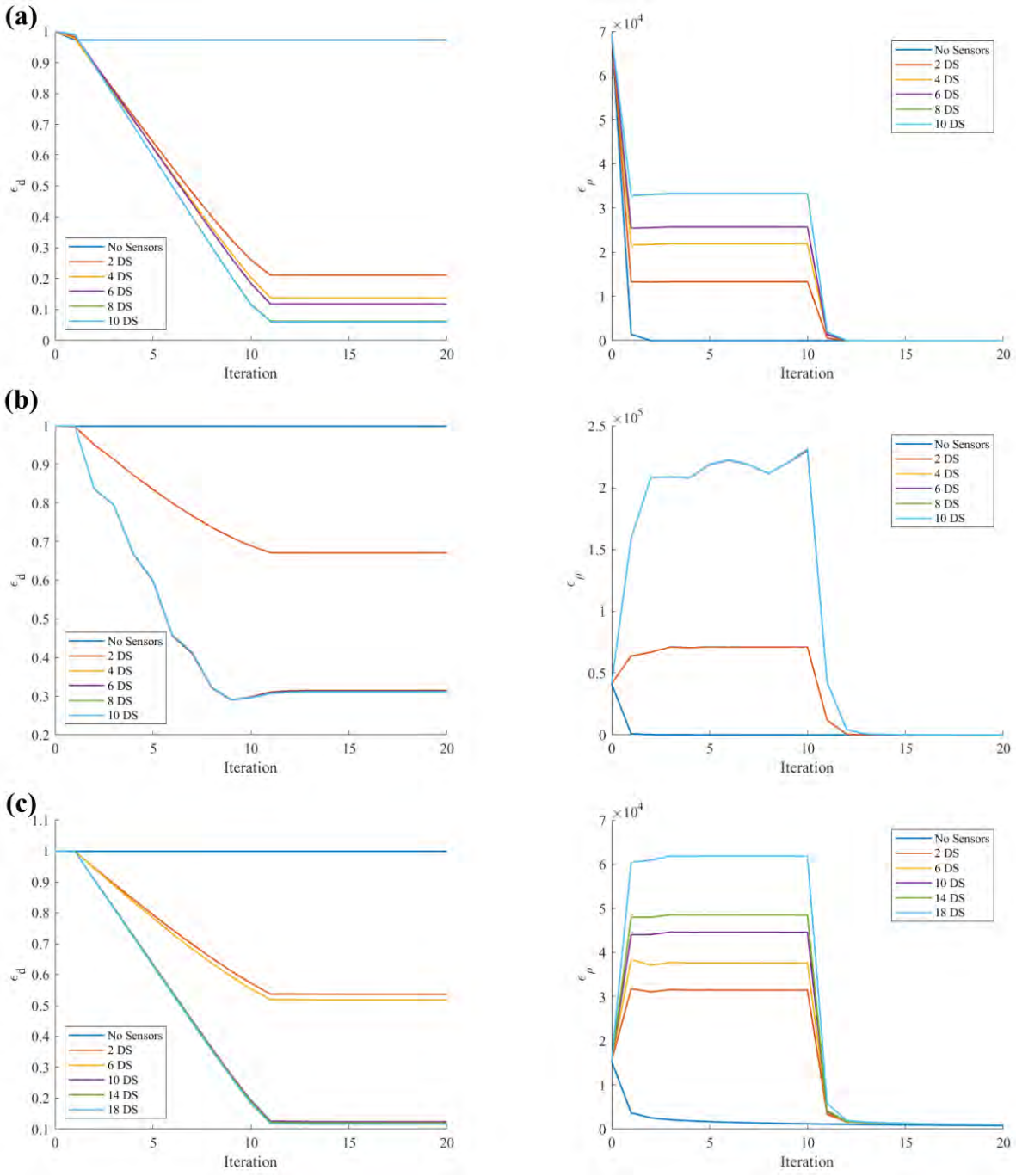

Figure 6.6. Displacement data fusion Experiment 1 displacement error plots (left) and resistivity error plots (right) for the (a) mounting bracket, (b) wing spar, and (c) airfoil.

6.1.2 Experiment 2

Figure 6.7 displays the sensor configuration used for each geometry. The displacement fields recovered from the 75 dB SNR resistivity data were shown in the previous subsection, so they are not presented again here. Figures 6.8 through 6.10 show the displacement field recovered from 50 dB, 40 dB, and 30 dB SNR resistivity data. For the airfoil, the results for the 30 dB SNR resistivity data are omitted because the noise was too high for meaningful results to be obtained. The noise profiles were generated with respect to the absolute resistivity, and the resistivity changes for the airfoil load case were much smaller compared to the mounting bracket and wing spar load cases. Figure 6.14 gives the displacement error and resistivity error plots for each geometry.

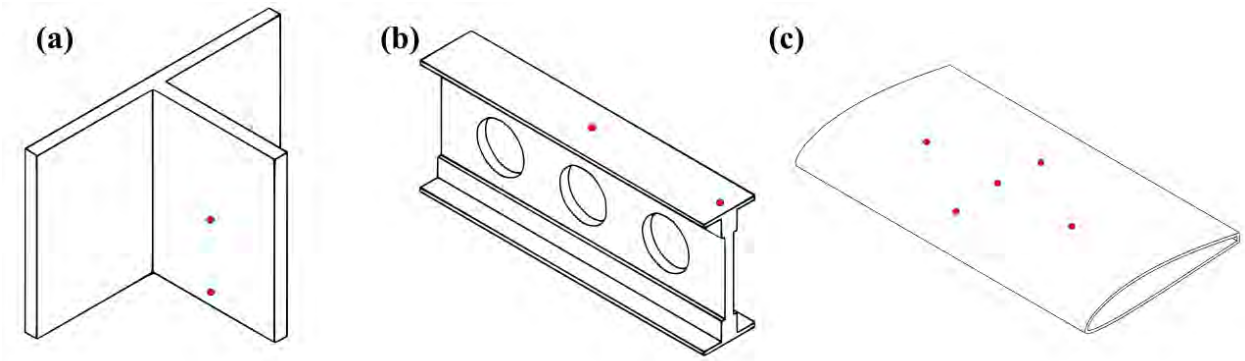

Figure 6.7. DS configuration used for Experiment 2 for the (a) mounting bracket, (b) wing spar, and (c) airfoil.

Figures 6.8, 6.9, and 6.10 show that the general shape and magnitude of the displacement reconstructions were largely captured even at low SNR for every shape. However, upon close inspection, aberrations can be observed. These noise aberrations are most distinct on the flange of the mounting bracket. On the mounting bracket flange, minimal displacement was expected because of the nearby fixed boundary condition, but the resistivity data noise caused the SSIP to predict small displacements throughout this region.

For the wing spar and airfoil, the effects of noise were not immediately apparent. The aberrations caused by noise are more clearly seen when each displacement component is displayed separately. Figures 6.11, 6.12, and 6.13 compare the exact x, y, and z displacements

to the displacement reconstructions obtained from the lowest SNR resistivity data attempted and the reconstructions from Experiment 1 using the same sensor configuration. From these figures, it can be seen that the quality of the displacement reconstructions from lower SNR resistivity data are noticeably degraded from the Experiment 1 results. One notable trend is that for all geometries, the smaller magnitude displacement components were more affected by the noise than the comparatively larger displacement component. For instance, for the airfoil, the maximum displacement in the y direction was two orders of magnitude larger than the maximum displacement in the x and z directions. As noise increased, the y displacement reconstructions remained relatively intact while the other components deviated further from exact solution. Similar observations can be made for the wing spar, where the z displacement dominated, and for the mounting bracket, where y and z displacements were much larger than the x displacements.

The plots in figure 6.14 show that ϵ_ρ tended to be larger with increasing noise while ϵ_d was fairly robust to change. The initial ϵ_ρ was larger at higher levels of noise because the SSIP initially predicts a uniform resistivity distribution where the resistivity of every element in the mesh is equal to $\rho_0 = 75{,}000\ \Omega \cdot m$. A noisier resistivity distribution will on average be further from the initial SSIP prediction. However, the final ϵ_ρ was different at each noise despite the final ϵ_d remaining consistent. This happened because the correct displacement field possesses a different resistivity distribution than the noisy resistivity data; therefore, the final ϵ_ρ tends to be larger at lower SNR.

In conclusion, the results of this experiment demonstrated that SDF of resistivity and displacement data improves the reliability of the SSIP displacement field recovery when resistivity data noise is increased.

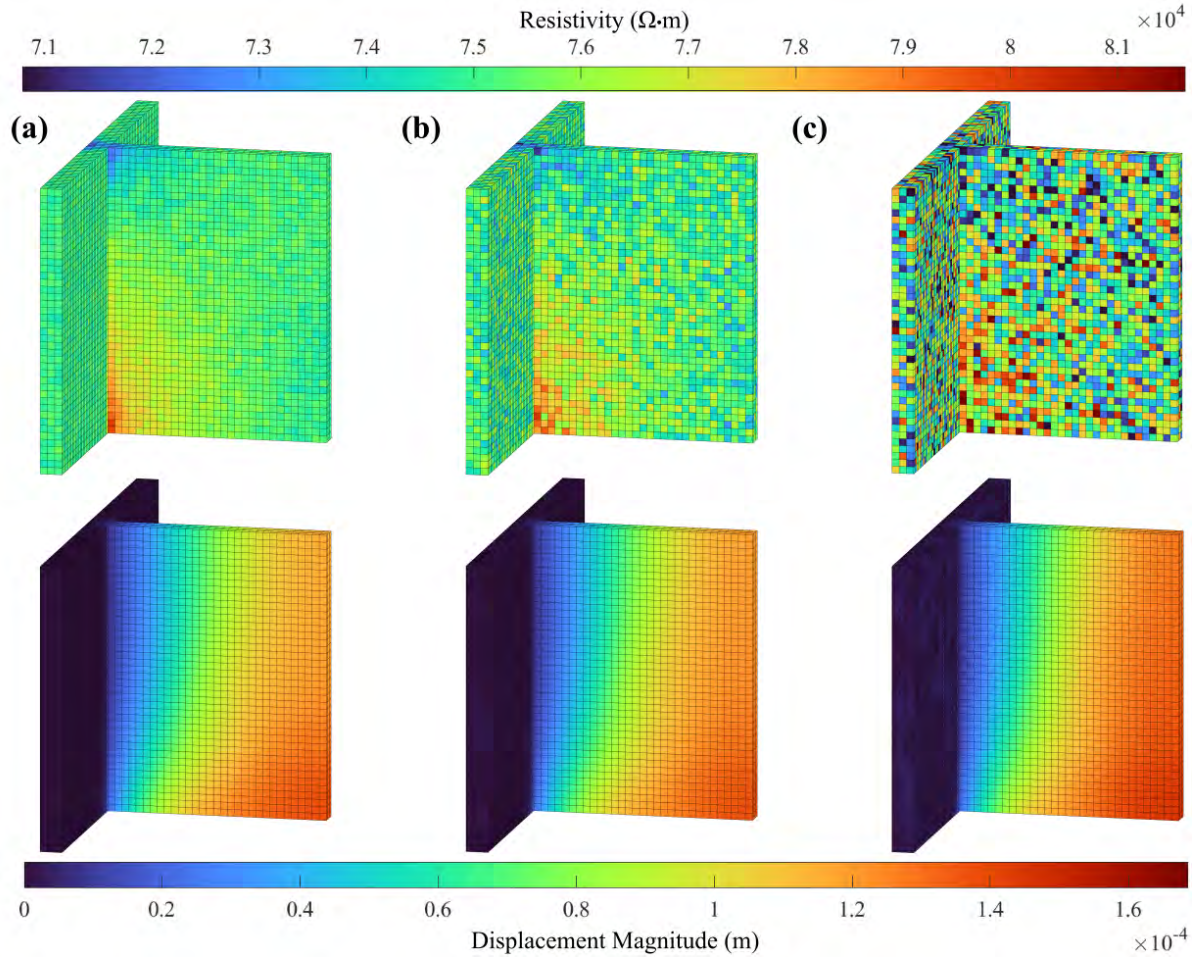

Figure 6.8. From left to right, each column shows the resistivity data (top) and displacement reconstruction (bottom) for (a) 50 dB, (b) 40 dB, and (c) 30 dB SNR for the mounting bracket using 4 DS.

6.1.3 Experiment 3

Figures 6.15 through 6.17 show the sensor configurations used and the corresponding displacement reconstruction for each geometry. The sensor configuration from Experiment 1 and a second configuration using more numerous sensors were used. At a glance, the resistivity data with outliers seem to have posed a steeper challenge for the displacement field recovery than data at the noise levels in Experiment 2. The mounting bracket and wing spar displacement fields were reconstructed using 4 and 8 DS, and the airfoil displacement field was reconstructed using 10 and 18 DS.

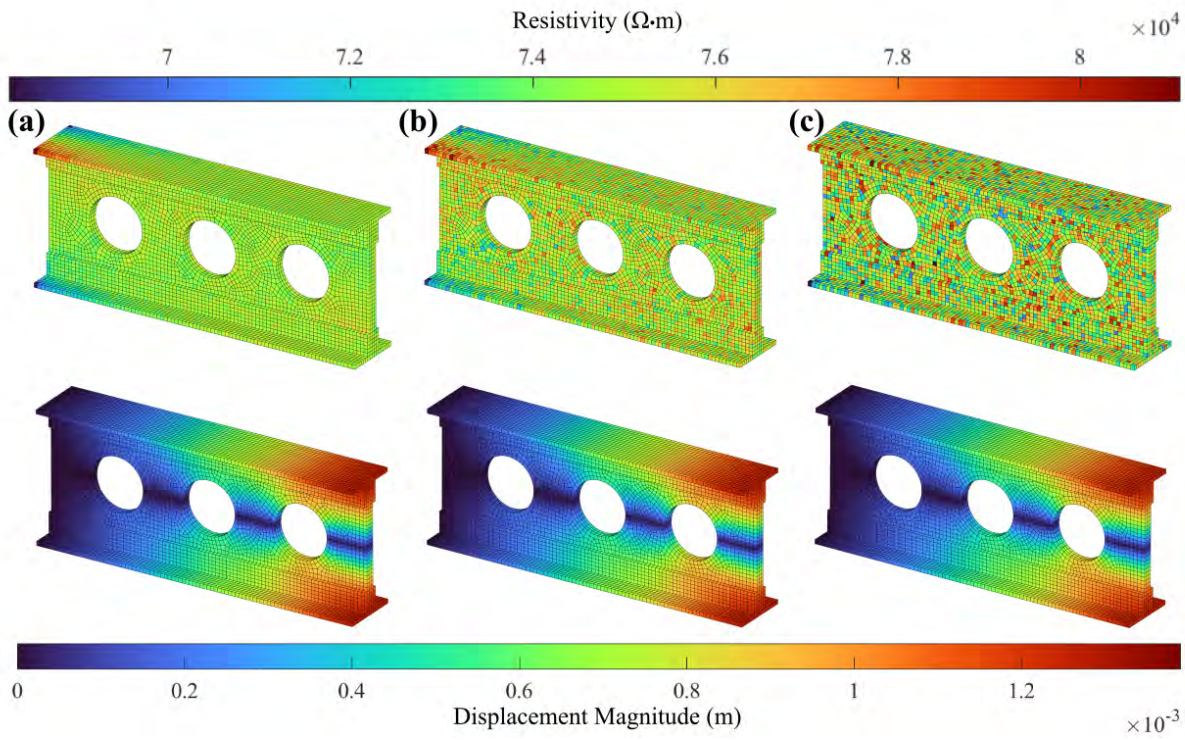

Figure 6.9. From left to right, each column shows the resistivity data (top) and displacement reconstruction (bottom) for (a) 50 dB, (b) 40 dB, and (c) 30 dB SNR for the wing spar using 4 DS.

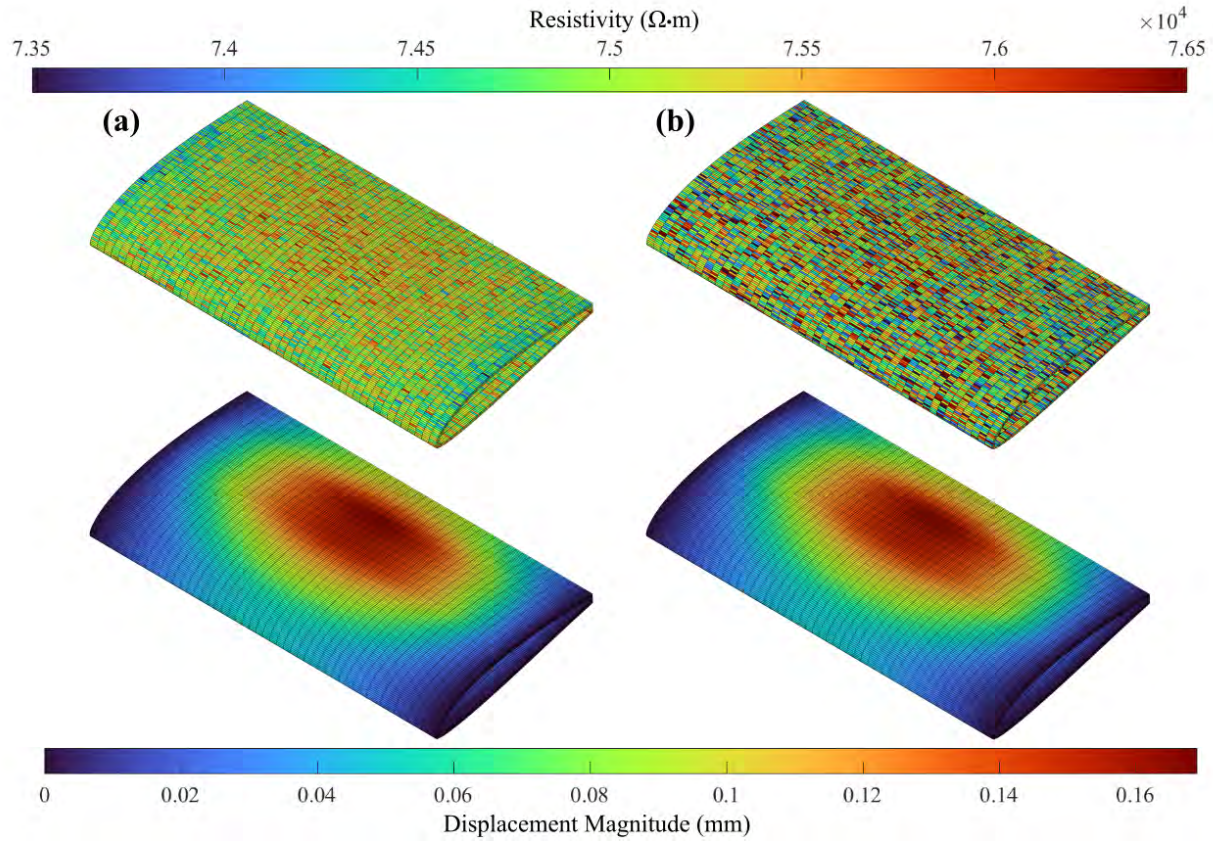

Figure 6.10. From left to right, each column shows the resistivity data (top) and displacement reconstruction (bottom) for (a) 50 dB and (b) 40 dB SNR for the airfoil using 10 DS.

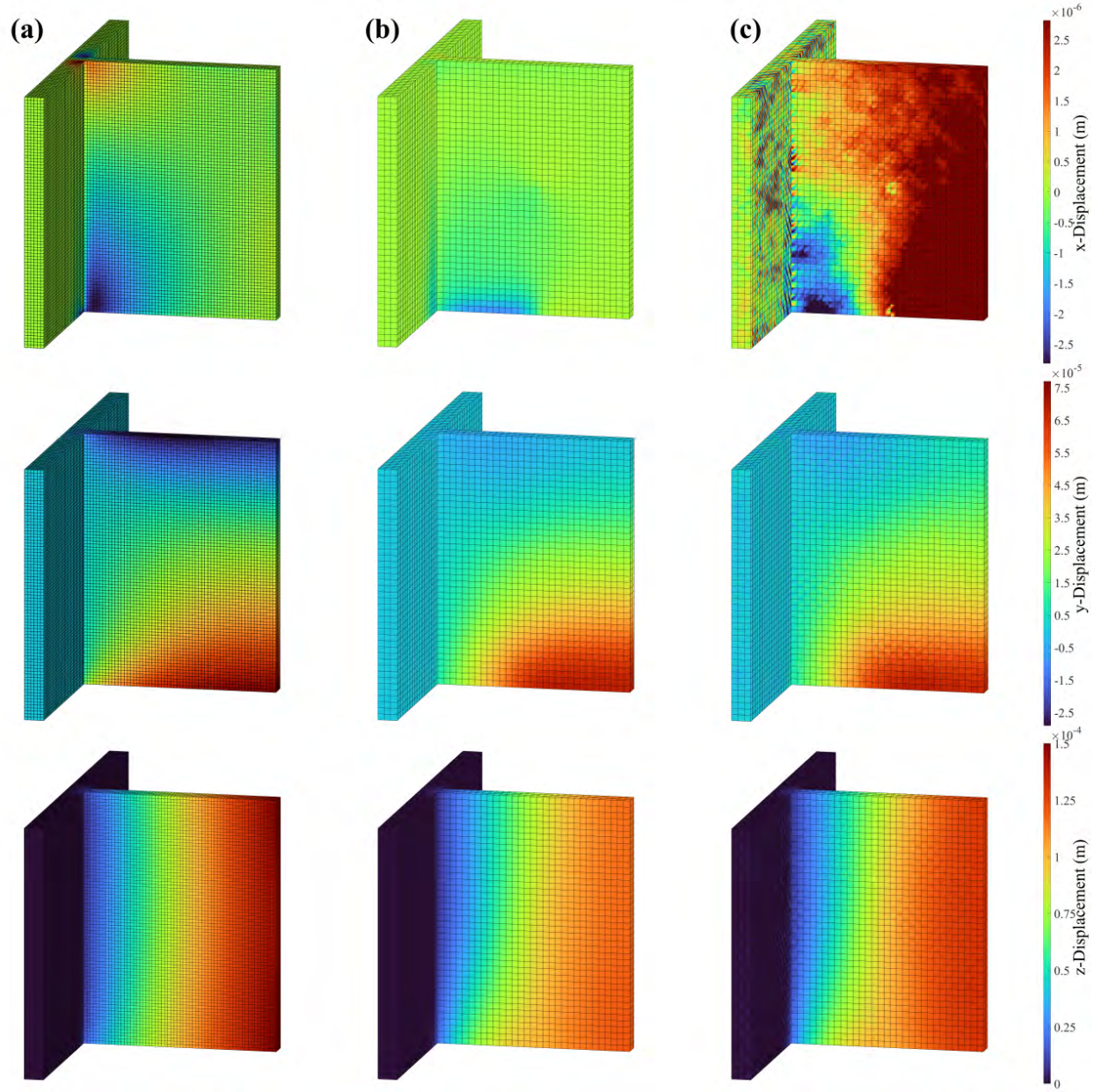

Figure 6.11. From left to right, a comparison of the (a) exact displacement field solution to the displacement reconstruction using (b) 4 DS at 75 dB SNR and (c) 4 DS at 30 dB SNR for the mounting bracket, broken down by displacement component.

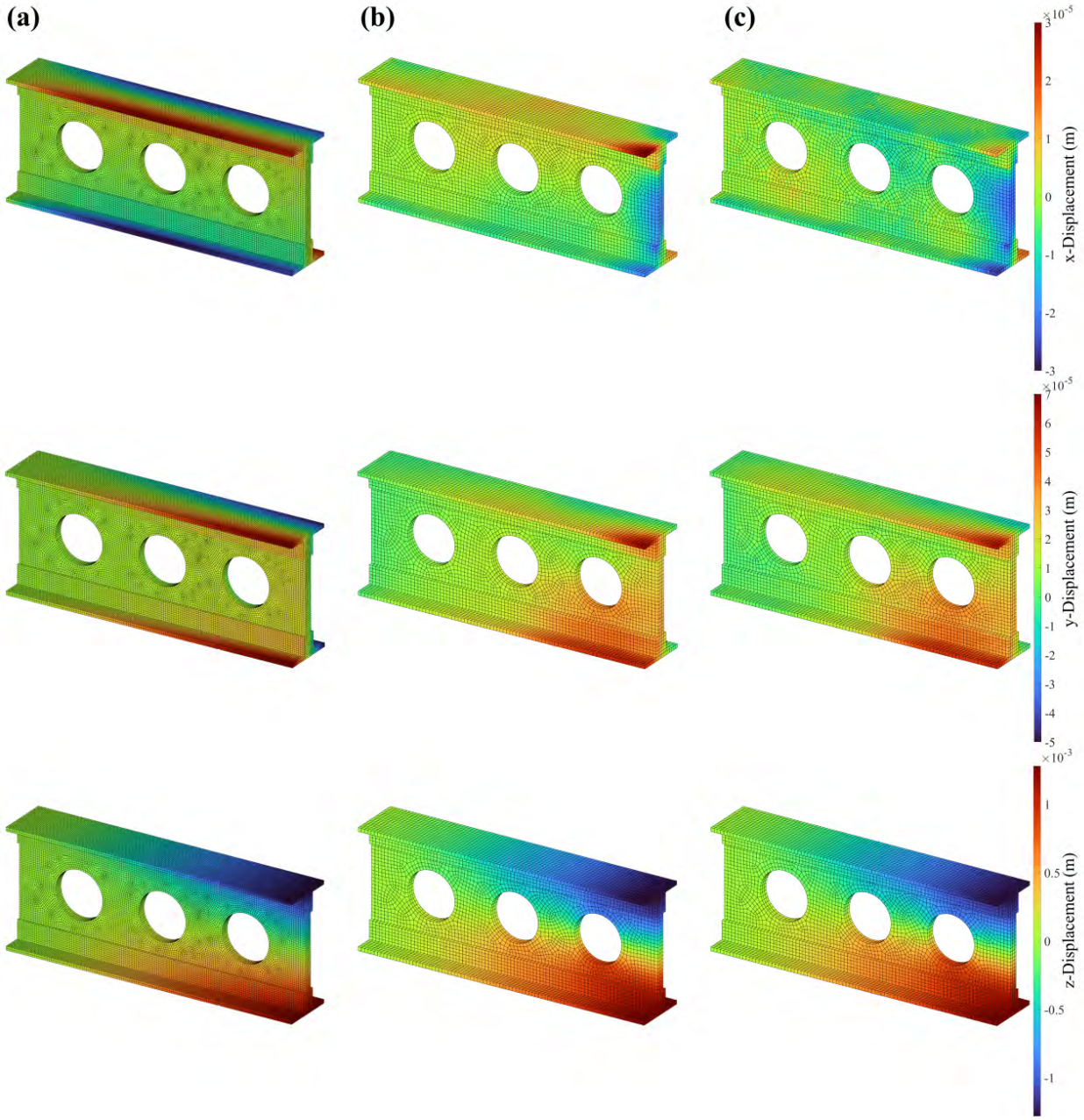

Figure 6.12. From left to right, a comparison of the (a) exact displacement field solution to the displacement reconstruction using (b) 4 DS at 75 dB SNR and (c) 4 DS at 30 dB SNR for the wing spar, broken down by displacement component

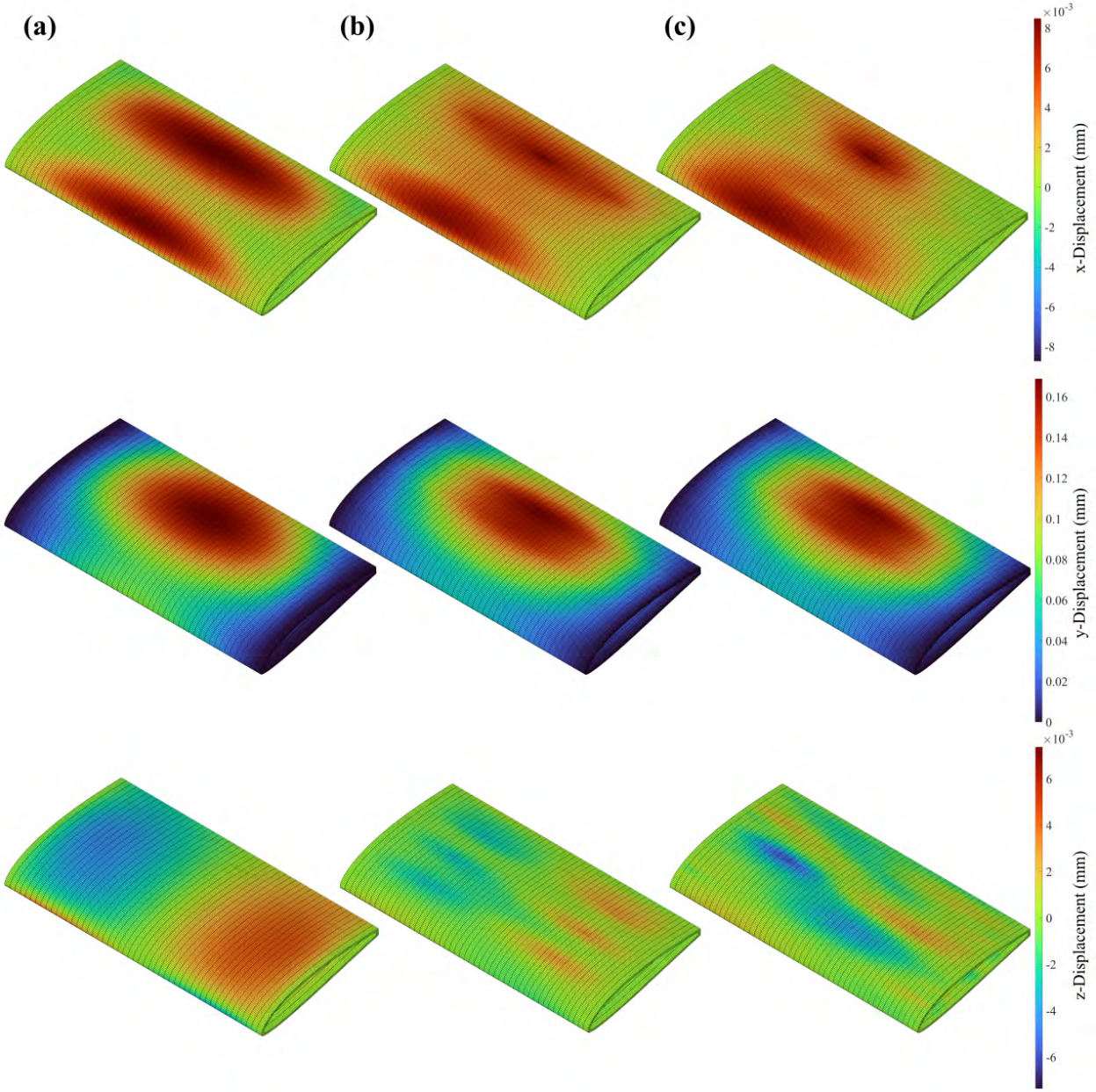

Figure 6.13. From left to right, a comparison of the (a) exact displacement field solution to the displacement reconstruction using (b) 10 DS at 75 dB SNR and (c) 10 DS at 40 dB SNR for the airfoil, broken down by displacement component

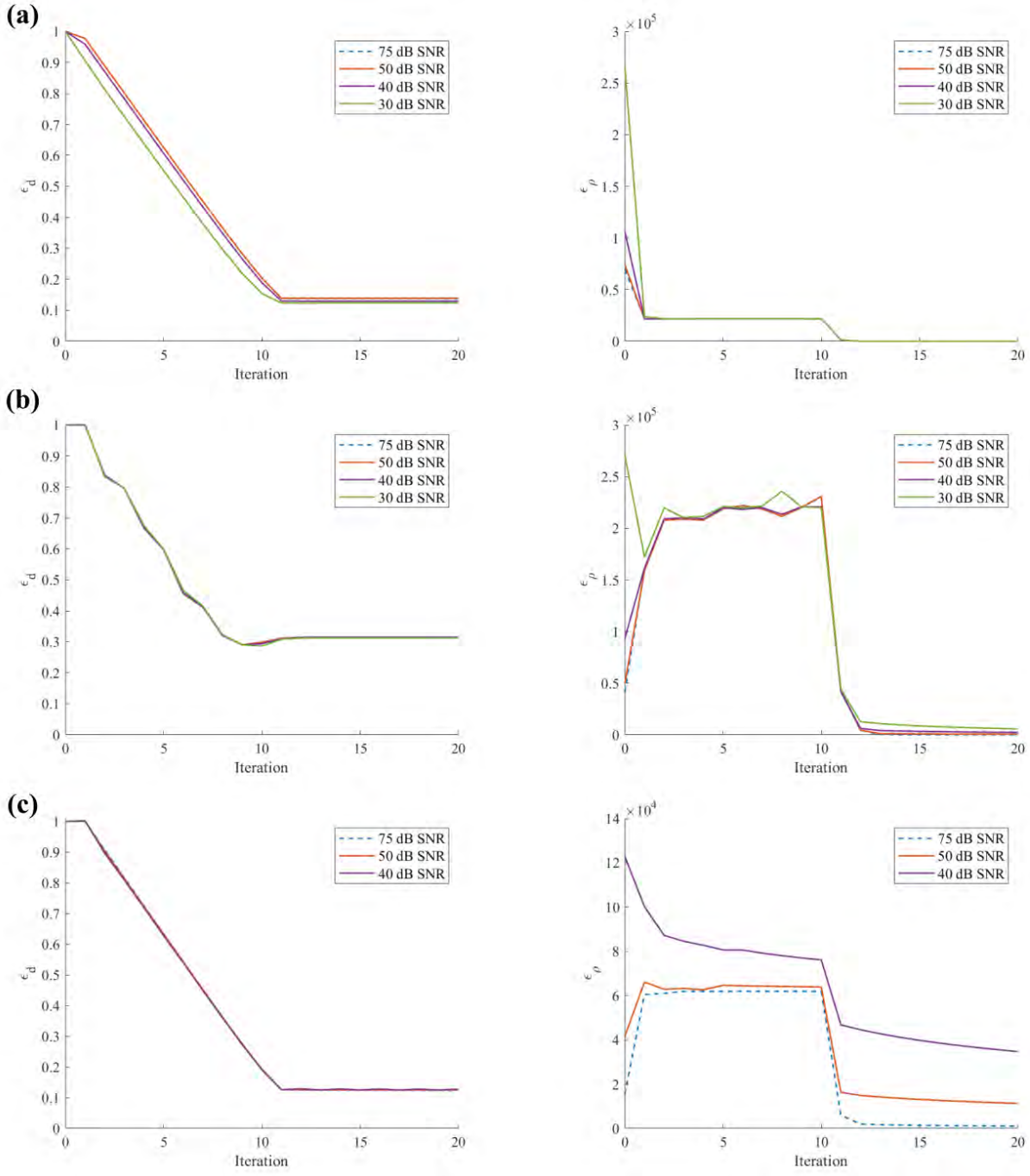

Figure 6.14. Displacement data fusion Experiment 2 displacement error plots (left) and resistivity error plots (right) for the (a) mounting bracket, (b) wing spar, and (c) airfoil.

As seen in figure 6.15, with 4 DS the shape of the displacement field shape was roughly captured, albeit with significant aberrations caused by the outlier data and an over-prediction of the displacement magnitude. Increasing to 8 DS, the displacement magnitude was better captured overall, but the aberrations persisted. The displacement error plot in figure 6.18 for the mounting bracket demonstrates how negatively the outliers affected the reconstruction, with the final ϵ_d increasing substantially when outlier data were introduced. The final ϵ_d for the outlier data reconstruction with 4 DS was about eight times larger than the reconstruction without outliers using the same sensor configuration. Increasing the number of sensors to eight improved the convergence toward the correct displacement field, but it ultimately was not as accurate as the resistivity data without outliers.

The outlier effects were less dramatic for the wing spar. Overall, the displacement magnitude was well captured, but the shape of the displacement field was skewed by the outlier data. Like the mounting bracket, increasing the number of DS improved the accuracy of the reconstructed displacement field, but aberrations caused by the outliers were not fully erased. The displacement error plot shows that ϵ_d diverges after the displacement data ramping was complete using 4 DS. At 8 DS, ϵ_d tracks closely with the ϵ_d curve for the reconstruction without outlier data. Although ϵ_d was diverging for the 4 DS case, ϵ_ρ was clearly converging toward zero, indicating that ϵ_d would eventually stabilize at some point if the iterations were allowed to continue.

The airfoil fared the best out of the three geometries in the face of outlier data. Using 10 DS, faint aberrations at outlier data locations are visible, most noticeable at the left side near the leading edge, but the displacement field shape and magnitude are otherwise largely well captured. Additionally, ϵ_d tracked close to the no outlier case except for mild oscillatory behavior after the end of data ramping. Thus, increasing to 18 DS resulted in no perceivable improvement.

The conclusion drawn from this experiment is that while SDF of displacement and resistivity data can generally improve the SSIP displacement field recovery, a good reconstruction is not always guaranteed. This is because the efficacy of DS in ameliorating the negative effects of outliers was not consistent across all cases shown. In the case of airfoil, the displacement reconstructions were of reasonable quality, but for the mounting bracket and wing spar,

outlier caused aberrations remained prominent, even when the number of DS were increased. This inconsistency can be attributed to the fact that the degree to which outlier data destabilize the SSIP depends on the outlier data frequency, magnitude, and location as well as the geometry and load case. Therefore, it may be more beneficial to apply minimization schemes more aptly designed to address outlier data in addition to SDF.

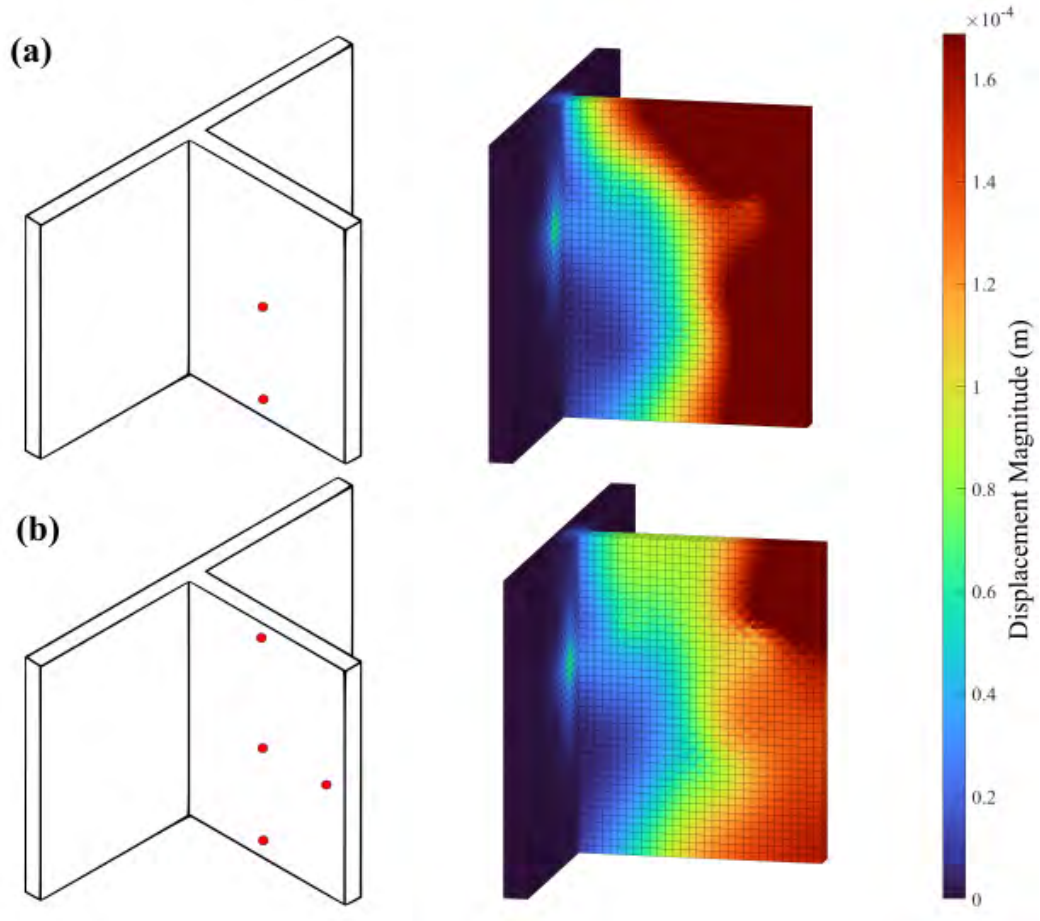

Figure 6.15. Sensor configuration (left) and outlier resistivity data displacement reconstruction (right) for the mounting bracket using (a) 4 DS and (b) 8 DS.

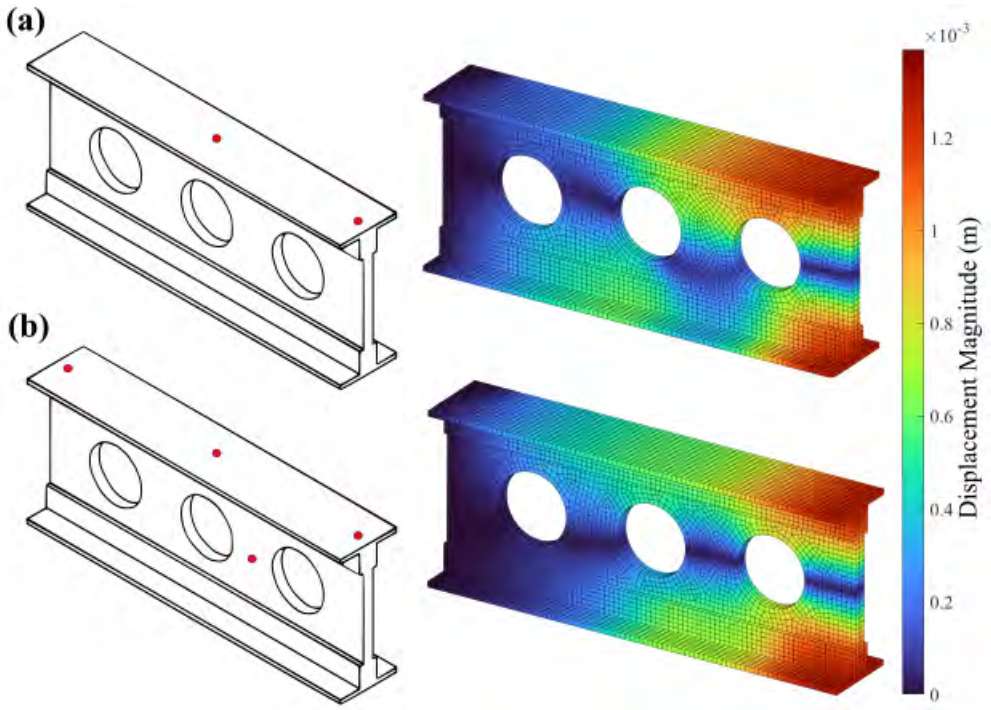

Figure 6.16. Sensor configuration (left) and outlier resistivity data displacement reconstruction (right) for the wing spar using (a) 4 DS and (b) 8 DS

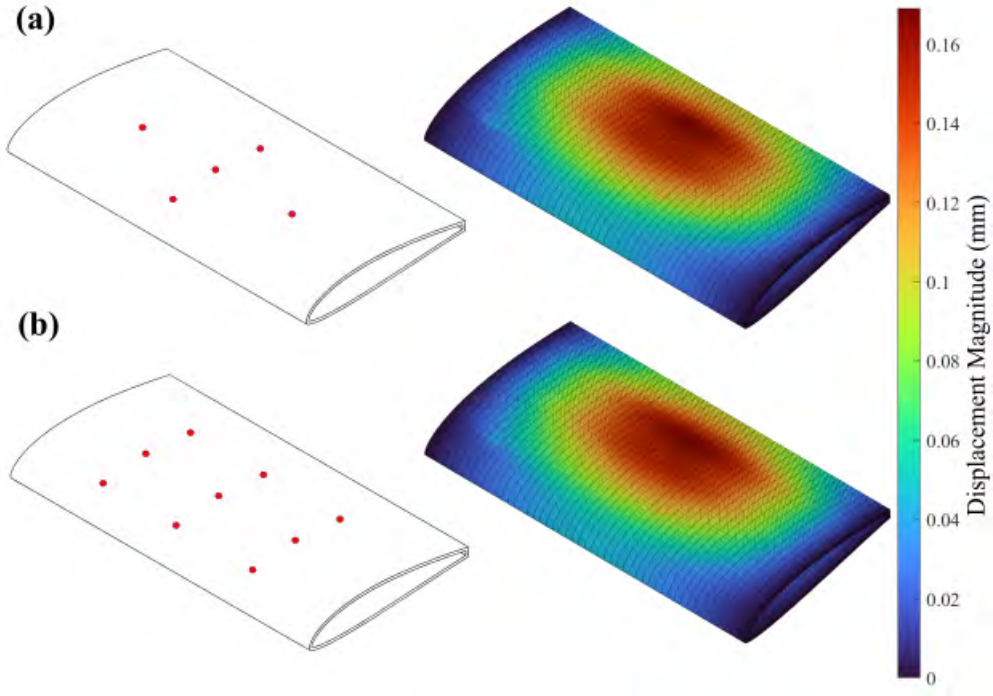

Figure 6.17. Sensor configuration (left) and outlier resistivity data displacement reconstruction (right) for the airfoil using (a) 10 DS and (b) 18 DS

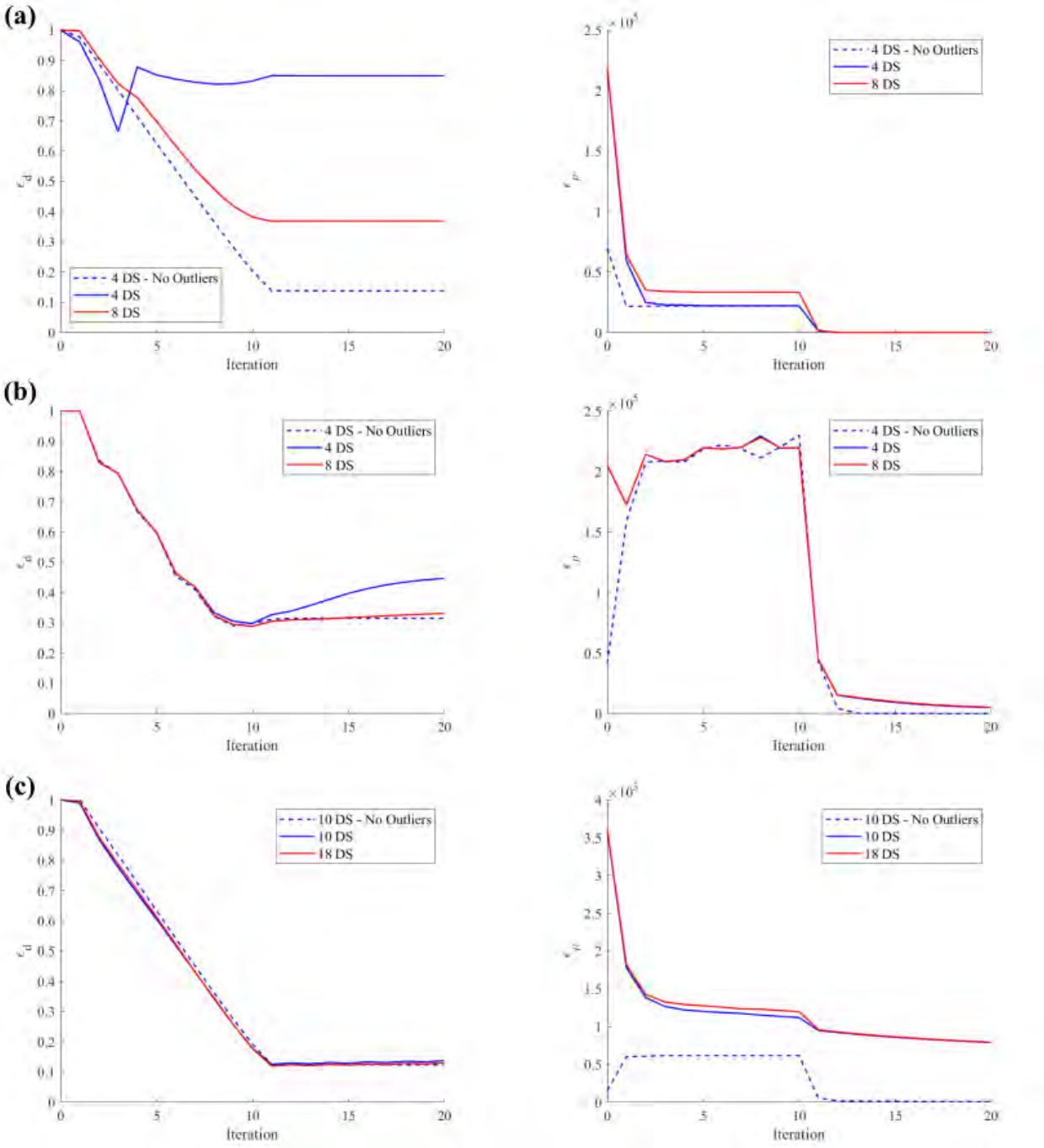

Figure 6.18. Displacement data fusion Experiment 3 displacement error plots (left) and resistivity error plots (right) for the (a) mounting bracket, (b) wing spar, and (c) airfoil.

6.2 Results of Strain Data Fusion

As mentioned in section 4.3, according to iFEM literature, large weights are assigned to elements with strain data, and smaller weights are assigned to elements without strain data, generally smaller by a factor of 1×10^{-3} to 1×10^{-6} relative to the large weights. Aside from this general guidance, there does not exist a strict mathematical methodology for selecting values for the weight coefficients. In this research, the weight for SS elements was selected such that the corresponding entries of $\boldsymbol{K}$ became, on average, the same order of magnitude as the entries of the $\boldsymbol{G}$ matrix. Thus, the weight for the SS elements were selected to be 1×10^2 for the mounting bracket and wing spar, and 1×10^8 for the airfoil. The weights for non-SS elements were selected to be 1×10^{-2} for the mounting bracket and wing spar, and 1×10^4 for the airfoil.

Additionally, unlike the DS experiments where all displacement components were known, only the in-plane strains were known at each SS to simulate the data from a strain gauge rosette. The strains used for strain data were calculated from the exact displacement solution and were in the global reference frame. For the mounting bracket, all SS were placed on the web which was aligned with the global y and z axes; therefore, ε_{22}, ε_{33}, and ε_{23} were known at each SS. For the wing spar, SS were placed on both the spar caps and the web. The SS on the spar caps provided ε_{11}, ε_{33}, and ε_{13}, and SS on the web provided ε_{11}, ε_{22}, and ε_{12}. For the airfoil, the SS provided ε_{11}, ε_{33}, and ε_{13}. Although the curved surface made it so that the SS were not aligned to the global x axis, it is assumed that the strains measured in the element reference frame can be rotated to the global ε_{11} in experimental application.

6.2.1 Experiment 1

Figure 6.19 displays the sensor configurations used for this experiment. The red circles designate the maximum sensor configuration used in the DS experiments. Up to this sensor configuration, the sensors were added in the same order as in figure 6.1. It was found in some cases that the addition of SS had a very small impact on the displacement reconstruction; therefore, after the reaching the maximum number of sensors used in the DS experiments, eight additional sensors are added at a time (instead of two) up to a total of 50 SS. The order

in which each additional set of eight SS were added are signified by different color circles in figure 6.19.

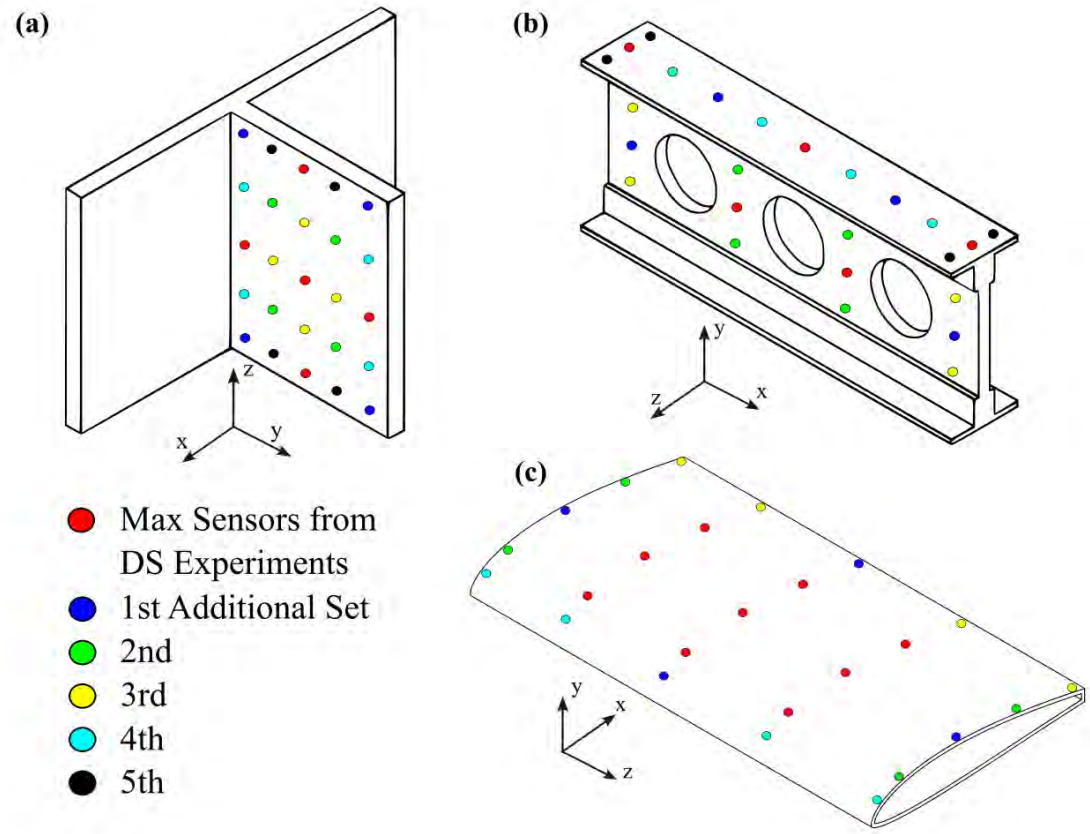

Figure 6.19. SS configurations for Experiment 1 for the (a) mounting bracket, (b) wing spar, and (c) airfoil. Colors indicate the order in which each additional set of sensors is added.

Figures 6.20, 6.21, and 6.22 show the displacement reconstructions using 2, 10, 18, 34, and 50 SS for the mounting bracket, wing spar, and airfoil, respectively. In all cases, increasing the number of SS increases the accuracy of the reconstructed displacement field. For all shapes, at 50 SS, the shape of the displacement field was well captured, but the magnitude of the displacement was underpredicted. The SDF enhanced reconstructions are nonetheless a significant improvement over the reconstructions without any additional sensor data.

However, it can be seen visually, and quantitatively in the plots in figures 6.23 and 6.24, that the mounting bracket displacement reconstruction is much closer to the exact solution than the wing spar and airfoil are at 50 SS. This is likely because of the orientation

and location of the SS. For the mounting bracket, the SS were aligned with the largest magnitude strain components the shape experienced. As a result of the tension loading, ε_{22}, ε_{33}, and ε_{23} dominated other strain components and were large throughout the web, and the SS were uniformly distributed throughout this area, collecting ε_{22}, ε_{33}, and ε_{23} data. In contrast, the twist loading in the wing spar produced large ε_{11} strains at its root near the fixed displacement boundary condition and relatively minute strains everywhere else. However, the majority of the SS were placed far from these large strains. Similarly, for the airfoil, while there was no dominant strain component, the largest magnitude strains were concentrated at the root and tip of the shape near the boundary conditions, whereas the majority of the SS were at the middle section. Concentrating more SS in areas with large expected strains may improve the overall displacement field construction, but optimizing sensor location is outside the scope of this research.

The resistivity error plots in figure 6.23 demonstrate stable convergence of ϵ_ρ toward zero for all cases. The ϵ_d versus number of sensors plots were again used to identify the point of diminishing improvement in the recovered displacement field. For the mounting bracket, this point occurred at 18 SS. However, for the wing spar and airfoil, after a steep initial drop in ϵ_d that occurred with the first two SS added, ϵ_d decreased roughly linearly by a very small amount up to the 50 SS configuration. While the 2 SS configuration could be selected as the point of diminishing improvement, the 18 SS configuration was selected instead. This was because, given the reconstructions for the wing spar and airfoil were not as accurate as the mounting bracket, 2 SS was deemed too few. Instead, by removing the data point at 0 SS, ϵ_d at 18 SS was approximately halfway between the maximum and minimum ϵ_d for the remaining data points. Therefore, 18 SS was chosen as the minimum number of SS that satisfied the tradeoff between number of sensors and relative reconstruction accuracy for all geometries.

From the results of this experiment, it was shown that SDF of strain and resistivity data mildly improves the SSIP displacement field recovery, being able to capture the shape of the true displacement field but under-predicting its magnitude.

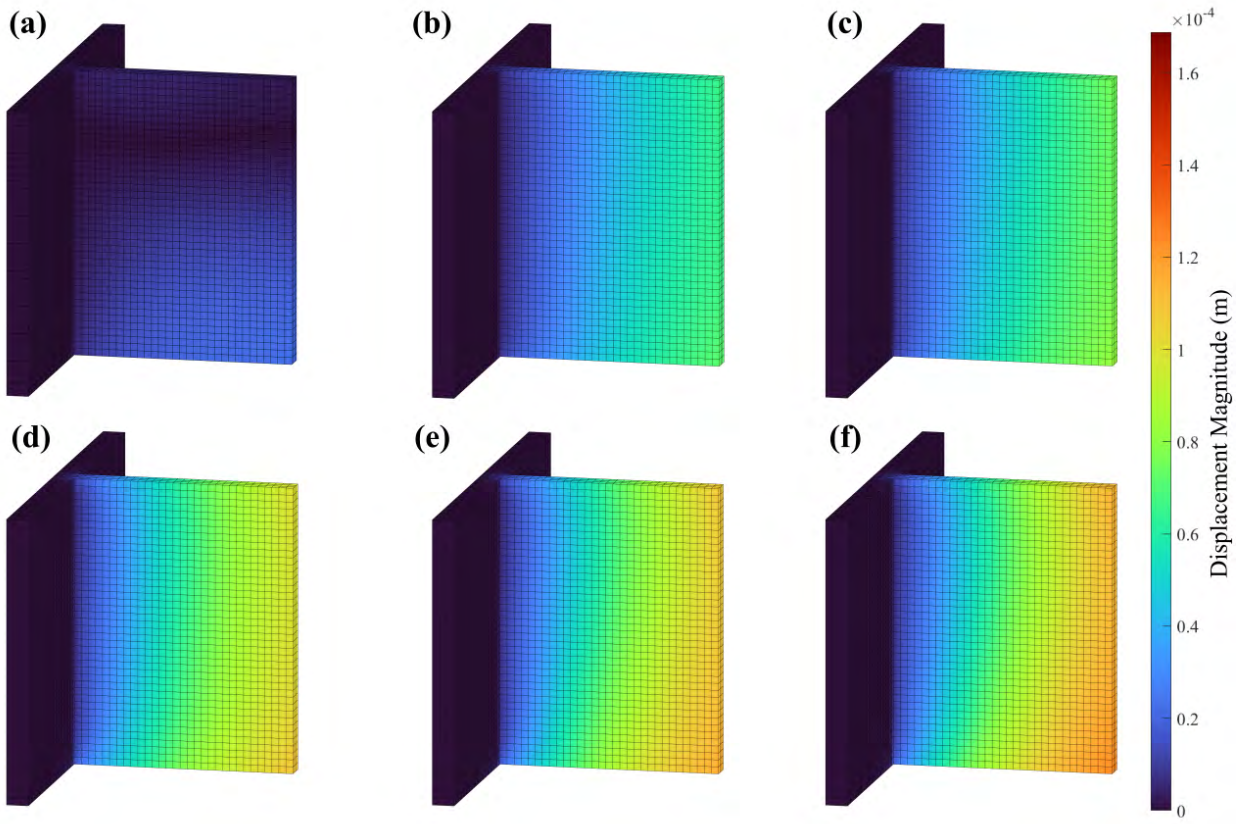

Figure 6.20. Displacement field reconstruction for the mounting bracket supplemented with displacement data from (a) 0, (b) 2, (c) 10, (d) 18, (e) 34, and (f) 50 SS.

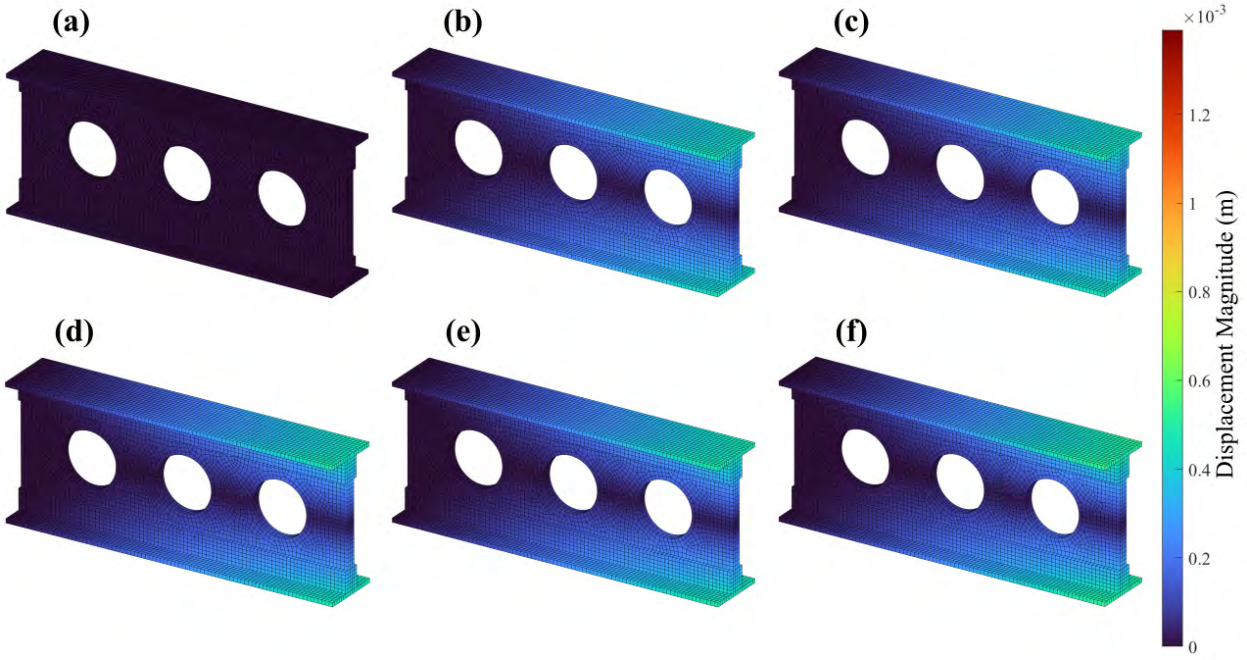

Figure 6.21. Displacement field reconstruction for the wing spar supplemented with displacement data from (a) 0, (b) 2, (c) 10, (d) 18, (e) 34, and (f) 50 SS.

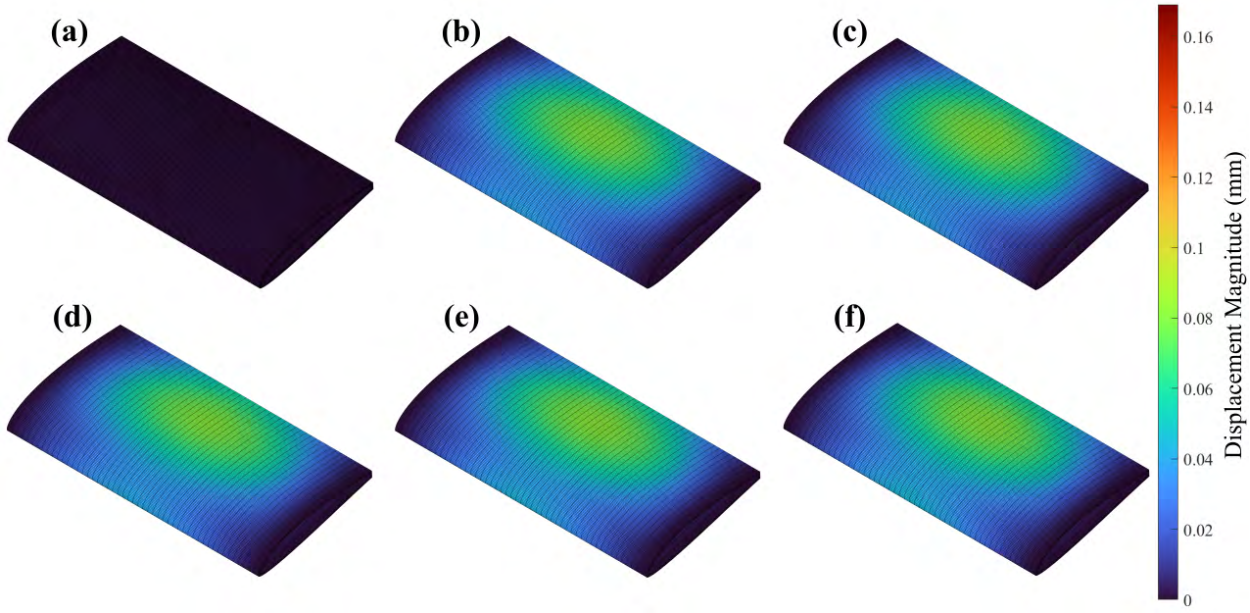

Figure 6.22. Displacement field reconstruction for the airfoil supplemented with displacement data from (a) 0, (b) 2, (c) 10, (d) 18, (e) 34, and (f) 50 SS.

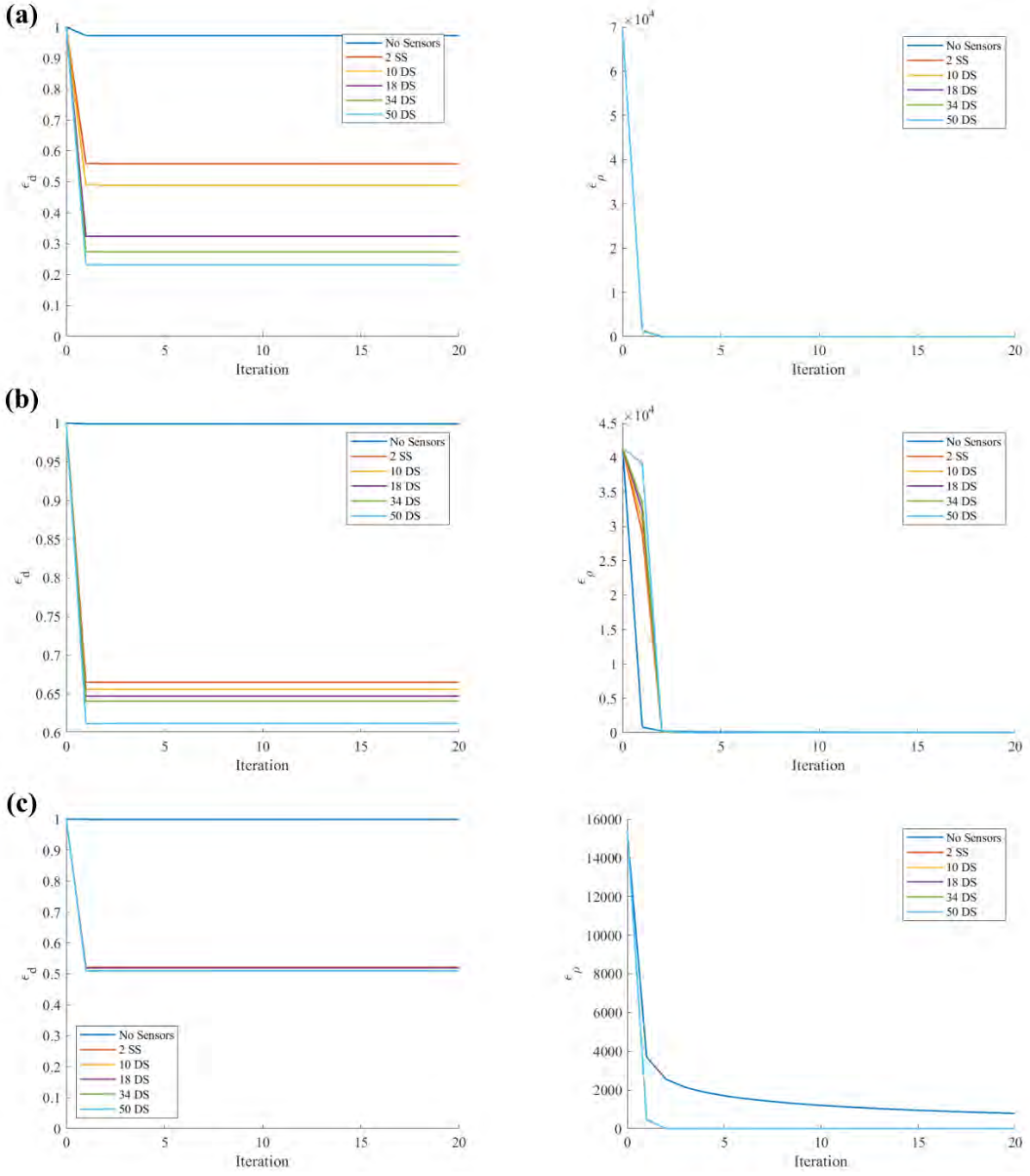

Figure 6.23. Strain data fusion Experiment 1 displacement error (left) and resistivity error (right) plots for the (a) mounting bracket, (b) wing spar, and (c) airfoil.

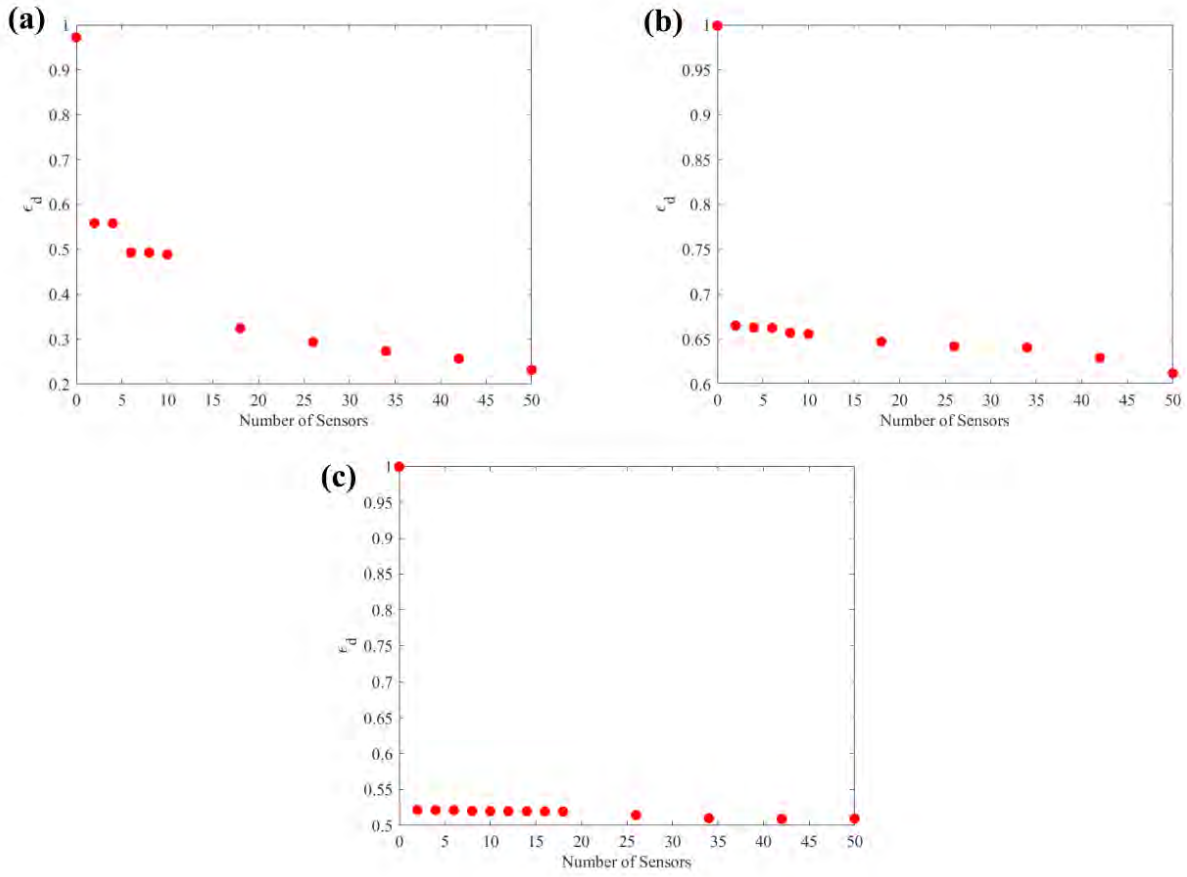

Figure 6.24. Strain data fusion Experiment 1 ϵ_d versus number of sensors plot for the (a) mounting bracket, (b) wing spar, and (c) airfoil.

6.2.2 Experiment 2

Figure 6.25 displays the SS configurations used in this experiment.

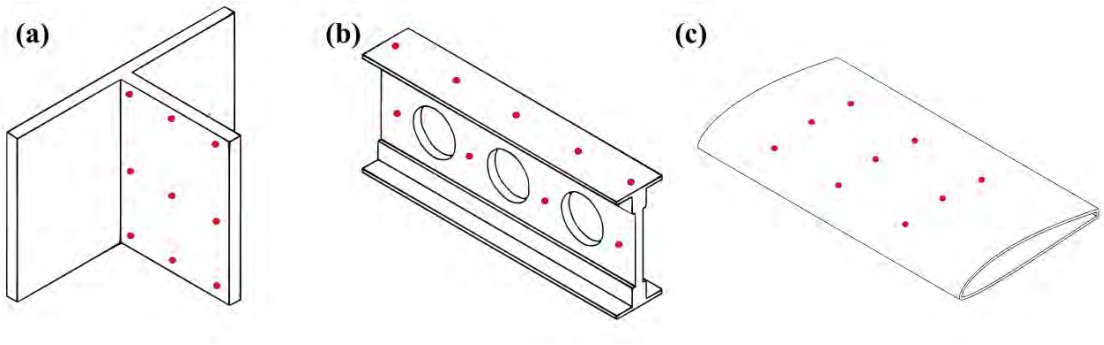

Figure 6.25. SS configurations for Experiment 2 for the (a) mounting bracket, (b) wing spar, and (c) airfoil.

Figures 6.26, 6.27, and 6.28 show the displacement reconstructions for the mounting bracket, wing spar, and airfoil, respectively using resistivity data at 50 dB, 40 dB, and 30 dB SNR. Again, the results for the airfoil at 30 dB SNR are omitted. Visually, the mounting bracket displacement reconstruction further under-predicts the magnitude of the displacement field at 50 dB SNR compared to the 75 dB SNR reconstruction in the previous experiment using the same sensor configuration. For the wing spar and airfoil, the reconstruction is relatively unchanged going from 75 dB to 50 dB SNR. The displacement error and resistivity error plots in figure 6.29 reflect this, with the 50 dB SNR ϵ_d and ϵ_ρ remaining relatively stable and tracking close to the 75 dB SNR case.

The reconstructions for all shapes become very poor at a SNR of 40 dB and below. For the mounting bracket and wing spar, very large displacements were predicted, far beyond the range of the exact solution. For the airfoil, there no displacement magnitude over-prediction, but the shape of the displacement field becomes skewed. For the mounting bracket and wing spar, the displacement error plots show that ϵ_d diverges a small amount at 40 dB SNR and egregiously at 30 dB SNR. In all cases, except for the 30 dB SNR mounting bracket, ϵ_ρ does seem to settle and converge toward zero by the last few iterations, suggesting that the SSIP will eventually find a solution and is not entirely unstable.

Overall, the inclusion of SS does help extract a displacement field reconstruction out of noisy resistivity data. The results showed the reconstructions, while not extremely close to the exact solution, remain around the same quality for resistivity data SNR above 50 dB. However, if the resistivity data SNR falls below 50 dB, reconstructions become largely unreliable.

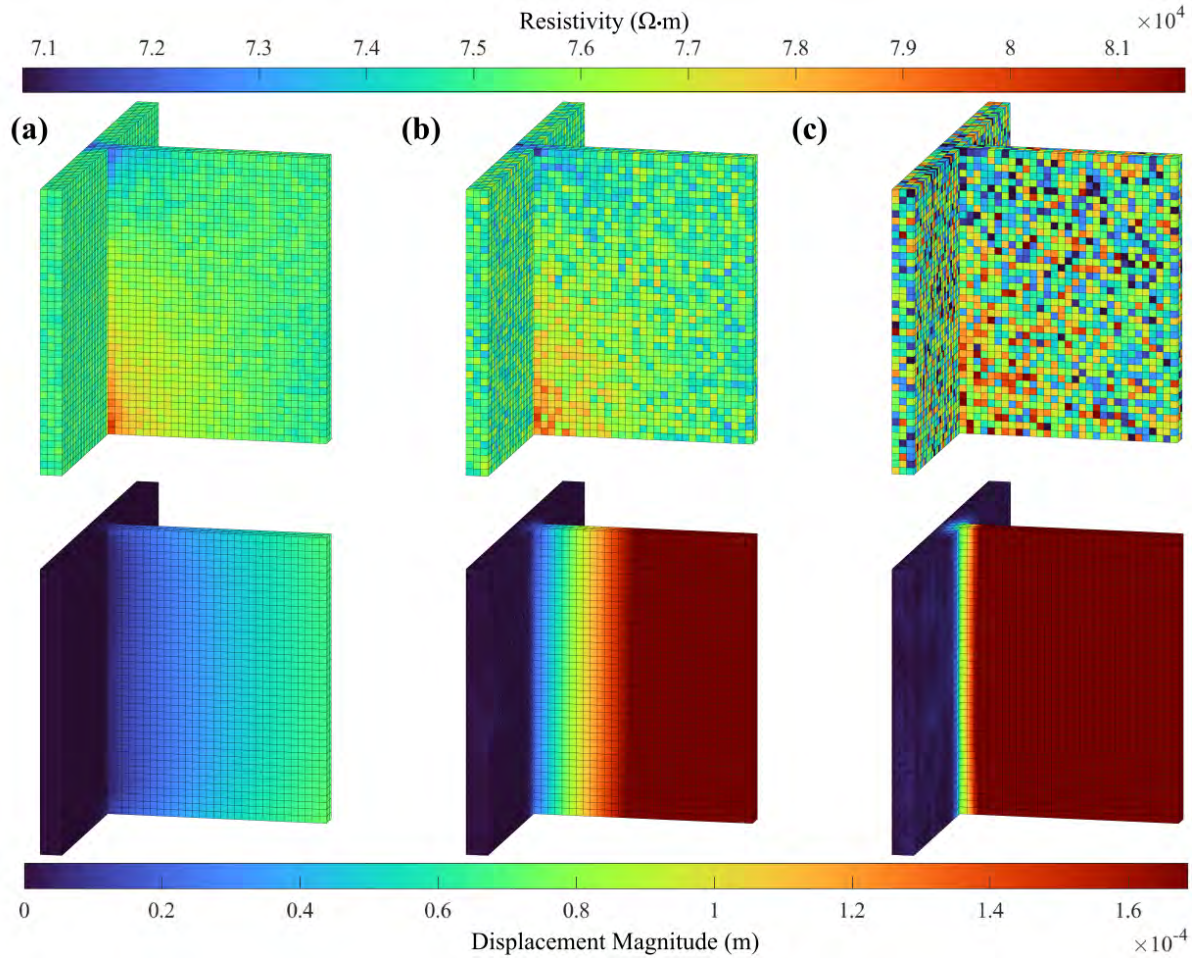

Figure 6.26. From left to right, each column shows the resistivity data (top) and displacement reconstruction (bottom) for (a) 50 dB, (b) 40 dB, and (c) 30 dB SNR for the mounting bracket using 18 SS.

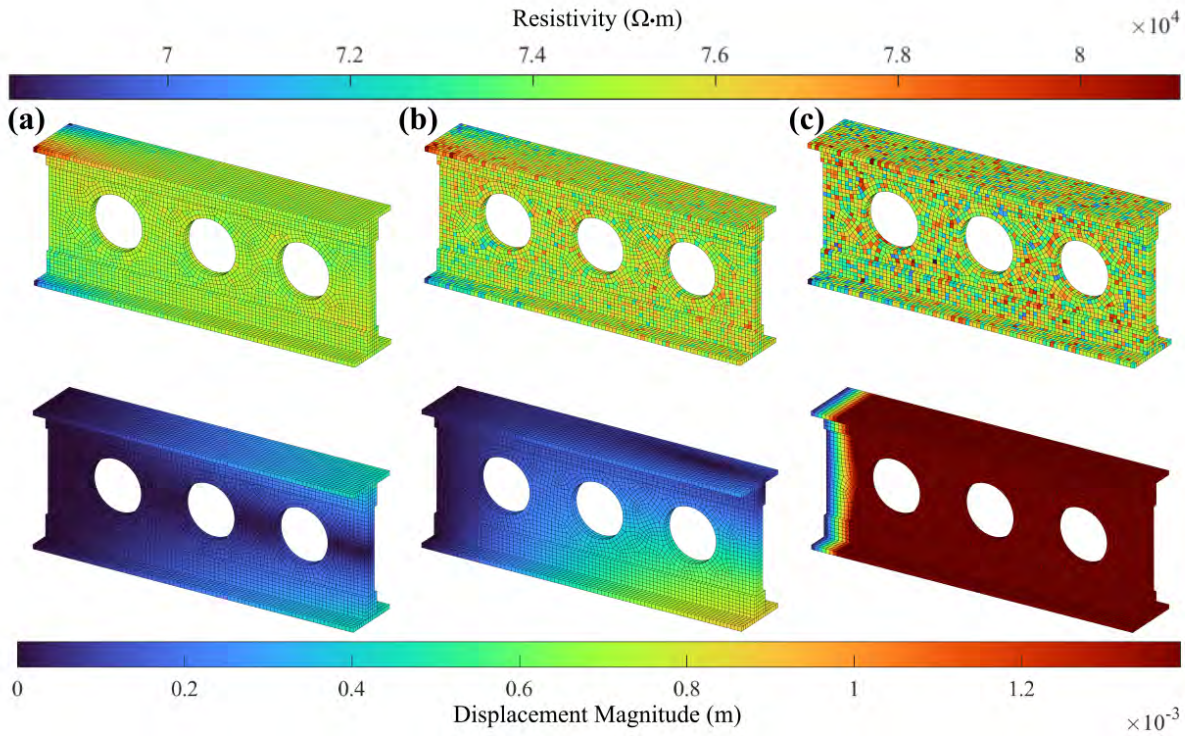

Figure 6.27. From left to right, each column shows the resistivity data (top) and displacement reconstruction (bottom) for (a) 50 dB, (b) 40 dB, and (c) 30 dB SNR for the wing spar using 18 SS.

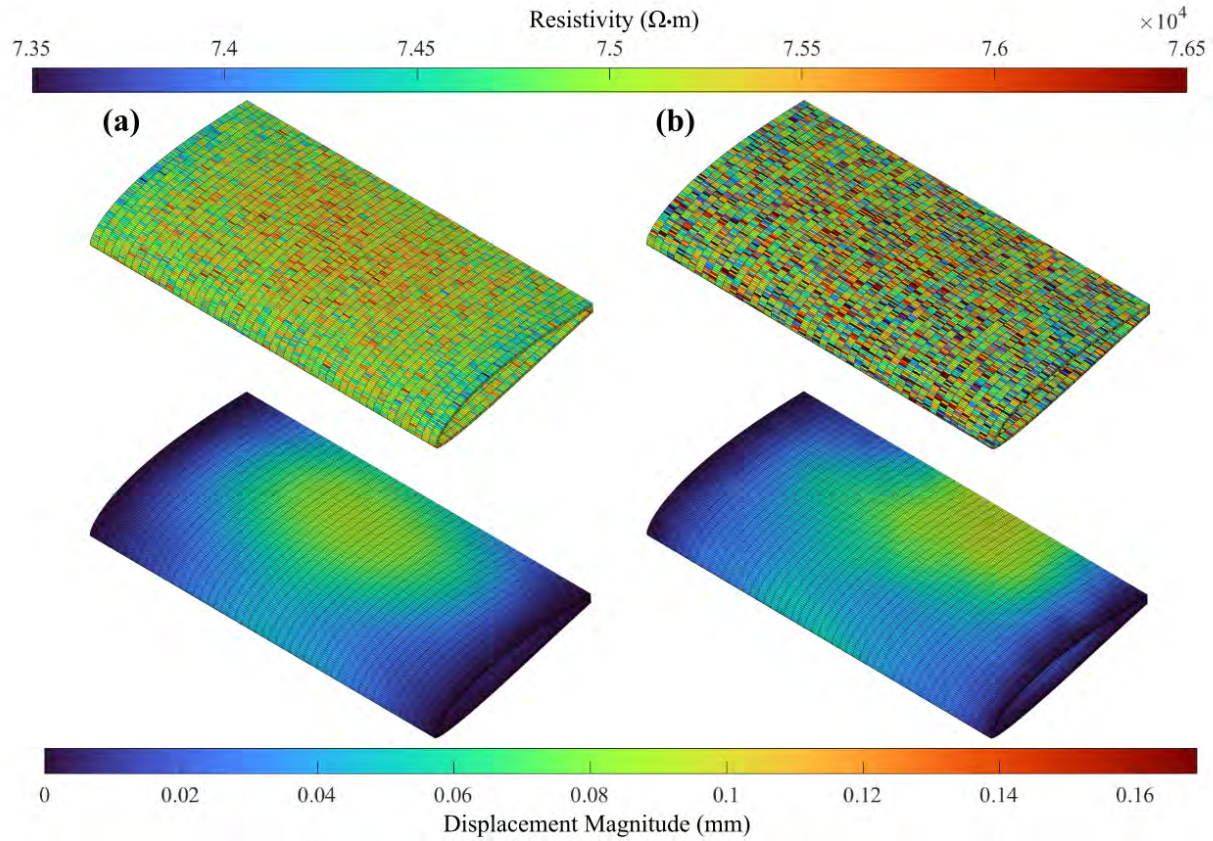

Figure 6.28. From left to right, each column shows the resistivity data (top) and displacement reconstruction (bottom) for (a) 50 dB and (b) 40 dB SNR for the airfoil using 18 SS.

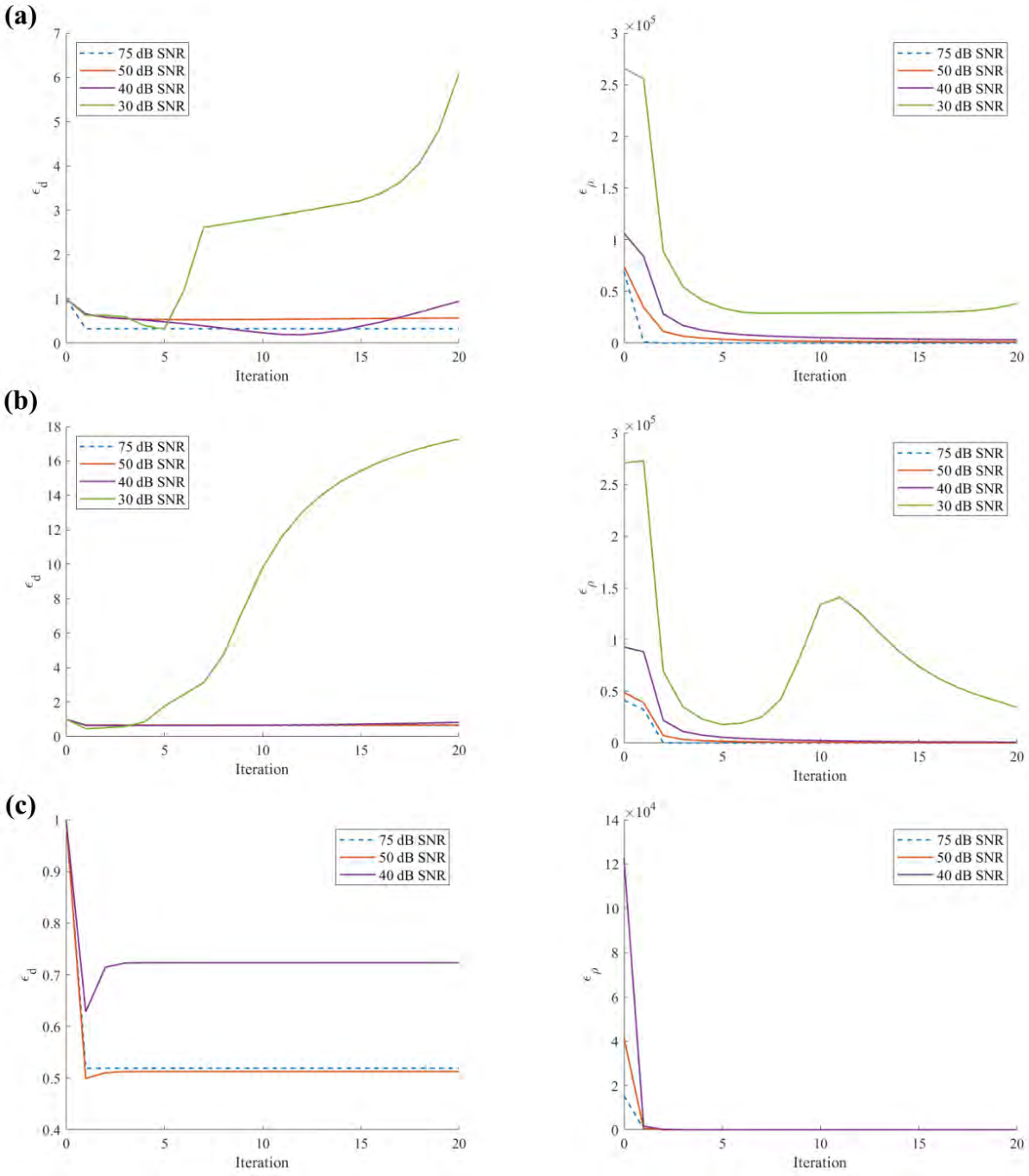

Figure 6.29. Strain data fusion Experiment 2 displacement error (left) and resistivity error (right) plots for the (a) mounting bracket, (b) wing spar, and (c) airfoil.

6.2.3 Experiment 3

The same outlier data used in the DS experiment were used here. Figures 6.30, 6.31, and 6.32 show the sensor configurations used and their corresponding displacement reconstructions for each geometry. All reconstructions were of poor quality, with the displacement magnitude significantly over-predicted and the displacement field fraught with aberrations. Increasing the number of SS decreased the final ϵ_d for all geometries, as seen in the displacement error plots in figure 6.33, but the effect is inconsequential when the final ϵ_d is still several times larger than 1. The resistivity error plots exhibit mildly unstable behavior, but generally converges toward zero in the final few iterations. This again indicates that the SSIP will eventually attain a displacement field solution that satisfies the minimization, even if it is wildly inaccurate.

From the results of this experiment, outlier data renders the SSIP displacement reconstruction inaccurate and unreliable even when enhanced with additional strain data. While adding SS technically improves the quality of the displacement field in such that ϵ_d decreases, the inaccuracies are still far too great. To reiterate, it may be advantageous to explore more outlier robust minimization schemes to counteract the effects of outlier data in conjunction with SDF.

6.2.4 Comparison of Strain Data Fusion to iFEM

Since iFEM is an established methodology that has been proven in literature to be able to accurately recover the displacement field of a deformed shape from discrete strain data, its inclusion in the SSIP raises a keen question. Are the displacement field reconstructions in the strain data fusion results truly the product of the synergistic combination of the SSIP and iFEM, or are the results attainable using iFEM alone?

To answer this question, a displacement field recovery was attempted on each of the three geometries with the 18 SS configuration using iFEM independently. As explained in section 4.3, the formulation of $\boldsymbol{K}$ and $\boldsymbol{F}$ remain unchanged, except the displacement field reconstruction is obtained by solving $\boldsymbol{d} = \boldsymbol{K}^{-1}\boldsymbol{F}$. The iFEM reconstructions are shown in figure 6.34, compared to exact solution and the SSIP strain data fusion Experiment 1 results.

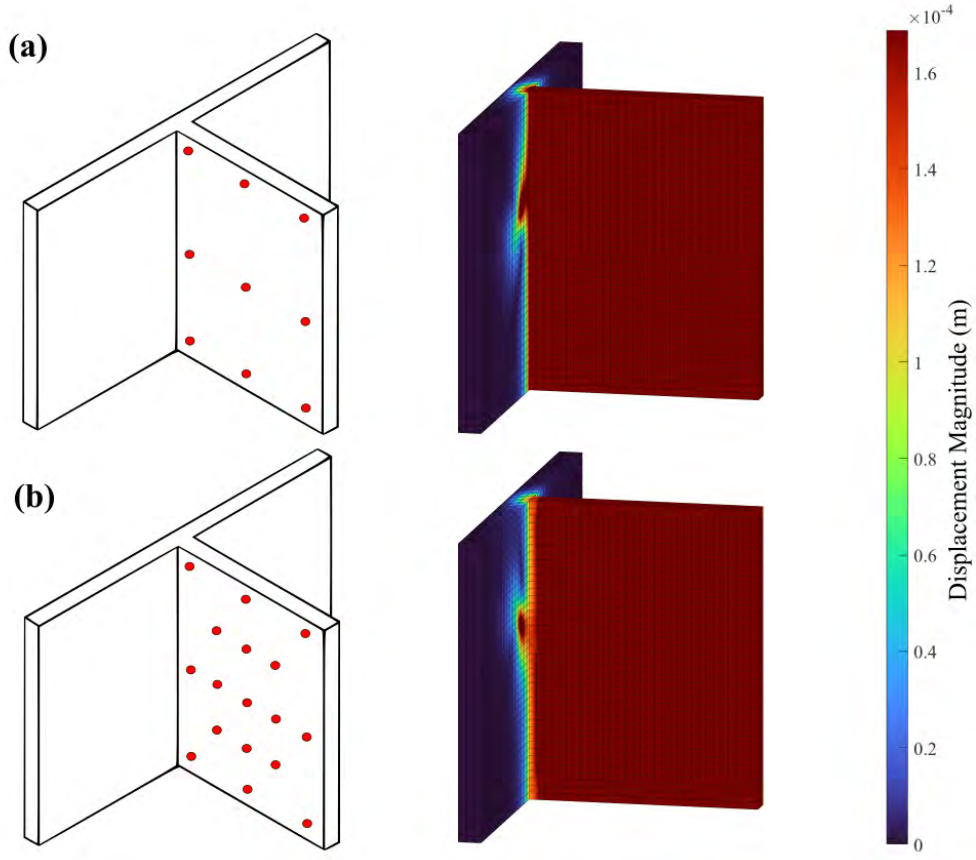

Figure 6.30. Sensor configuration (left) and outlier resistivity data displacement reconstruction (right) for the mounting bracket using (a) 18 SS and (b) 34 SS.

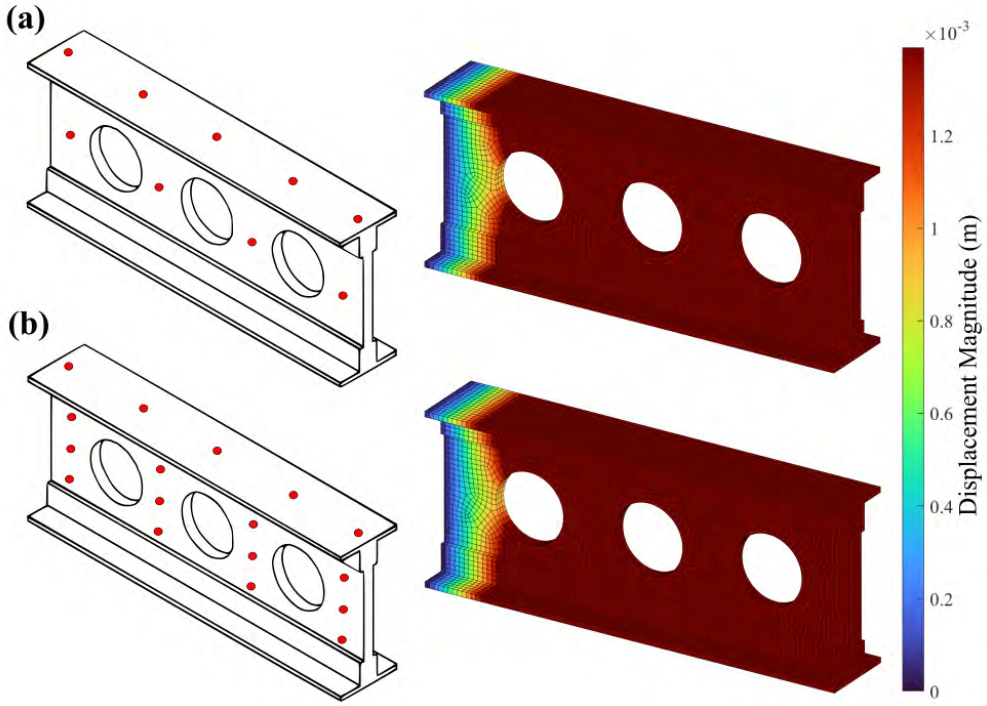

Figure 6.31. Sensor configuration (left) and outlier resistivity data displacement reconstruction (right) for the wing spar using (a) 18 SS and (b) 34 SS.

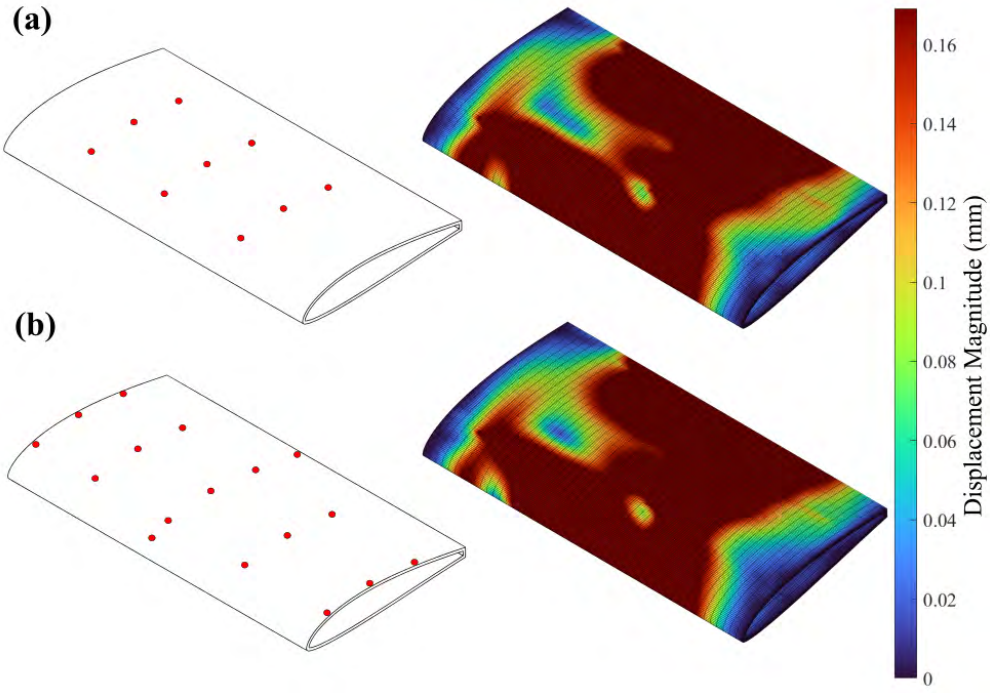

Figure 6.32. Sensor configuration (left) and outlier resistivity data displacement reconstruction (right) for the airfoil using (a) 18 SS and (b) 34 SS.

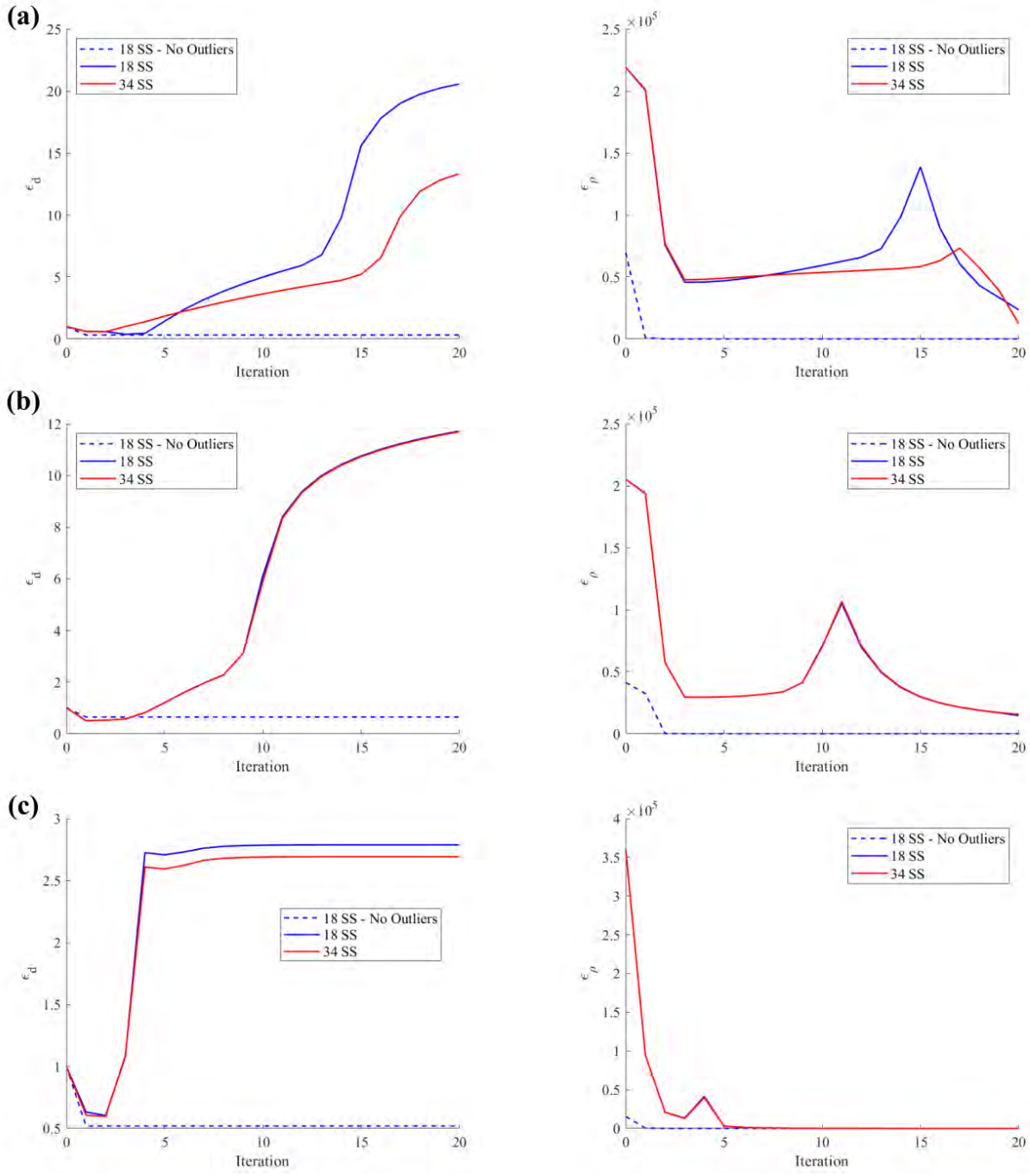

Figure 6.33. Displacement data fusion Experiment 3 displacement error plots (left) and resistivity error plots (right) for the (a) mounting bracket, (b) wing spar, and (c) airfoil.

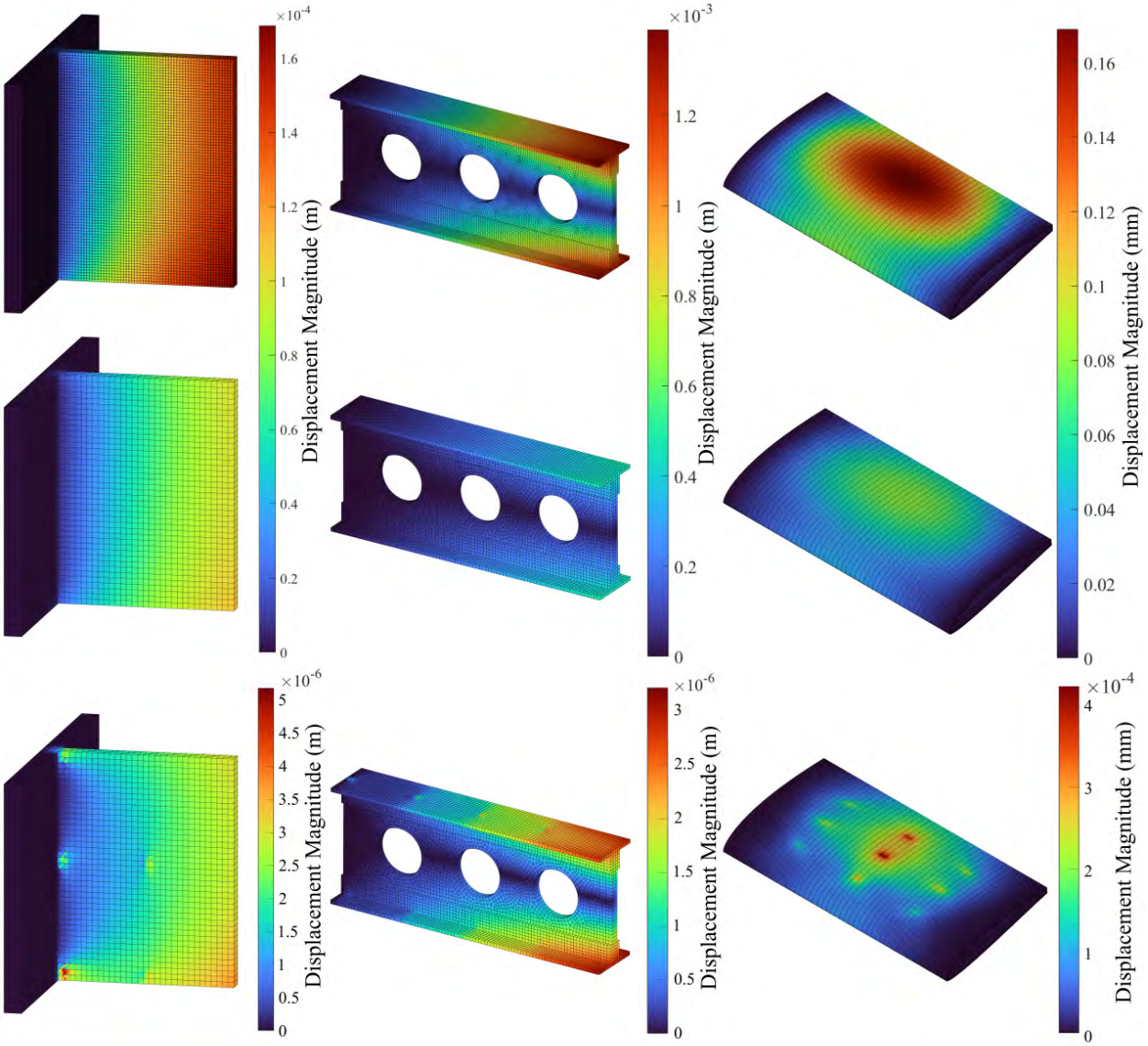

Figure 6.34. Top row: exact displacement field solution, middle row: Experiment 1 SSIP strain SDF displacement field reconstruction using 18 SS, bottom row: iFEM displacement field reconstruction using 18 SS.

Note that a different scale with a much smaller displacement magnitude was used for the iFEM results. Although the iFEM reconstruction roughly captures the shape of the true displacement field, the displacement magnitude is extremely underpredicted, and reconstruction artifacts are plainly visible at SS locations. Recalling the poor quality of the SSIP displacement field reconstruction without any SS, the SSIP strain data fusion reconstructions are an indisputable improvement over the individual use of either method.

6.3 Comparison of Displacement and Strain Data Fusion Results

From the results of Experiment 1, it is clear that the displacement reconstructions enhanced with displacement data outperformed the displacement reconstructions enhanced with strain data. Overall, relatively few DS were required to reconstruct a displacement field close to the exact solution, whereas up to 50 SS were still not able to reconstruct a displacement field as near to the true displacement field. Figure 6.35 plots ϵ_d against the number of sensors for both DS and SS for each shape.

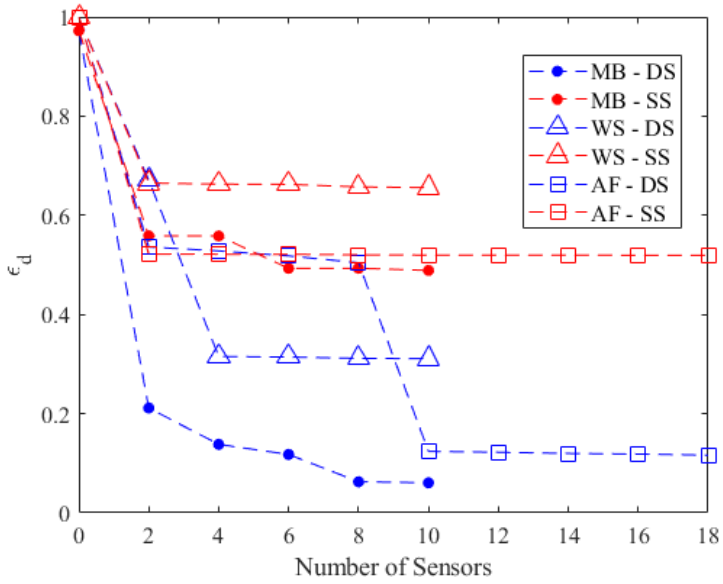

Figure 6.35. Plot of ϵ_d versus number of sensors for each shape using DS and SS.

Displacement data fusion also outperformed strain data fusion in Experiment 2. Using DS, a reasonably accurate displacement field reconstruction was obtained using resistivity

data down to 30 dB SNR for some cases. On the other hand, the quality of reconstructions enhanced with SS was already degraded at 50 dB SNR and became inaccurate below 50 dB SNR. The main reason displacement data fusion possesses an advantage over strain data fusion is because the SSIP directly solves for the displacements. Inserting displacement data directly into $\boldsymbol{d}$ in a sense enforces a displacement boundary condition on the SSIP solution. In contrast, while the strain data fusion method applies additional constraints on the nodal displacements belonging to an SS element, the nodal displacements are not explicitly restricted to a single value as in the displacement data fusion method.

For Experiment 3, reconstructions enhanced with DS also outperformed reconstructions enhanced with SS. However, although the aberrations and reconstruction artifacts were much worse in the resistivity-strain reconstructions, the existence of any outlier induced aberrations, major or minor, already makes the reconstruction equally unreliable. For instance, both the DS and SS reconstructions for the mounting bracket with outlier resistivity data contained significant aberrations. The only reason that the DS reconstruction was considered to be better is because the exact displacement solution was known. Without prior knowledge of the exact solution, there would be no sure way to ascertain that a displacement reconstruction is accurate since ϵ_ρ has been proven to converge toward zero, even in cases with outlier data, given enough iterations. Therefore, to reiterate, if it is known that resistivity data contains outliers, the best approach may be to consider more outlier robust minimization schemes.

7. SUMMARY AND CONCLUSIONS

7.1 Summary

This research endeavored to advance the capabilities of the SSIP by implementing SDF to surmount the mathematical limitations that hinder the accuracy of the SSIP displacement field recovery. This research also expanded the application of the SSIP to more realistic geometries resembling engineering structures and loads, where previous work had focused on relatively simple geometries. By improving the accuracy and reliability of the SSIP displacement field recovery, the long term goal is to one day establish piezoresistive materials as a practical structural material capable of innately providing real-time MSA via the SSIP.

To this end, two SDF methods were formulated to supplement the resistivity data the SSIP utilizes to reconstruct the displacement field of a deformed shape. The first method fused resistivity and discrete displacement data, and the second method fused resistivity and discrete strain data. The efficacy of each method was then demonstrated through a series of computational experiments. The computational experiments aimed to determine the number of sensors providing displacement or strain data required to obtain an accurate displacement field reconstruction, and whether the additional sensor data improved the reliability of the displacement field recovery when the resistivity data contained noise or outlier data.

The results of resistivity-displacement data fusion demonstrated that relatively few sensors were required to tremendously improve the accuracy of the SSIP displacement field reconstruction compared to reconstruction without SDF. The SDF enhanced displacement reconstruction came close to the exact solution simulated by finite element analysis. The inclusion of sensors providing displacement data also made the SSIP more robust to noisy resistivity data, with a reasonably accurate displacement field being reconstructed from resistivity data with 30 dB SNR, in some cases. With regard to outlier data, while a reasonably accurate displacement field was reconstructed for one case, the aberrations and artifacts in the other reconstructed displacement fields caused by outlier data rendered them inaccurate.

The results of resistivity-strain data fusion, while not as auspicious as the resistivity-displacement results, demonstrated similar trends. The inclusion of sensors providing strain data undeniably improved the accuracy of the SSIP recovered displacement field over the

reconstruction without additional sensors, but the degree of improvement was not as pronounced as resistivity-displacement data fusion. In general, increasing the number of strain sensors improved the displacement field recovery accuracy, but while the shape of the displacement field was well captured, the magnitude of the displacements were under-predicted. When the level of resistivity data noise was increased, the strain data enhanced SSIP was able maintain about the same quality displacement reconstruction above 50 dB SNR. Below 50 dB SNR, the displacement field reconstruction quality degraded significantly. When outlier resistivity data were introduced, all reconstructions were entirely unreliable.

7.2 Conclusion

In conclusion, this research shows that SDF is a viable method to improve the accuracy and reliability of the displacement field reconstructed by the SSIP. The bulleted list below highlights the key takeaways from this work. Overall, this study advances the state of the art in extracting useful information about the mechanical state of a piezoresistive material from changes in its electrical properties. This brings piezoresistive materials one step closer toward practical implementation in engineering structures for real-time MSA and condition monitoring.

- In general, SDF of resistivity data with discrete displacement or strain data improves the accuracy of the displacement field reconstructed by the SSIP.
- Employing SDF enables the SSIP to reconstruct the displacement field of complex, realistic geometries, which was not possible without the additional sensor data.
- Fusing resistivity and displacement data allows the SSIP to reconstruct a displacement field close to the true displacement field using relatively few sensors. Increasing the number of sensors generally brings the SSIP displacement reconstruction closer to the exact solution, but there is often a clear point where improvements in accuracy begin to diminish.

- Fusing resistivity and displacement data allows the SSIP to reconstruct a reasonably accurate displacement field from resistivity data with low SNR, in some cases down to 30 dB SNR. However, noise induced reconstruction artifacts intensify at lower SNR.
- Fusing resistivity and displacement data does not guarantee an accurate displacement field reconstruction when there are outliers in the resistivity data, but increasing the number of sensors generally improves the quality of the reconstruction. However, significant aberrations in the reconstruction are likely to persist.
- Fusing resistivity and strain data improves the accuracy of the SSIP displacement field reconstruction. However, while the shape of the displacement field was well captured, the magnitude of the displacement was under-predicted.
- Fusing resistivity and strain data allows the SSIP to maintain roughly the same quality displacement reconstruction for resistivity data SNR above 50 dB.
- Fusing resistivity and strain data does not improve the SSIP displacement field recovery by an appreciable amount when the resistivity data has outliers.
- The SSIP when supplemented with discrete displacement data outperforms the reconstructions supplemented with strain data in terms of displacement field reconstruction accuracy, the number of sensors required for a reasonably accurate displacement, and reliability when resistivity data contains more noise.
- SDF is generally not a reliable approach to deal with resistivity data with outliers.
- The resistivity-strain data fusion method involves adapting an existing displacement reconstruction method known as iFEM. The resistivity-strain data fusion reconstructions are a clear improvement over the use of iFEM independently.

7.3 Outlook for Future Work

While the methods and computational results in this thesis show successful implementation of SDF in the SSIP, these results are preliminary and serve as a foundation for future

exploration of this topic. More research must be performed before the SSIP is ready to be deployed in conjunction with other NDE sensors for real-time condition monitoring of engineering structures. Below are suggestions by the author for future work.

1. The work presented in this thesis was purely computational. Experimental validation of these methods is a clear next step in advancing the SSIP SDF problem.

2. As mentioned several times in this thesis, the quality of the SSIP displacement field reconstruction can depend on sensor location. Studies on sensor location optimization can be explored to develop efficient sensor networks tailored for SSIP displacement field recovery.

3. Outlier resistivity data presented a challenge for the SSIP, even when enhanced with SDF. Future work should explore more outlier-robust formulations, such as the 1-norm error minimization schemes solved via the primal-dual interior point method, in conjunction with SDF.

REFERENCES

[1] A. K. Jardine, D. Lin, and D. Banjevic, "A review on machinery diagnostics and prognostics implementing condition-based maintenance," *Mechanical systems and signal processing*, vol. 20, no. 7, pp. 1483–1510, 2006.

[2] S. Pattabhiraman, C. Gogu, N. H. Kim, R. T. Haftka, and C. Bes, "Skipping unnecessary structural airframe maintenance using an on-board structural health monitoring system," *Proceedings of the Institution of Mechanical Engineers, Part O: Journal of Risk and Reliability*, vol. 226, no. 5, pp. 549–560, 2012.

[3] Y. Li, S. Peng, Y. Li, and W. Jiang, "A review of condition-based maintenance: Its prognostic and operational aspects," *Frontiers of Engineering Management*, vol. 7, no. 3, p. 323, 2020.

[4] E. A. Meyer, Ed., *Proceedings of a Workshop on Materials State Awareness*. Washington, DC: The National Academies Press, 2008.

[5] S. Beard and F.-K. Chang, "Active damage detection in filament wound composite tubes using built-in sensors and actuators," *Journal of Intelligent Material Systems and Structures*, vol. 8, no. 10, pp. 891–897, 1997.

[6] H. Tsuda and J.-R. Lee, "Strain and damage monitoring of cfrp in impact loading using a fiber bragg grating sensor system," *Composites Science and Technology*, vol. 67, no. 7, pp. 1353–1361, 2007.

[7] L. Groo, J. Nasser, D. J. Inman, and H. A. Sodano, "Transfer printed laser induced graphene strain gauges for embedded sensing in fiberglass composites," *Composites Part B: Engineering*, vol. 219, p. 108 932, 2021.

[8] M. Mitra and S. Gopalakrishnan, "Guided wave based structural health monitoring: A review," *Smart Materials and Structures*, vol. 25, no. 5, p. 053 001, 2016.

[9] S. Masmoudi, A. El Mahi, and S. Turki, "Fatigue behaviour and structural health monitoring by acoustic emission of e-glass/epoxy laminates with piezoelectric implant," *Applied Acoustics*, vol. 108, pp. 50–58, 2016.

[10] S. Laflamme and F. Ubertini, "Back-to-basics: Self-sensing materials for nondestructive evaluation," 2019.

[11] "Piezoresistive properties of resin reinforced with carbon nanotubes for health-monitoring of aircraft primary structures," *Composites Part B: Engineering*, vol. 107, pp. 192–202, 2016.

[12] P. Verma, J. Ubaid, K. M. Varadarajan, B. L. Wardle, and S. Kumar, "Synthesis and Characterization of Carbon Nanotube-Doped Thermoplastic Nanocomposites for the Additive Manufacturing of Self-Sensing Piezoresistive Materials," *ACS Applied Materials & Interfaces*, vol. 14, pp. 8361–8372, Feb. 2022.

[13] C. J. Hohimer, G. Petrossian, A. Ameli, C. Mo, and P. Pötschke, "3d printed conductive thermoplastic polyurethane/carbon nanotube composites for capacitive and piezoresistive sensing in soft pneumatic actuators," *Additive Manufacturing*, vol. 34, p. 101 281, Aug. 2020.

[14] Z. Tang, S. Jia, C. Zhou, and B. Li, "3d printing of highly sensitive and large-measurement-range flexible pressure sensors with a positive piezoresistive effect," *ACS applied materials & interfaces*, vol. 12, no. 25, pp. 28 669–28 680, 2020.

[15] P. Costa *et al.*, "Polycarbonate based multifunctional self-sensing 2d and 3d printed structures for aeronautic applications," *Smart Materials and Structures*, vol. 30, no. 8, p. 085 032, Jul. 2021.

[16] K. J. Loh, T.-C. Hou, J. P. Lynch, and N. A. Kotov, "Carbon Nanotube Sensing Skins for Spatial Strain and Impact Damage Identification," *Journal of Nondestructive Evaluation*, vol. 28, pp. 9–25, Mar. 2009.

[17] P. Gruener, Y. Zhao, and M. Schagerl, "Characterization of the spatial elastoresistivity of inkjet-printed carbon nanotube thin films for strain-state sensing," H. F. Wu, A. L. Gyekenyesi, P. J. Shull, and T.-Y. Yu, Eds., Portland, Oregon, United States, Apr. 2017, 101690F.

[18] T. Swait, F. Jones, and S. Hayes, "A practical structural health monitoring system for carbon fibre reinforced composite based on electrical resistance," *Composites Science and Technology*, vol. 72, no. 13, pp. 1515–1523, 2012.

[19] C. Viets, S. Kaysser, and K. Schulte, "Damage mapping of gfrp via electrical resistance measurements using nanocomposite epoxy matrix systems," *Composites Part B: Engineering*, vol. 65, pp. 80–88, Oct. 2014.

[20] A. Naghashpour and S. Van Hoa, "A technique for real-time detecting, locating, and quantifying damage in large polymer composite structures made of carbon fibers and carbon nanotube networks," *Structural Health Monitoring*, vol. 14, no. 1, pp. 35–45, 2015.

[21] F. Azhari and N. Banthia, "Cement-based sensors with carbon fibers and carbon nanotubes for piezoresistive sensing," *Cement and Concrete Composites*, vol. 34, no. 7, pp. 866–873, Aug. 2012.

[22] A. Downey, A. D'Alessandro, S. Laflamme, and F. Ubertini, "Smart bricks for strain sensing and crack detection in masonry structures," *Smart Materials and Structures*, vol. 27, no. 1, p. 015 009, Jan. 2018.

[23] T. N. Tallman and D. J. Smyl, "Structural health and condition monitoring via electrical impedance tomography in self-sensing materials: A review," *Smart Materials and Structures*, vol. 29, no. 12, p. 123 001, Oct. 2020.

[24] R. Harikumar, R. Prabu, and S. Raghavan, "Electrical impedance tomography (eit) and its medical applications: A review," 2013.

[25] B. R. Loyola *et al.*, "Detection of spatially distributed damage in fiber-reinforced polymer composites," *Structural Health Monitoring*, vol. 12, pp. 225–239, May 2013.

[26] T. Tallman, S. Gungor, K. Wang, and C. Bakis, "Tactile imaging and distributed strain sensing in highly flexible carbon nanofiber/polyurethane nanocomposites," *Carbon*, vol. 95, pp. 485–493, Dec. 2015.

[27] A. Baltopoulos, N. Polydorides, L. Pambaguian, A. Vavouliotis, and V. Kostopoulos, "Exploiting carbon nanotube networks for damage assessment of fiber reinforced composites," *Composites Part B: Engineering*, vol. 76, pp. 149–158, Jul. 2015.

[28] H. Dai, G. J. Gallo, T. Schumacher, and E. T. Thostenson, "A Novel Methodology for Spatial Damage Detection and Imaging Using a Distributed Carbon Nanotube-Based Composite Sensor Combined with Electrical Impedance Tomography," *Journal of Nondestructive Evaluation*, vol. 35, no. 2, p. 26, Jun. 2016.

[29] G. J. Gallo and E. T. Thostenson, "Spatial damage detection in electrically anisotropic fiber-reinforced composites using carbon nanotube networks," *Composite Structures*, vol. 141, pp. 14–23, May 2016.

[30] W. Lestari, B. Pinto, V. La Saponara, J. Yasui, and K. J. Loh, "Sensing uniaxial tensile damage in fiber-reinforced polymer composites using electrical resistance tomography," *Smart Materials and Structures*, vol. 25, no. 8, p. 085 016, Jul. 2016.

[31] S. Nonn, M. Schagerl, Y. Zhao, S. Gschossmann, and C. Kralovec, "Application of electrical impedance tomography to an anisotropic carbon fiber-reinforced polymer composite laminate for damage localization," *Composites Science and Technology*, vol. 160, pp. 231–236, May 2018.

[32] A. Thomas, J. Kim, T. Tallman, and C. Bakis, "Damage detection in self-sensing composite tubes via electrical impedance tomography," *Composites Part B: Engineering*, vol. 177, p. 107 276, Nov. 2019.

[33] M. Sannamani, J. Gao, W. W. Chen, and T. N. Tallman, "Damage detection in non-planar carbon fiber-reinforced polymer laminates via electrical impedance tomography with surface-mounted electrodes and directional sensitivity matrices," *Composites Science and Technology*, vol. 224, Jun. 2022.

[34] L. Homa, M. Sannamani, A. J. Thomas, T. N. Tallman, and J. Wertz, "Enhanced damage imaging in three-dimensional composite structures via electrical impedance tomography with mixed and level set regularization," *NDT & E International*, vol. 137, p. 102 830, Jul. 2023.

[35] T.-C. Hou, K. J. Loh, and J. P. Lynch, "Spatial conductivity mapping of carbon nanotube composite thin films by electrical impedance tomography for sensing applications," *Nanotechnology*, vol. 18, p. 315 501, Aug. 2007.

[36] T.-C. Hou and J. P. Lynch, "Electrical Impedance Tomographic Methods for Sensing Strain Fields and Crack Damage in Cementitious Structures," *Journal of Intelligent Material Systems and Structures*, vol. 20, no. 11, pp. 1363–1379, Jul. 2009. (visited on 01/31/2025).

[37] K. Karhunen, A. Seppänen, A. Lehikoinen, P. J. Monteiro, and J. P. Kaipio, "Electrical resistance tomography imaging of concrete," *Cement and Concrete Research*, vol. 40, no. 1, pp. 137–145, 2010.

[38] M. Hallaji and M. Pour-Ghaz, "A new sensing skin for qualitative damage detection in concrete elements: Rapid difference imaging with electrical resistance tomography," *NDT & E International*, vol. 68, pp. 13–21, Dec. 2014.

[39] M. Hallaji, A. Seppänen, and M. Pour-Ghaz, "Electrical resistance tomography to monitor unsaturated moisture flow in cementitious materials," *Cement and Concrete Research*, vol. 69, pp. 10–18, Mar. 2015.

[40] D. Smyl, R. Rashetnia, A. Seppänen, and M. Pour-Ghaz, "Can Electrical Resistance Tomography be used for imaging unsaturated moisture flow in cement-based materials with discrete cracks?" *Cement and Concrete Research*, vol. 91, pp. 61–72, Jan. 2017.

[41] D. Smyl, M. Pour-Ghaz, and A. Seppänen, "Detection and reconstruction of complex structural cracking patterns with electrical imaging," *NDT & E International*, vol. 99, pp. 123–133, Oct. 2018.

[42] T. N. Tallman and K. W. Wang, "An inverse methodology for calculating strains from conductivity changes in piezoresistive nanocomposites," *Smart Materials and Structures*, vol. 25, no. 11, p. 115 046, Nov. 2016.

[43] T. Tallman, S. Gungor, G. Koo, and C. Bakis, "On the inverse determination of displacements, strains, and stresses in a carbon nanofiber/polyurethane nanocomposite from conductivity data obtained via electrical impedance tomography," *Journal of Intelligent Material Systems and Structures*, vol. 28, no. 18, pp. 2617–2629, Nov. 2017.

[44] H. Hassan and T. N. Tallman, "Failure prediction in self-sensing nanocomposites via genetic algorithm-enabled piezoresistive inversion," *Structural Health Monitoring*, vol. 19, no. 3, pp. 765–780, May 2020.

[45] H. Hassan and T. N. Tallman, "A comparison of metaheuristic algorithms for solving the piezoresistive inverse problem in self-sensing materials," *IEEE Sensors Journal*, vol. 21, no. 1, pp. 659–666, 2020.

[46] H. Hassan, W. A. Crossley, and T. N. Tallman, "Hybrid optimization schemes for solving the piezoresistive inversion problem in self-sensing materials," *Smart Materials and Structures*, vol. 33, p. 065 033, Jun. 2024.

[47] D. Hall and J. Llinas, "An introduction to multisensor data fusion," *Proceedings of the IEEE*, vol. 85, no. 1, pp. 6–23, 1997.

[48] F. E. White, "Data Fusion Lexicon," OSD or Non-Service DoD Agency, Fort Belvoir, VA, Tech. Rep., Oct. 1991.

[49] Y. Wu, E. Blasch, G. Chen, L. Bai, and H. Ling, "Multiple source data fusion via sparse representation for robust visual tracking," in *14th International Conference on Information Fusion*, IEEE, 2011, pp. 1–8.

[50] E. Blasch, "Context aided sensor and human-based information fusion," in *NAECON 2014 - IEEE National Aerospace and Electronics Conference*, Dayton, OH, USA: IEEE, Jun. 2014, pp. 127–134.

[51] E. Blasch *et al.*, "Context aided video-to-text information fusion," in *17th International Conference on Information Fusion (FUSION)*, IEEE, 2014, pp. 1–8.

[52] Z. Liu, D. S. Forsyth, J. P. Komorowski, K. Hanasaki, and T. Kirubarajan, "Survey: State of the Art in NDE Data Fusion Techniques," *IEEE Transactions on Instrumentation and Measurement*, vol. 56, no. 6, pp. 2435–2451, Dec. 2007.

[53] R.-T. Wu and M. R. Jahanshahi, "Data fusion approaches for structural health monitoring and system identification: Past, present, and future," *Structural Health Monitoring*, vol. 19, no. 2, pp. 552–586, Mar. 2020.

[54] W. Nsengiyumva, S. Zhong, M. Luo, Q. Zhang, and J. Lin, "Critical insights into the state-of-the-art nde data fusion techniques for the inspection of structural systems," *Structural Control and Health Monitoring*, vol. 29, no. 1, e2857, 2022.

[55] X. E. Gros, *Applications of NDT data fusion*. Springer, 2001.

[56] D. Horn and W. Mayo, "Nde reliability gains from combining eddy-current and ultrasonic testing," *NDT & E International - NDT E INT*, vol. 33, pp. 351–362, Sep. 2000.

[57] J. Moysan, A. Durocher, C. Gueudré, and G. Corneloup, "Improvement of the non-destructive evaluation of plasma facing components by data combination of infrared thermal images," *NDT & E International*, vol. 40, no. 6, pp. 478–485, Sep. 2007.

[58] M.-A. Ploix, V. Garnier, D. Breysse, and J. Moysan, "NDE data fusion to improve the evaluation of concrete structures," *NDT & E International*, vol. 44, no. 5, pp. 442–448, Sep. 2011.

[59] D. Zonta *et al.*, "Sensor Fusion on Structural Monitoring Data Analysis: Application to a Cable-Stayed Bridge," *Key Engineering Materials*, vol. 569-570, pp. 812–819, Jul. 2013.

[60] P. J. Dempsey and S. Sheng, "Investigation of data fusion applied to health monitoring of wind turbine drivetrain components," *Wind Energy*, vol. 16, no. 4, pp. 479–489, 2013.

[61] P. Lopato, G. Psuj, and B. Szymanik, "Nondestructive Inspection of Thin Basalt Fiber Reinforced Composites Using Combined Terahertz Imaging and Infrared Thermography," *Advances in Materials Science and Engineering*, vol. 2016, pp. 1–13, 2016.

[62] S.-S. Jin, S. T. Kim, and Y.-H. Park, "Combining point and distributed strain sensor for complementary data-fusion: A multi-fidelity approach," *Mechanical Systems and Signal Processing*, vol. 157, p. 107 725, Aug. 2021.

[63] A. Hauptmann and D. Smyl, "Fusing electrical and elasticity imaging," *Philosophical Transactions of the Royal Society A: Mathematical, Physical and Engineering Sciences*, vol. 379, p. 20 200 194, Jun. 2021.

[64] J. Wertz, L. Homa, M. Cherry, S. O'Rourke, C. Flournoy, and E. Blasch, "A novel method for segmentation of titanium microtexture regions via sensor data fusion," *Materials Characterization*, vol. 210, p. 113 770, 2024.

[65] R. Heideklang and P. Shokouhi, "Multi-sensor image fusion at signal level for improved near-surface crack detection," *NDT & E International*, vol. 71, pp. 16–22, Apr. 2015.

[66] S. Pashoutani, J. Zhu, C. Sim, K. Won, B. A. Mazzeo, and W. S. Guthrie, "Multi-sensor data collection and fusion using autoencoders in condition evaluation of concrete bridge decks," *Journal of Infrastructure Preservation and Resilience*, vol. 2, pp. 1–12, 2021.

[67] A. Gallet *et al.*, "Structural engineering from an inverse problems perspective.," *Proceedings. Mathematical, Physical, and Engineering Sciences*, vol. 478, no. 2257, pp. 20 210 526–20 210 526, 2022.

[68] M. Taya, W. Kim, and K. Ono, "Piezoresistivity of a short fiber/elastomer matrix composite," *Mechanics of Materials*, vol. 28, no. 1, pp. 53–59, 1998.

[69] N. Hu, Z. Masuda, G. Yamamoto, H. Fukunaga, T. Hashida, and J. Qiu, "Effect of fabrication process on electrical properties of polymer/multi-wall carbon nanotube nanocomposites," *Composites Part A: Applied Science and Manufacturing*, vol. 39, no. 5, pp. 893–903, 2008.

[70] R. Rahman and P. Servati, "Effects of inter-tube distance and alignment on tunnelling resistance and strain sensitivity of nanotube/polymer composite films," *Nanotechnology*, vol. 23, no. 5, p. 055 703, Jan. 2012.

[71] B. M. Lee and K. J. Loh, "A 2D percolation-based model for characterizing the piezoresistivity of carbon nanotube-based films," en, *Journal of Materials Science*, vol. 50, no. 7, pp. 2973–2983, Apr. 2015.

[72] A. Oliva-Avilés, F. Avilés, G. Seidel, and V. Sosa, "On the contribution of carbon nanotube deformation to piezoresistivity of carbon nanotube/polymer composites," *Composites Part B: Engineering*, vol. 47, pp. 200–206, 2013.

[73] A. K. Chaurasia, X. Ren, and G. D. Seidel, "Computational micromechanics analysis of electron hopping and interfacial damage induced piezoresistive response in carbon nanotube-polymer nanocomposites," *Smart Materials and Structures*, vol. 23, no. 7, p. 075 023, Jun. 2014.

[74] X. Ren, A. K. Chaurasia, A. I. Oliva-Avilés, J. J. Ku-Herrera, G. D. Seidel, and F. Avilés, "Modeling of mesoscale dispersion effect on the piezoresistivity of carbon nanotube-polymer nanocomposites via 3d computational multiscale micromechanics methods," *Smart Materials and Structures*, vol. 24, no. 6, p. 065 031, May 2015.

[75] A. Alian and S. Meguid, "Multiscale modeling of the coupled electromechanical behavior of multifunctional nanocomposites," *Composite Structures*, vol. 208, pp. 826–835, 2019.

[76] F. Deng and Q.-S. Zheng, "An analytical model of effective electrical conductivity of carbon nanotube composites," *Applied Physics Letters*, vol. 92, no. 7, p. 071 902, Feb. 2008.

[77] T. Takeda, Y. Shindo, Y. Kuronuma, and F. Narita, "Modeling and characterization of the electrical conductivity of carbon nanotube-based polymer composites," *Polymer*, vol. 52, no. 17, pp. 3852–3856, Aug. 2011.

[78] T. Tallman and K. Wang, "An arbitrary strains carbon nanotube composite piezoresistivity model for finite element integration," *Applied Physics Letters*, vol. 102, no. 1, 2013.

[79] F. Panozzo, M. Zappalorto, and M. Quaresimin, "Analytical model for the prediction of the piezoresistive behavior of cnt modified polymers," *Composites Part B: Engineering*, vol. 109, pp. 53–63, 2017.

[80] G. Koo and T. Tallman, "Higher-order resistivity-strain relations for self-sensing nanocomposites subject to general deformations," *Composites Part B: Engineering*, vol. 190, p. 107 907, Jun. 2020.

[81] D. Holder and Institute of Physics (Great Britain), Eds., *Electrical impedance tomography: methods, history, and applications* (Series in medical physics and biomedical engineering). Institute of Physics Pub, 2005.

[82] A. N. Steinberg, C. L. Bowman, and F. E. White, "Revisions to the JDL data fusion model," in *Sensor Fusion: Architectures, Algorithms, and Applications III*, B. V. Dasarathy, Ed., International Society for Optics and Photonics, vol. 3719, SPIE, 1999, pp. 430–441.

[83] Z. Ma, J. Choi, and H. Sohn, "Structural displacement sensing techniques for civil infrastructure: A review," *Journal of Infrastructure Intelligence and Resilience*, vol. 2, no. 3, p. 100 041, 2023.

[84] E. Hinton and J. S. Campbell, "Local and global smoothing of discontinuous finite element functions using a least squares method," *International Journal for Numerical Methods in Engineering*, vol. 8, no. 3, pp. 461–480, 1974.

[85] A. Tessler, *A variational principle for reconstruction of elastic deformations in shear deformable plates and shells*. National Aeronautics and Space Administration, Langley Research Center, 2003.

[86] A. Tessler and J. L. Spangler, "Inverse fem for full-field reconstruction of elastic deformations in shear deformable plates and shells," in *2nd European workshop on structural health monitoring*, 2004.

[87] A. Tessler, J. L. Spangler, M. Gherlone, M. Mattone, and M. Di Sciuva, "Real-time characterization of aerospace structures using onboard strain measurement technologies and inverse finite element method," in *Proceedings of the 8th international workshop on structural health monitoring*, Stanford Univ Stanford, CA, vol. 2, 2011, pp. 981–989.

[88] D. Poloni, D. Oboe, C. Sbarufatti, and M. Giglio, "Towards a stochastic inverse finite element method: A gaussian process strain extrapolation," *Mechanical Systems and Signal Processing*, vol. 189, p. 110 056, 2023.

[89] D. Oboe, C. Sbarufatti, and M. Giglio, "Physics-based strain pre-extrapolation technique for inverse finite element method," *Mechanical Systems and Signal Processing*, vol. 177, p. 109 167, Sep. 2022.

[90] M. Drela, "XFOIL: An Analysis and Design System for Low Reynolds Number Airfoils," in *Low Reynolds Number Aerodynamics*, T. J. Mueller, Ed., Berlin, Heidelberg: Springer Berlin Heidelberg, 1989, pp. 1–12.

[91] G.M.Koo, "On the development of macroscale modeling strategies for ac/dc transport-deformation coupling in self-sensing piezoresistive materials," PhD thesis, Purdue University, School of Aeronautics and Astronautics, 2020.

A. ADDITIONAL STRAIN DATA FUSION METHODS

This appendix will elaborate upon the strain SDF methods discussed in section 4.3 that were not selected for further investigation in this thesis. The following will present a detailed mathematical formulation of these methods as well as their displacement reconstruction results.

A.1 Mathematical Formulation

In section 4.3, two resistivity-strain data fusion methods were briefly discussed that were not selected for further investigation. The first involved augmenting the SSIP $\boldsymbol{G}$ matrix, and the second involved reformulating the SSIP as a constrained least squares problem and applying known strain data as linear constraints. These methods are hereon referred to as the 'G Augmentation' and 'Linear Equality Constraint' (LEC) methods, respectively. The strain SDF method chosen in the thesis is referred to as the 'SSIP-iFEM' method. What follows is a detailed mathematical formulation of the G Augmentation and LEC methods.

To reiterate, the resistivity-strain data fusion methods in this thesis are predicated on incorporating strain-displacement relations to constrain the SSIP. Recall that the SSIP has been adapted to be applicable to a finite element mesh. Thus, the strain-displacement relations are expressed in matrix form in equation (4.9) for a single hexahedral element, denoted as B_e. B_e is simply a mapping of the element nodal displacements to each unique strain component defined by equation (4.7). However, both the G Augmentation and LEC methods treat strain as a nodal quantity because strain gauges, in practice, measure strains at a point, whereas finite element analysis typically treats strains as an elemental value. Therefore, a method is required to project the elemental strains to the nodes.

The L_2 projection is method that can project the values of an arbitrary function with values known at the Gaussian integration points of a finite element mesh to the mesh's nodes [84]. The projection is performed by solving the matrix equation (A.1) for Ψ, where $\boldsymbol{M}$ is known as the mass matrix, Ψ is the global vector of projected nodal values, and Θ is known as the L_2 projection forcing vector. In the context of projected strains, Ψ are the nodal projected strains, and Θ contains the strains known at the integration points. $\boldsymbol{M}$ is a

symmetric matrix with the number of rows and columns equal to the total number of nodes in the mesh. For dimensional compatibility, the length of Θ must also equal the total number of nodes. Therefore, the integration point rule used must yield the same total number of integration points as there are nodes in the mesh. Thus, in this work, a $2 \times 2 \times 2$ integration point rule for three-dimensional hexahedral elements was used.

$$\boldsymbol{M\Psi} = \boldsymbol{\Theta} \tag{A.1}$$

$\boldsymbol{M}$ and $\boldsymbol{\Theta}$ are assembled from elemental matrices and vectors. Equation (A.2) defines equation (A.1) for a single mesh element. In the equation below, M_e is the elemental mass matrix, ψ_e are the projected nodal strains for a single element, and θ_e is the elemental forcing vector. For three-dimensional hexahedral elements, M_e and θ_e are formulated using equations (A.3) and (A.4), respectively, where N^A are the trilinear interpolation functions, defined in equation (3.11), and ε_e^N is the value of the strain component at the Nth integration point of the eth element. The triple integrals are being performed over the volume of the iso-parametric hexahedral element. The superscript A and B represent the node number, while the superscript N represents the integration point number. For hexahedral elements using a $2 \times 2 \times 2$ integration point rule, A, B, and N all run from 1 to 8. ε must be a constant because, generally, for the L_2 projection, the values defined at the integration points must be constants.

$$M_\mathrm{e}\psi_\mathrm{e} = \theta_\mathrm{e} \tag{A.2}$$

$$M_\mathrm{e} = \iiint_{V_\xi} N^A N^B |det\boldsymbol{J}| d\xi_1 d\xi_2 d\xi_3 = \begin{bmatrix} \iiint N^1 N^1 |det\boldsymbol{J}| dV_\xi & \cdots & \iiint N^1 N^8 |det\boldsymbol{J}| dV_\xi \\ \vdots & \ddots & \vdots \\ \iiint N^8 N^1 |det\boldsymbol{J}| dV_\xi & \cdots & \iiint N^8 N^8 |det\boldsymbol{J}| dV_\xi \end{bmatrix} \tag{A.3}$$

$$\theta_{\mathrm{e}} = \iiint_{V_\xi} N^N \varepsilon_{\mathrm{e}}^N |det\boldsymbol{J}| d\xi_1 d\xi_2 d\xi_3 = \begin{bmatrix} \iiint N^1 \varepsilon_{\mathrm{e}}^1 |det\boldsymbol{J}| dV_\xi \\ \vdots \\ \iiint N^8 \varepsilon_{\mathrm{e}}^8 |det\boldsymbol{J}| dV_\xi \end{bmatrix} \tag{A.4}$$

The next step is to express ε_{e} in equation (A.4) in terms of strain-displacement relations. This can be done via equation (A.5). However, as mentioned earlier, $\varepsilon_{\mathrm{e}}^N$ needs to be a constant, but equation (A.5) calculates a vector, with each vector component corresponding to a different strain component.

$$\varepsilon_{\mathrm{e}} = B_{\mathrm{e}} d_{\mathrm{e,i}} \tag{A.5}$$

To surmount this problem, B_{e} is split into six row vectors, with each vector mapping the nodal displacements to one strain component. These row vectors are denoted by $B_{\mathrm{e}}^{\varepsilon_{\mathrm{ij}}}$. For instance, the strain-displacement vector mapping the nodal displacements to the strain component ε_{11} would be denoted as $B_{\mathrm{e}}^{\varepsilon_{11}}$. $B_{\mathrm{e}}^{\varepsilon_{11}}$ consists of the first row of B_{e}. The product of $B_{\mathrm{e}}^{\varepsilon_{11}}$ and $d_{\mathrm{e,i}}$ results in a constant ε_{11} for each integration point, making it compatible for substitution into equation (A.4). Proceeding with the formulation, now just considering the projection of ε_{11}, equation (A.4) becomes equation (A.6). In the second line of equation (A.6), $d_{\mathrm{e,i}}$ is removed from the integrand because the nodal displacements are constants and independent from the integral. Additionally, by combining N^N with $B_{\mathrm{e}}^{\varepsilon_{11}}$, the integrand becomes a matrix, which is more succinctly expressed as $C_{\mathrm{e}}^{\varepsilon_{11}}$. $C_{\mathrm{e}}^{\varepsilon_{11}}$ is explicitly defined in equation (A.7).

$$\begin{aligned} \theta_{\mathrm{e}} &= \iiint_{V_\xi} N^N (B_{\mathrm{e}}^{\varepsilon_{11}} d_{\mathrm{e,i}}) |det\boldsymbol{J}| d\xi_1 d\xi_2 d\xi_3 \\ &= \left[\iiint_{V_\xi} N^N B_{\mathrm{e}}^{\varepsilon_{11}} |det\boldsymbol{J}| d\xi_1 d\xi_2 d\xi_3 \right] d_{\mathrm{e,i}} \\ &= C_{\mathrm{e}}^{\varepsilon_{11}} d_{\mathrm{e,i}} \end{aligned} \tag{A.6}$$

$$C_{\mathrm{e}}^{\varepsilon_{11}} = \iiint_{V_\xi} \begin{bmatrix} N^1\frac{\partial N^1}{\partial x_1} & 0 & 0 & N^1\frac{\partial N^2}{\partial x_1} & 0 & 0 & \cdots & N^1\frac{\partial N^8}{\partial x_1} & 0 & 0 \\ \vdots & \vdots & \vdots & \vdots & \vdots & \vdots & \ddots & \vdots & \vdots & \vdots \\ N^8\frac{\partial N^1}{\partial x_1} & 0 & 0 & N^8\frac{\partial N^2}{\partial x_1} & 0 & 0 & \cdots & N^8\frac{\partial N^8}{\partial x_1} & 0 & 0 \end{bmatrix} |det\boldsymbol{J}| dV_\xi \tag{A.7}$$

Next, the elemental $C_{\mathrm{e}}^{\varepsilon_{11}}$ and $d_{\mathrm{e,i}}$ matrices and vectors are assembled into a global matrix and vector encompassing the entire finite element mesh. Thus, $\boldsymbol{\Theta}$ can be expressed as equation (A.8).

$$\boldsymbol{\Theta}^{\varepsilon_{11}} = \boldsymbol{C}^{\varepsilon_{11}}\boldsymbol{d} \tag{A.8}$$

By substituting equation (A.8) into equation (A.1) and solving for $\boldsymbol{\Psi}$, equation (A.9) is obtained. In the equation below, $\Psi^{\varepsilon_{11}}$ are the ε_{11} strains at the nodes of the finite element mesh. Therefore, to fully formulate the nodal strain-displacement relations, solving five additional matrix equations for each remaining strain component are necessary.

$$\boldsymbol{\Psi}^{\varepsilon_{11}} = \boldsymbol{M}^{-1}\boldsymbol{C}^{\varepsilon_{11}}\boldsymbol{d} \tag{A.9}$$

To incorporate equation (A.9) into the SSIP, $\boldsymbol{d}$ and $\boldsymbol{\Psi}^{\boldsymbol{\varepsilon_{11}}}$ are converted to $\delta\boldsymbol{d}$ and $\delta\boldsymbol{\Psi}^{\boldsymbol{\varepsilon_{11}}}$, respectively. $\delta\boldsymbol{d}$ is the difference between the true and SSIP predicted displacement field, and $\delta\boldsymbol{\Psi}^{\boldsymbol{\varepsilon_{11}}}$ is the difference between the measured and SSIP predicted ε_{11}. Thus, equation (A.9) is recast as equation (A.10).

$$\delta\boldsymbol{\Psi}^{\varepsilon_{11}} = \boldsymbol{M}^{-1}\boldsymbol{C}^{\varepsilon_{11}}\delta\boldsymbol{d} \tag{A.10}$$

The matrix product $\boldsymbol{M}^{-1}\boldsymbol{C}^{\varepsilon_{11}}$ is the strain-displacement matrix mapping the global nodal displacements to the global nodal ε_{11} strains.

A.1.1 G Augmentation

Now, consider that nodes of the finite element mesh are selected to be SS, and that the sensors measure ε_{11}. For the G Augmentation method, the rows of $\boldsymbol{M}^{-1}\boldsymbol{C}^{\varepsilon_{11}}$ corresponding

to SS nodes are concatenated to the $\boldsymbol{G}$ matrix. The remaining rows of $\boldsymbol{M}^{-1}\boldsymbol{C}^{\varepsilon_{11}}$ not associated with a node with strain data are ignored. $\delta\boldsymbol{\Psi}^{\varepsilon_{11}}$ is formulated by subtracting the SSIP predicted ε_{11} from the known ε_{11} data and recalculated each SSIP iteration as the SSIP predicted ε_{11} is updated. $\delta\boldsymbol{\Psi}^{\varepsilon_{11}}$ is then concatenated to $\delta\boldsymbol{\rho}$ such that the order of the entries of $\delta\boldsymbol{\Psi}^{\varepsilon_{11}}$ matched the order of the rows of $\boldsymbol{M}^{-1}\boldsymbol{C}^{\varepsilon_{11}}$. The same procedure is performed if a different strain component or multiple strain components are known. In the case of multiple known strain components, the rows concatenated to $\boldsymbol{G}$ are a composite of many different strain-displacement matrices; therefore, equation (A.11), which shows the general form of SSIP with strain SDF via G Augmentation, a superscript ε_{ij} is used for $\boldsymbol{C}$ and $\delta\boldsymbol{\Phi}$ instead of any specific strain component.

$$\boldsymbol{d}^* = \arg\min_{d} \left\| \begin{bmatrix} \delta\boldsymbol{\rho} \\ \delta\boldsymbol{\Psi}^{\varepsilon_{\text{ij}}} \end{bmatrix} - \begin{bmatrix} \boldsymbol{G} \\ \boldsymbol{M}^{-1}\boldsymbol{C}^{\varepsilon_{\text{ij}}} \end{bmatrix} \delta\boldsymbol{d} \right\|^2 \tag{A.11}$$

The iterative process to reconstruct the displacement field proceeds normally, the only difference being that $\delta\boldsymbol{d}$ is now calculated using equation (A.12) below. In the below, recall that $\boldsymbol{L}$ is the discrete Laplacian used for regularization, and α is the scalar regularization parameter.

$$\delta\boldsymbol{d} = \left(\begin{bmatrix} \boldsymbol{G} \\ \boldsymbol{M}^{-1}\boldsymbol{C}^{\varepsilon_{\text{ij}}} \end{bmatrix}^T \begin{bmatrix} \boldsymbol{G} \\ \boldsymbol{M}^{-1}\boldsymbol{C}^{\varepsilon_{\text{ij}}} \end{bmatrix} + \alpha^2 \boldsymbol{L}^T\boldsymbol{L} \right)^{-1} \begin{bmatrix} \boldsymbol{G} \\ \boldsymbol{M}^{-1}\boldsymbol{C}^{\varepsilon_{\text{ij}}} \end{bmatrix}^T \begin{bmatrix} \delta\boldsymbol{\rho} \\ \delta\boldsymbol{\Psi}^{\varepsilon_{\text{ij}}} \end{bmatrix} \tag{A.12}$$

A.1.2 Linear Equality Constraint

The LEC method utilizes the same $\boldsymbol{M}^{-1}\boldsymbol{C}^{\varepsilon_{\text{ij}}}$ and $\delta\boldsymbol{\Phi}^{\varepsilon_{\text{ij}}}$ matrices and vectors formulated earlier in this section. However, instead of concatenating additional rows directly to original SSIP $\boldsymbol{G}$ matrix and $\delta\boldsymbol{\rho}$ vector, the SSIP is recast as a constrained least-squares minimization and the additional rows are expressed as linear equality constraints. The optimization problem statement describing the Linear Constraint Method is given in equation (A.13), where f is the objective function, h are the equality constraints, and k is the number of equality constraints. Each row taken from the strain-displacement matrices becomes a single equality constraint.

$$\begin{aligned} &\text{minimize} \quad f(\boldsymbol{d}) = \left\| \begin{bmatrix} \delta\boldsymbol{\rho} \\ \mathbf{0} \end{bmatrix} - \begin{bmatrix} \boldsymbol{G} \\ \alpha\boldsymbol{L} \end{bmatrix} \delta\boldsymbol{d} \right\|^2 \\ &\text{subject to} \quad h_k(\boldsymbol{d}) = [\boldsymbol{M}^{-1}\boldsymbol{C}^{\varepsilon_{ij}}]_k \delta\boldsymbol{d} - \delta\boldsymbol{\Phi}_k^{\varepsilon_{ij}} = 0, \; k = 1, \ldots, k. \end{aligned} \tag{A.13}$$

To solve for $\delta\boldsymbol{d}$, the MATLAB '*lsqlin*' function is used.

A.2 Displacement Reconstruction Results

Figure A.1 below compares the displacement reconstructions using the SSIP-iFEM, G Augmentation, and Linear Constraint strain SDF methods with 50 SS. Reconstructions are performed on the mounting bracket geometry. For the G Augmentation and LEC methods, α is selected to be 1×10^6, whereas recall that the SSIP-iFEM method does not require regularization. The exact displacement and ε_{22}, ε_{33}, and ε_{23} strain field solutions are given in figure A.4.

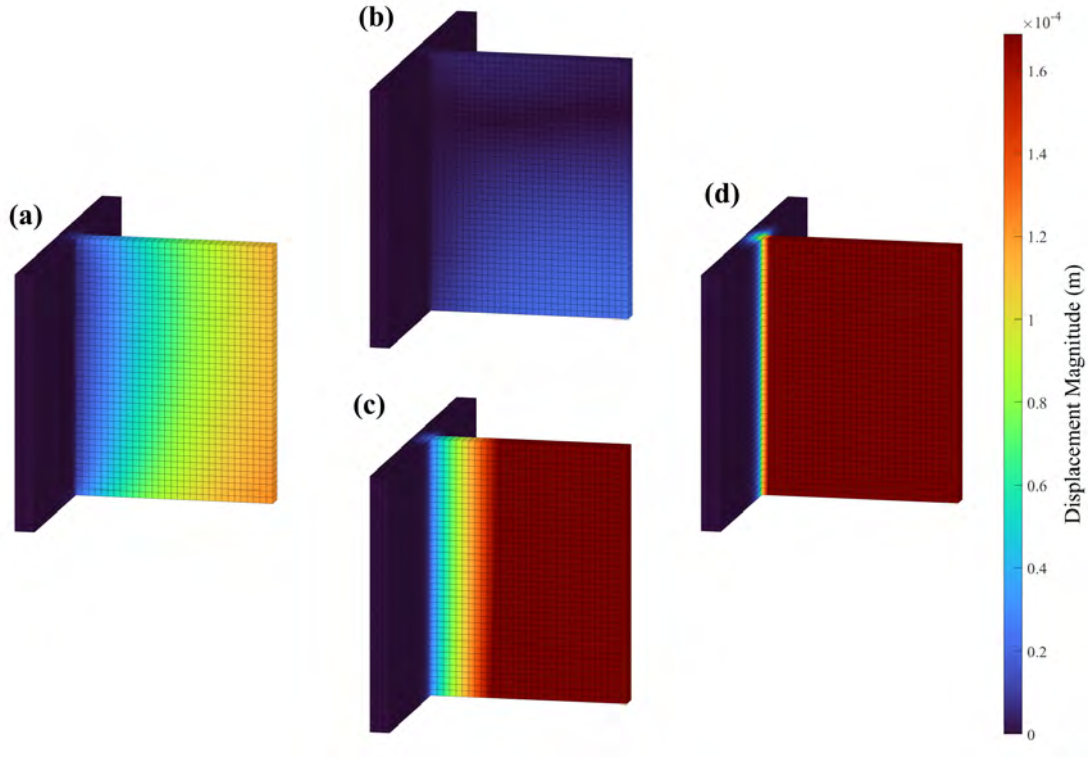

Figure A.1. Displacement reconstruction with 50 SS using the (a) SSIP-iFEM, (b) G Augmentation, (c) weighted G Augmentation, and (d) LEC methods.

It can be seen that the G Augmentation method under-predicts the displacement magnitude. In fact, the reconstruction is very similar to the reconstruction without the use of any sensors. This suggests that this strain SDF method is not having any notable effect on the reconstruction. This may be because the magnitude of the entries of the additional rows concatenated to $\boldsymbol{G}$ are much smaller relative to the entries of $\boldsymbol{G}$. Thus, a reconstruction was also performed with a weight of 1×10^3 multiplied to both $\boldsymbol{M}^{-1}\boldsymbol{C}^{\varepsilon_{ij}}$ and $\delta\boldsymbol{\Psi}^{\varepsilon_{ij}}$, which made the terms of $\boldsymbol{M}^{-1}\boldsymbol{C}^{\varepsilon_{ij}}$ on average the same order of magnitude as the entries of $\boldsymbol{G}$. The result is that the reconstruction is closer to the exact solution, albeit the displacement magnitude is now over-predicted. Nevertheless, the shape of the displacement field is better captured.

On the other hand, the LEC method over-predicts the displacement magnitude to a higher degree than the weighted G Augmentation method. If we break the reconstructions down to displacement components seen in figure A.2, the majority of the over-prediction is in the z displacement component, which is the largest magnitude displacement component in the exact solution. From these displacement reconstructions, it is clear that the SSIP-iFEM method greatly outperforms the other methods.

Seeing that the G Augmentation and LEC displacement reconstructions are not accurate despite the addition of strain data, the reconstructed ε_{22}, ε_{33}, and ε_{23} strain fields are visualized in figure A.3 to determine if the additional strain data improved the strain field recovery. These strain components are visualized because these are the in-plane strain components relative to the mounting bracket web that are measured by the SS. In general, the G Augmentation and LEC strain reconstructions underpredict the strain magnitude. Additionally, the sensor locations are distinctly visible. Although the strains are more accurate near SS, the overall shape of the strain field is not well captured. The LEC method fails to capture the shape of the ε_{33} and ε_{23} fields. While the G Augmentation method reconstructs a similar ε_{23} field, it performs marginally better for the ε_{33} strains. Once again, the iFEM-SSIP method demonstrates much better strain reconstructions with regard to both magnitude and shape.

In addition to the displacement and strain reconstructions not being as accurate, the two unused strain SDF methods are more computationally expensive than the SSIP-iFEM

SDF method. First, a matrix inversion and product is required to formulate the strain-displacement matrix for each strain component, $\boldsymbol{M}^{-1}\boldsymbol{C}^{\varepsilon_{ij}}$, whereas in the SSIP-iFEM method, no matrix inversions or products are required, and a single $\boldsymbol{K}$ matrix contains all the strain-displacement relations for all strain components. Second, as the number of SS was increased, it was observed that longer computational time was required to complete one SSIP iteration. In contrast, the SSIP-iFEM method did not exhibit any notable change in computational time with the increase of the number of SS.

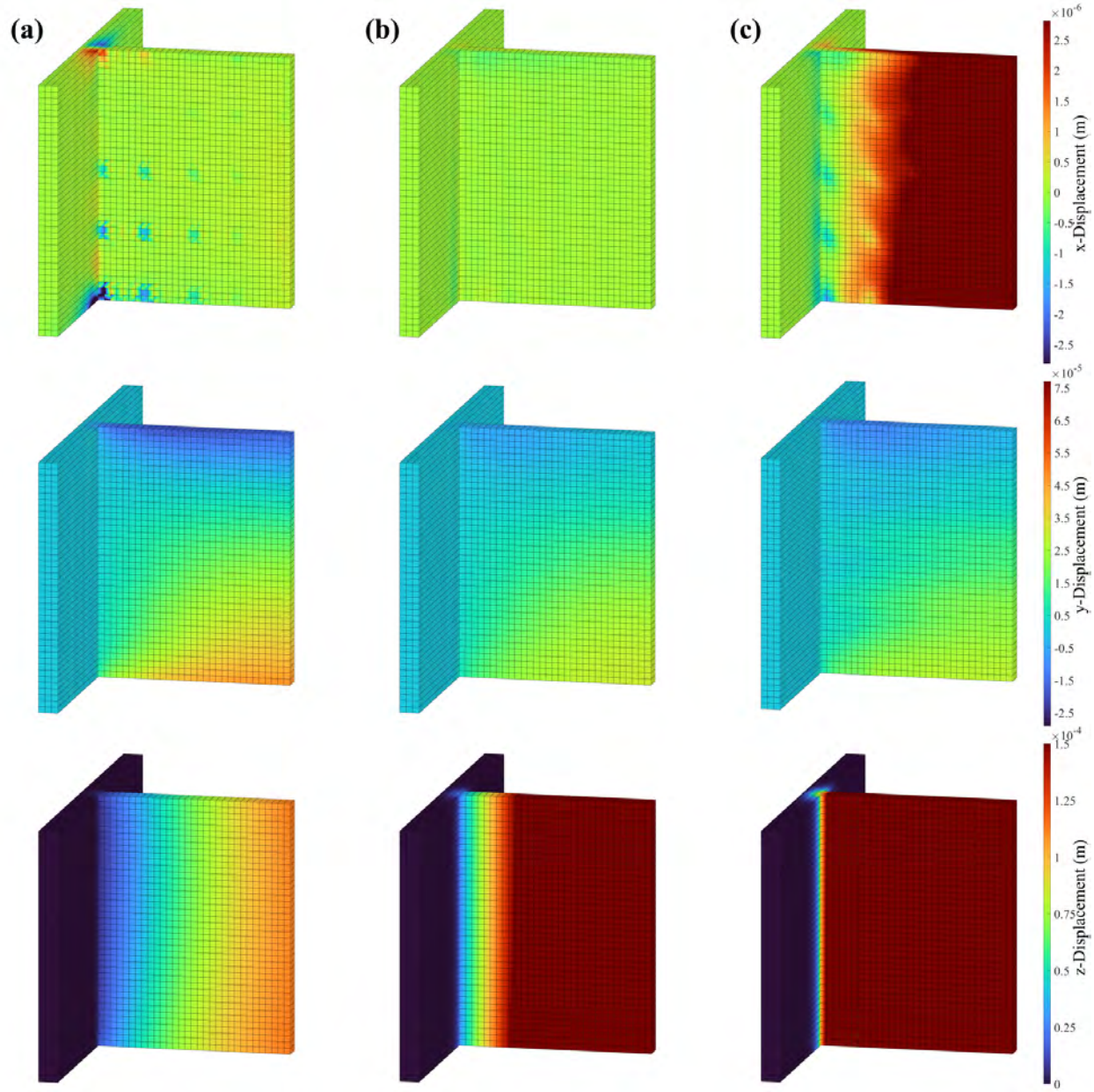

Figure A.2. Displacement reconstructions with 50 SS using the (a) SSIP-iFEM, (b) weighted G Augmentation, and (c) LEC methods split into displacement components.

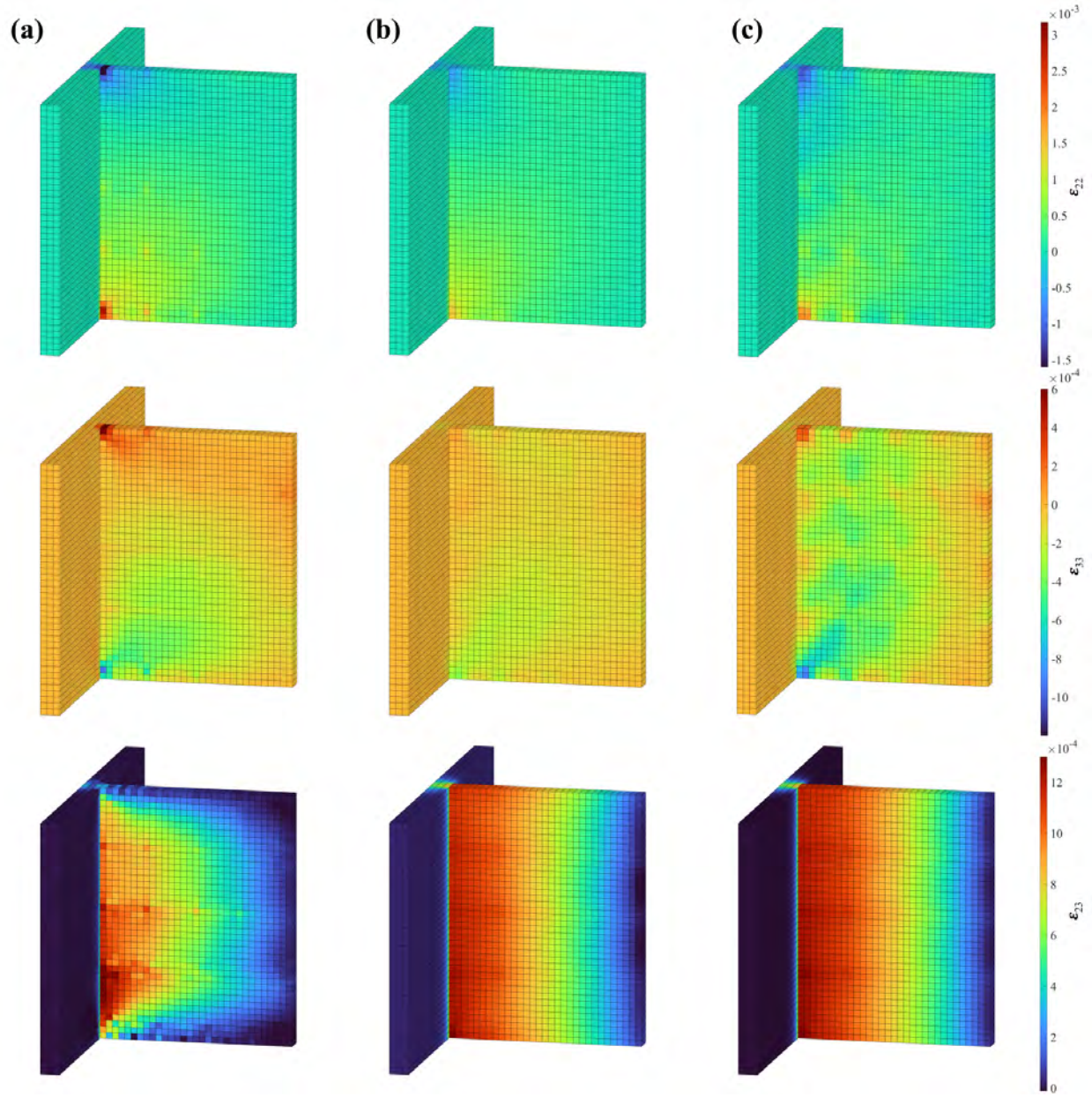

Figure A.3. ε_{22}, ε_{33}, and ε_{23} reconstructions with 50 SS using the (a) SSIP-iFEM, (b) weighted G Augmentation, and (c) LEC methods.

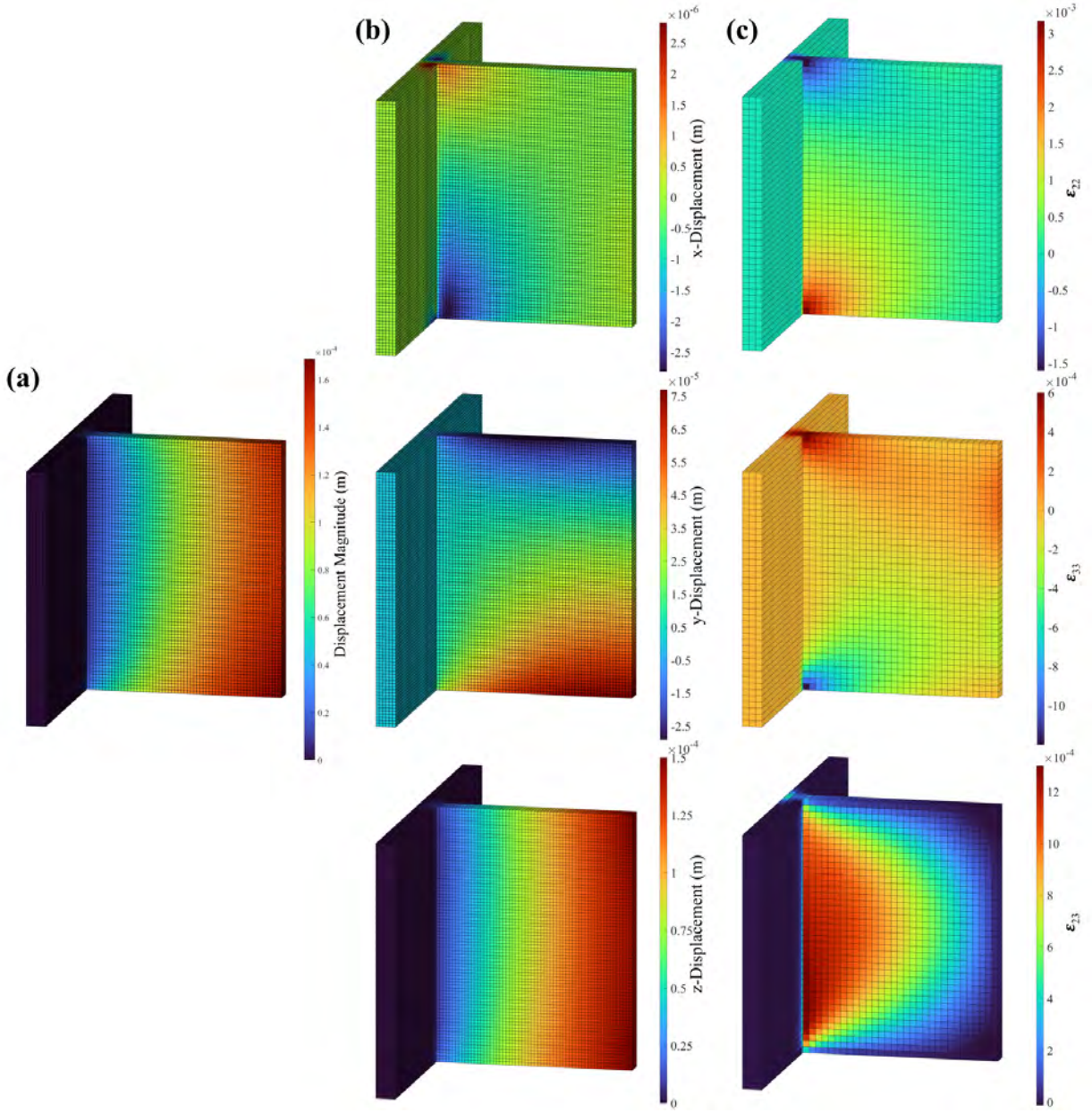

Figure A.4. Exact solution (a) displacement magnitude, (b) displacement components, and (c) ε_{22}, ε_{33}, and ε_{23} strains.